AWARD NUMBER: DE-FG07-05ID14705
AWARDEE NAME AND INSTITUTION: Taro Ueki (PI), University of New Mexico

PROJECT TITLE: A Multivariate Time Series Method for Monte Carlo Reactor Analysis

Report Category: Management
Report Name: Final Technical Report
Period Covered: July 1, 2005 – June 30, 2008

Abstract

A robust multivariate time series method has been established for the Monte Carlo calculation of neutron multiplication problems. The method is termed Coarse Mesh Projection Method (CMPM) and can be implemented using the coarse statistical bins for acquisition of nuclear fission source data. A novel aspect of CMPM is the combination of the general technical principle of projection pursuit in the signal processing discipline and the neutron multiplication eigenvalue problem in the nuclear engineering discipline. CMPM enables reactor physicists to accurately evaluate major eigenvalue separations of nuclear reactors with continuous energy Monte Carlo calculation. CMPM was incorporated in the MCNP Monte Carlo particle transport code of Los Alamos National Laboratory. The great advantage of CMPM over the traditional Fission Matrix method is demonstrated for the three space-dimensional modeling of the initial core of a pressurized water reactor.

Prepared by: Taro Ueki, Assistant professor
University of New Mexico, Chemical and Nuclear Engineering

1. Introduction

The knowledge and availability of non-fundamental mode eigenvalues of neutron multiplication problems are valuable for some type of nuclear reactor analysis. One example is a nodal modal method in which eigenvalues including but not limited to the fundamental-mode eigenvalue are used to analyze the stability of boiling water reactors [1]. Another example is the use of eigenvalue ratios in the confidence interval estimation of nuclear fission source distribution in Monte Carlo (MC) nuclear reactor analysis [2]. In these examples, a robust method of evaluating major eigenvalues using continuous energy nuclear cross section data is desired.

The origin of the project described in this report dates back to the recent development of the calculation of dominant eigenvalue ratio by autoregressive moving average fitting in the standard time series method [3]. The methodology therein enables reactor physicists to compute dominance ratio (DR), i.e., the ratio of the second-largest to largest eigenvalues, by continuous energy Monte Carlo calculation with very simple statistical bins for nuclear fission source data. However, the methodology demands some prior knowledge of eigenfinctions and fine-tuning of convergence control parameters on the user side. Also, it is not capable of computing other major eigenvalue ratios beyond DR; for example, the ratios of the third, fourth and fifth largest eigenvalues to the largest eigenvalue can not be computed.

In this project, PI and his graduate student have established a robust multivariate time series method for computing major eigenvalues with continuous energy Monte Carlo calculation. The guiding principle was “projection pursuit” in the signal processing disciplines [4]. It is the technical philosophy that pursues vectors for feature extraction and takes the projection of multivariate data on these vectors in order to obtain information relevant to problems under analysis. To determine the “projection vector” for neutron multiplication eigenvalue problems, the theory of error propagation was developed for the iterations of Monte Carlo particle transport calculation [5]. This allows the Monte Carlo calculation to automatically determine the projection vectors for the estimation of major eigenvalue ratios. The method was benchmarked against energy-independent deterministic particle transport calculation including discrete ordinates methods and Green’s function method and was applied to the three-dimensional modeling of the initial core of a pressurized water reactor.

2. Projection Pursuit

In nuclear reactor and criticality analysis with Monte Carlo methods, particle transport governed by the physical laws of neutron multiplication is faithfully simulated using a random number generator [6]. This process is iterated with particle population normalization at the beginning of each iteration. The iterations are normally called cycles, generations or batches, and cycles are used in this report. Eventually nuclear fission source distribution reaches stationarity, i.e., equilibrium and fluctuates within a small range. The cycles continue and quantities of interest including the effective neutron multiplication factor, reaction rate distribution, etc., are tallied until these quantities can be presented with sufficiently small statistical uncertainty.

The neutron multiplication eigenvalue problem concerns the nuclear fission source distribution, hereafter abbreviated as "source distribution". Through stationary cycles, source distribution are tallied at statistical bins. The fluctuation of these tallies contain uncompromised information from which major eigenvalue ratios can be extracted via appropriate choices of projection vectors. This was the guiding principle in this project. See Figure 1 and 2. We have developed a theory of how to determine the projection vectors. This is described in the next sections.

3. Error Propagation and Coarse Mesh Projection Method (CMPM)

A form of the neutron multiplication eigenvalue problem convenient for the analysis of Monte Carlo calculation is

$$S_j(\vec{r}) = \frac{1}{k_j}\int_V \mathbf{H}(\vec{r}' \to \vec{r})\, S_j(\vec{r}')\, dV' \tag{1}$$

where $\vec{r}$ is position vector, dV' denotes a differential volume element, the $\mathbf{H}(\vec{r}' \to \vec{r})$ can be understood as the expected number of direct-descendent (first generation) fission neutrons produced per unit volume at $\vec{r}$ due to a fission neutron that was produced at $\vec{r}'$, and the eigenvalues k_j, $j \geq 0$ are assumed to be discrete and ordered $|k_0| > |k_1| > |k_2| > \cdots$ and the corresponding eigenfunctions are denoted $S_j(\vec{r})$, $j = 0,1,\cdots$ (where "0" implies the fundamental mode and "*j*" larger than zero imply *j*-th mode). The fluctuating part of Monte Carlo source distribution at *m*-th stationary cycle, denoted $\vec{e}^{(m)}$, and the random noise at *m*-th stationary cycle, denoted $\vec{\varepsilon}^{(m)}$, satisfy [7]

$$\vec{e}^{(m+1)} = \mathbf{A}_0 \vec{e}^{(m)} + \vec{\varepsilon}^{(m+1)}, \tag{2}$$

where the dimension of Eq (2) is equal to the number of statistical bins and $\mathbf{A}_0$ is error propagation matrix. The important property of Eq (2) is that the eigenvalues of $\mathbf{A}_0$ are k_1/k_0, k_2/k_0, … , i.e., the eigenvalue ratios of the original problem, Eq. (1).

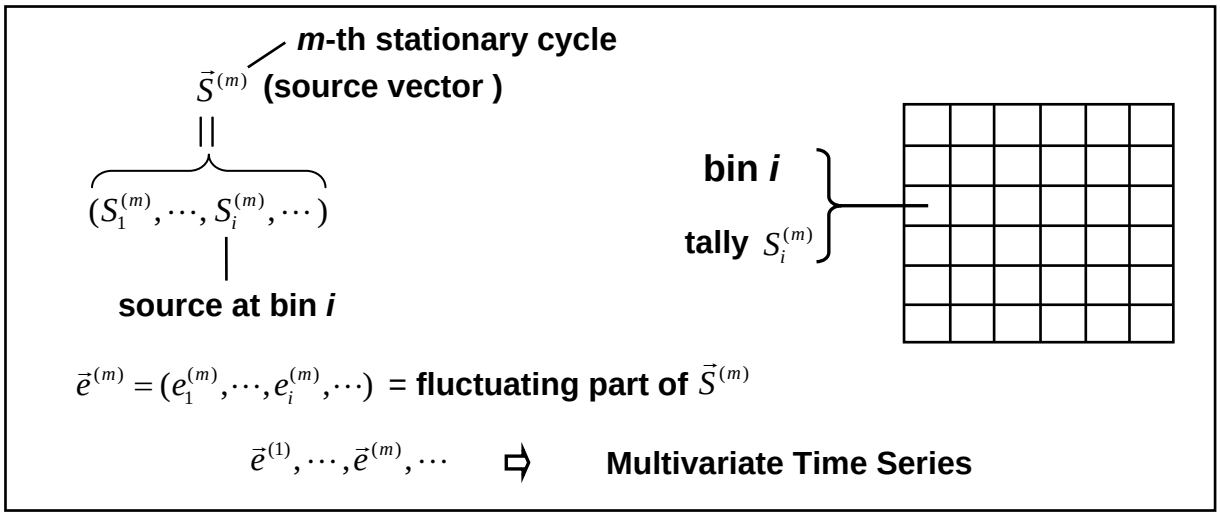

Figure 1: Source Binning

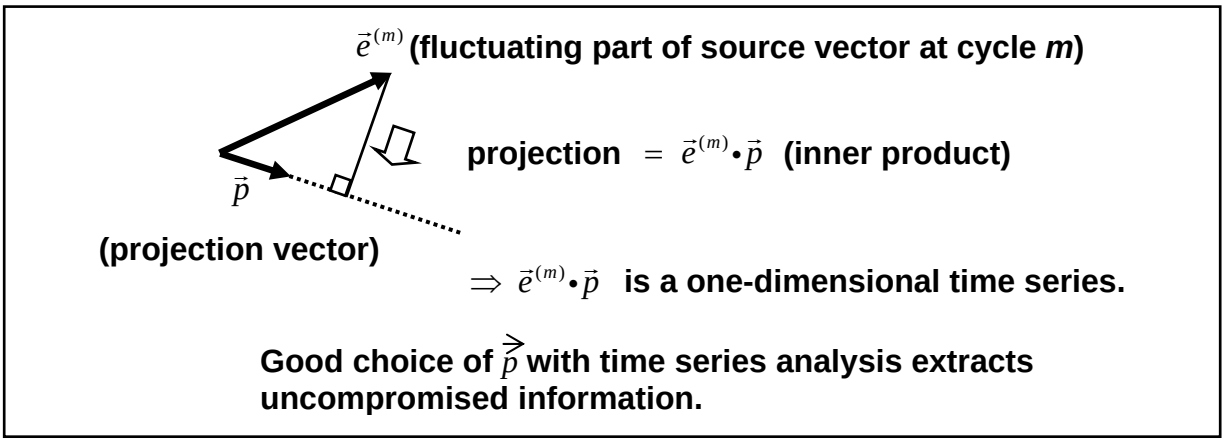

Figure 2: Projection Pursuit

One can certainly compute these eigenvalue ratios by directly solving the eigenvalue problem of $\mathbf{A}_0$ via a matrix solver because $\mathbf{A}_0$ can be estimated by the standard method in multivariate regression analysis [7]. However, this approach suffers from discretization error due to size as in deterministic transport calculation. On the other hand, previous work [3] showed that time series analysis enables one to accurately compute k_1 / k_0 with very large and simple statistical bins. Therefore, the key issue was how to apply the philosophy in Figure 2 to Eq (2) in order to compute these eigenvalue ratios with the automated choice of projection vectors.

PI and his student derived that "if the eigenvectors of the transpose of error propagation matrix are utilized as the projection vectors, the autocorrelation coefficients of the resulting one-dimensional time series are the eigenvalue ratios [7]". This is technically described as follows. Let $\vec{p}_j$ be the eigenvector of the transpose of error propagation matrix $\mathbf{A}_0$ corresponding to k_j / k_0. Here, $\vec{p}_j$ is automatically computed by a standard matrix solver. Then, the projection $\vec{p}_j \bullet \vec{e}^{(m)}$ is an autoregressive process of order one with the coefficient of k_j / k_0:

$$y^{(m+1)} = \lambda_j y^{(m)} + z^{(m+1)} \quad ; \quad y^{(m)} = \vec{p}_j \bullet \vec{e}^{(m)}, \lambda_j = k_j / k_0 \tag{3}$$

where *m* implies *m*-th stationary cycle and $z^{(m)}$ are uncorrelated and identically distributed noises. Therefore, the standard data processing of the linear least square methods is used to compute k_j / k_0. This method of computing eigenvalue ratios, termed the Coarse Mesh Projection Method (CMPM), follows a structure similar to the original time series method [3]. However, instead of relying on a user specified projection vector, a projection vector is automatically calculated and applied by computing the eigenvector of the transpose of error propagation matrix. The use of this projection vector assures several things: 1) only information about the desired eigenmode is extracted; 2) all undesired modes are cancelled out and removed; 3) the time series fitting order is extremely simple; and 4) any desired eigenvalue can be calculated as long as the corresponding eigenmode does not cancel out over the tally bins. The method also retains the strengths of the initial method too, being extremely

fast and efficient. Although a standard matrix solver is used to determine projection vectors, the final answer, k_j / k_0, is extracted statistically, and therefore the method does not suffer discretization error due to size. These aspects are summarized in Figure 3 with the comparison to the traditional fission matrix method (FMM) [8].

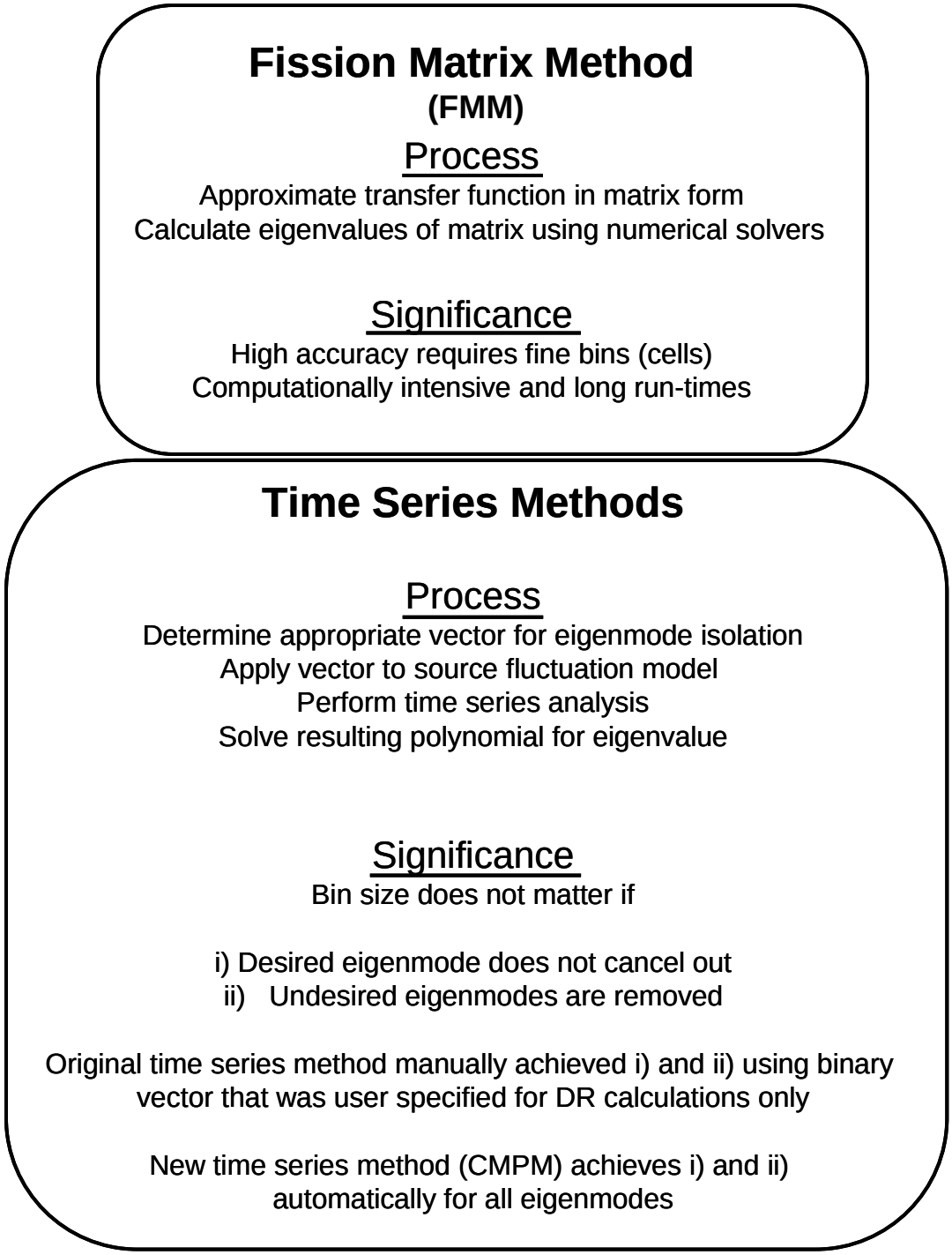

Figure 3: Summary of CMPM Characteristics

The methodology directly based on Eq. (3) still has an unfavorable aspect. Since the fluctuating part $\vec{e}^{(m)}$ involves the subtraction from the mean, the computation can only be made in a posterior manner. In other words, the eigenvalue ratios can be computed only after all stationary cycles are finished. This was pointed out by a technical staff member at MCNP [9] Team in X-3-MCC of Los Alamos National Laboratory. On the Monte Carlo code developer side, there was a practical need for the incremental updating of the eigenvalue ratios without storing source distributions at previous cycles. Therefore, PI and his student sought a new representation starting from Eq. (3) and derived [7]

$$\frac{k_j}{k_0} \text{ at } m\text{-th stationary cycle} = \frac{\left\langle \vec{p}_j \otimes \vec{p}_j, \frac{1}{m-1}\sum_{i=1}^{m-1} \vec{S}^{(i)} \otimes \vec{S}^{(i-1)} \right\rangle}{\left\langle \vec{p}_j \otimes \vec{p}_j, \frac{1}{m}\sum_{i=1}^{m} \vec{S}^{(i)} \otimes \vec{S}^{(i)} \right\rangle}, \qquad (4)$$

where $\otimes$ stands for outer (tensor) product, $\langle\ ,\ \rangle$ the sum of component-wise products and $\vec{S}^{(i)}$ is source vector at *i*-th stationary cycle in Figure 1. The summation in Eq (4) can be updated in an incremental manner without storing source vectors at previous cycles. The projection vector $\vec{p}_j$ can also be updated in the same manner [7]. Therefore, the estimation of eigenvalue ratios can be updated in an incremental manner without storing source vectors at previous cycles. The preliminary results from these activities will be presented in September 2008 at International Meeting for Reactor Physics (Physor 2008) [9]. The technical details are described in the PhD dissertation of PI's student [7].

4. Benchmark Calculation of CMPM

The benchmark calculation of CMPM was extensively conducted in order to establish the methodology. However, only the highlight of these activities is presented in this section. Other benchmark results are found in the PhD dissertation of PI's student [7].

Figure 4 shows a one-dimensional heterogeneous slab problem. For this problem, CMPM results were benchmarked against results from Green's function methods (GFM) [11]. As shown in Table 1, CMPM results from 30 bins agree with GFM results with 1800 spatial cells.

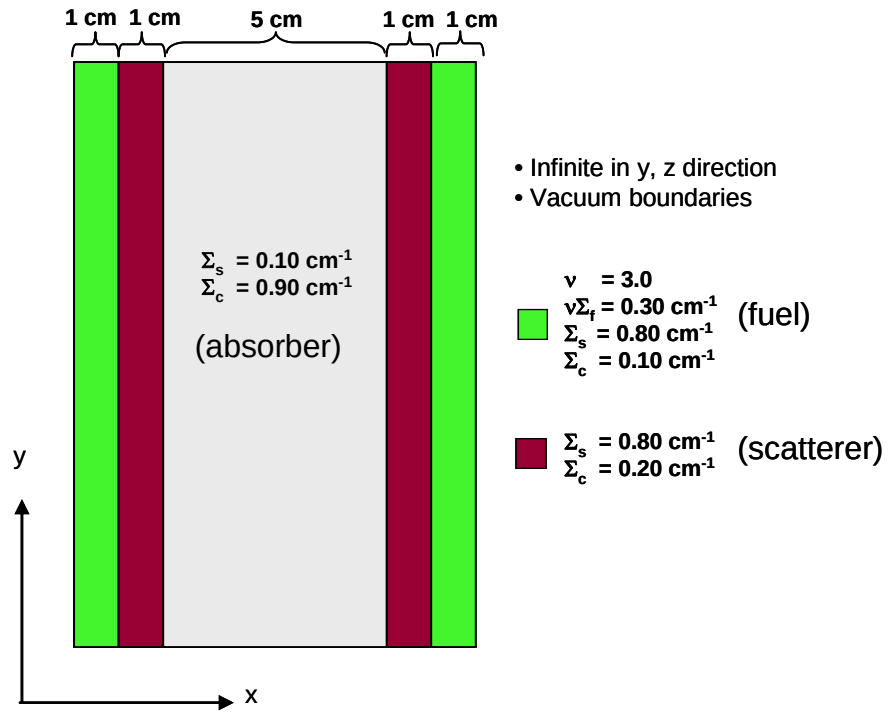

Figure 4: One-Dimensional Heterogeneous Slab Problem

Table 1: First Four Eigenvalue Ratios by GFM and CMPM with 30-bins and 2σ standard deviation

	GFM Using 1,800-cell Mesh	CMPM 2σ Interval Using 30-bins	Benchmark Contained in 2σ?
k_1/k_0	0.999565	(0.999405, 0.999750)	Yes
k_2/k_0	0.304653	(0.292868, 0.311932)	Yes
k_3/k_0	0.304635	(0.285621, 0.304730)	Yes
k_4/k_0	0.167738	(0.161231, 0.180936)	Yes

5. Practical Application

DR, i.e., k_1 / k_0, is especially important among major eigenvalue ratios. One finding in this project is that the number of bins needed for DR estimation is 2, 4 and 8 for one, two and three dimensional problems, respectively, if the method users are not interested in other eigenvalue ratios. To demonstrate this, the whole core of a pressurized water reactor (PWR) at initial cycle in Figure 5 was analyzed. The detailed specifications of this reactor are found elsewhere [12]. CMPM was compared against FMM. The comparison was made for the two and three dimensional modeling of Figure 5. In the former comparison a reflecting boundary condition is imposed on top and bottom and in the latter these top and bottom structures are

taken into account. The results are shown in Figure 6 and 7. It is observed that FMM needs 150 bins in the two dimensional case. By extrapolation, one can see that FMM needs more than 4000 bin in the three dimensional case. In both cases, CMPM needs just four and eight bins, respectively. Also it can be concluded that CMPM is more powerful in three dimensional problems than in two dimensional problems.

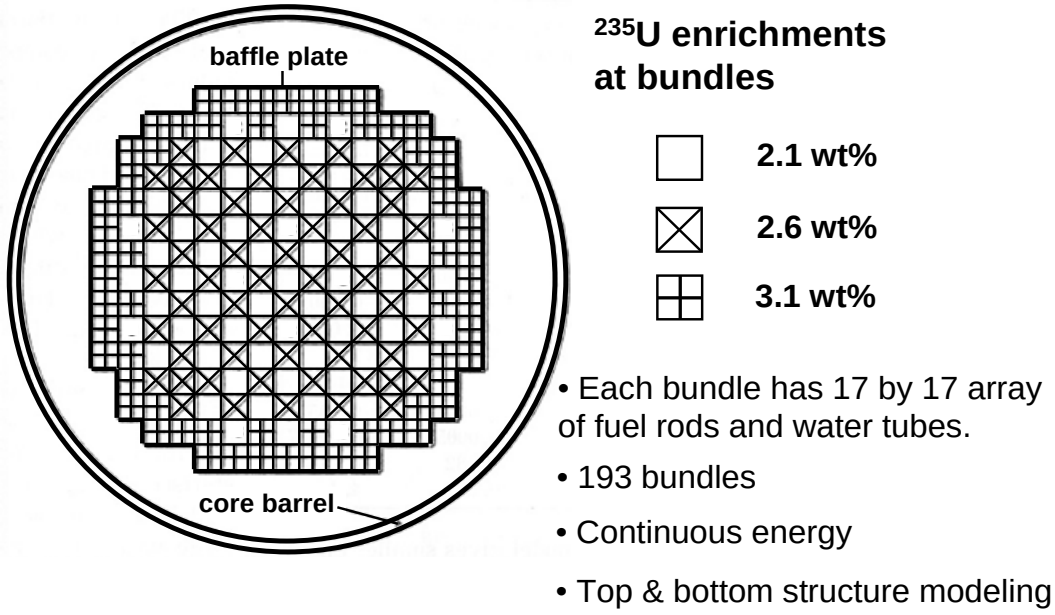

Figure 5: Pressurized Reactor Core at Initial Cycle

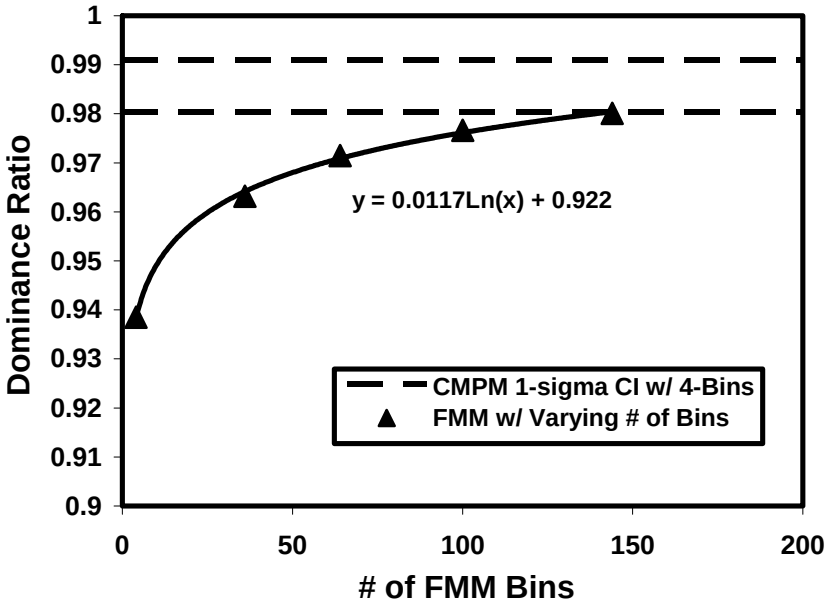

Figure 6: Two Dimensional PWR Comparison FMM vs CMPM

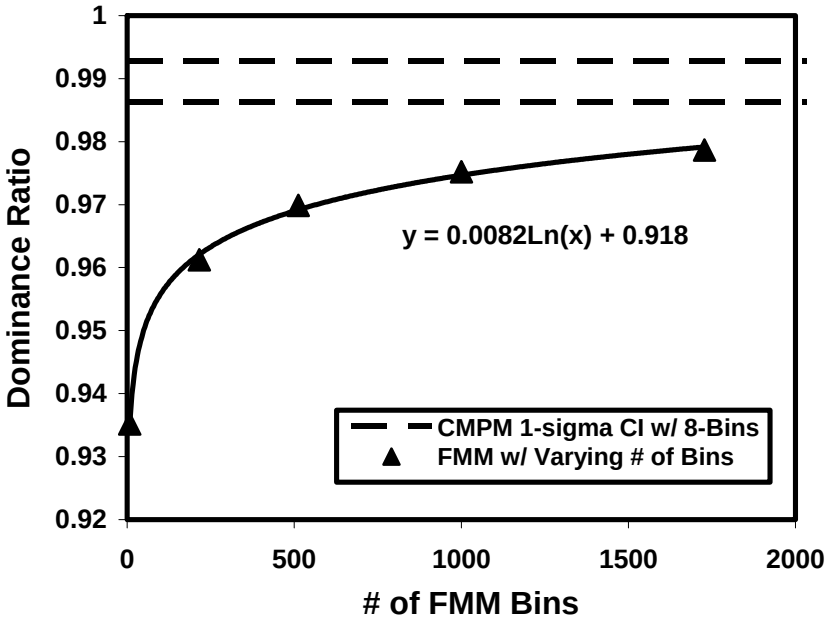

Figure 7: Three dimensional PWR Comparison FMM vs CMPM

6. Change of Plan in Third Year (2007 July – 2008 June)

During the first and second years of this project, PI and his student investigated reliable estimation of DR and its simple applications. These activities were in line with the original proposal of this project and reported in the previous progress reports. In Summer 2007, we found that CMPM can compute major eigenvalue ratios beyond DR. Also in Summer 2007, a collaborator at MCNP Team in X-3 MCC of LANL pointed out that the methodology could not update eigenvalue ratios in an incremental manner as cycles progress. Therefore, in the third year, 1) extensive benchmarking of the calculation of major eigenvalue ratios including but not limited to DR was conducted to establish the methodology and 2) representation alternative to Eq. (3) was sought, which led to Eq. (4) and made the incremental updating possible. These effort led to the inclusion of the methodology in a version of MCNP private to PI's group at UNM and internal to the MCNP Team at LANL.

7. Student Support

Throughout this project, Brian R. Nease, a former PhD student in Chemical and Nuclear Engineering was supported as a full time graduate research assistant in regular semester periods (September-May). Previously, he completed his MS thesis under PI's guidance, which contributed to the original proposal of this award. He successfully defended his dissertation in May 2008.

8. Faculty Support

Part of salary of PI's was supported in summer 2006, 2007, 2008.

9. External Collaboration

PI has a research contract with MCNP Team in X-3 MCC of LANL. Some issues concerning the actual implementation of the developed time series methods with MCNP5 were discussed with a technical staff member at LANL. As reported above, this collaboration led to the inclusion of the developed methodology (CMPM) in private versions of MCNP. Also, the contract is supporting Brian R. Nease through September 2008 to establish resource bases in PI's group and ensure knowledge transfer to a new graduate student.

10. Outcomes

<u>Dissertation</u>

B.R. Nease, Time Series Analysis of Monte Carlo Neutron Transport Calculation, PhD Dissertation, The University of New Mexico (2008). **(See Attachment 1)**

<u>Journal publication</u>

B.R. Nease and T. Ueki, "Time Series Analysis of Monte Carlo Fission Sources: III. Coarse Mesh Projection," *Nuclear Science and Engineering*, **157**, 51-64 (2007). **(See Attachment 2)**

Conference presentations and articles

B.R. Nease and T. Ueki, "Extension of the Autoregressive Method for Autocorrelation Estimation of Monte Carlo Fission Sources," *Transactions of American Nuclear Society* **95**, 741 (2006).
B.R. Nease and T. Ueki, "Coarse Mesh Projection Method for Calculation of Dominance Ratio," *Transactions of American Nuclear Society* **95,** 579 (2006).
B.R. Nease and T. Ueki, "Information Criteria and Higher Eigenmode Estimation in Monte Carlo Calculations," in CD-ROM proceedings of Joint International Topical Meeting on Mathematics & Computation and Supercomputing in Nuclear Applications (M&C + SNA 2007) Monterey, CA, 2007.
B.R. Nease and T. Ueki, "Higher Eigenmode Analysis with Coarse Mesh Projection in Monte Carlo Fission Source Iterations," *Transactions of American Nuclear Society* **98**, 515 (2008). **(See Attachment 3)**
B.R. Nease, F.B. Brown and T. Ueki, "Dominance Ratio Calculations with MCNP," Accepted, PHYSOR 2008, International Conference on the Physics of Reactors "Nuclear Power: A Sustainable Resource," to be held in Septermber 2008.

Article in preparation

Brian R. Nease supported by this project is preparing a review article for the calculation of eigenvalue separation by Monte Carlo methods. We plan on submitting it to Journal of Computational Physics.

11. Deliverable

The methodology in this report was incorporated in a version of MCNP5 [9] private to PI's group and MCNP Team in X-3 MCC of LANL. It will be available in a future version of MCNP.

References

1. R. Miro et al., "A Nodal Modal Method for the Neutron Diffusion Equation. Application to BWR Instabilities Analysis," *Annals of Nuclear Energy*, **29**, 1171-1194, 2002.
2. T. Ueki and B.R. Nease, "Time Series Analysis of Monte Carlo Fission Sources – II: Confidence Interval Estimation," *Nuclear Science and Engineering* **153**, 184 (2006).
3. T. Ueki, F.B. Brown, D.K. Parsons, and J.S. Warsa, "Time Series Analysis of Monte Carlo Fission Sources: I. Dominance Ratio Computation," *Nuclear Sciences and Engineering*, **148**, 374-390 (2004).
4. J.H. Friedman, "Exploratory Projection Pursuit," Journal of the American Statistical Association, Vol. 82, No. 397, 249 (1987).
5. B.R. Nease and T. Ueki, "Time Series Analysis of Monte Carlo Fission Sources: III. Coarse Mesh Projection," *Nuclear Science and Engineering*, **157**, 51-64 (2007).
6. S.A. Dupree and S.K. Fraley, A Monte Carlo Primer, Kluwer Academic/Plenum Publishers, New York (2002).

7. B.R. Nease, Time Series Analysis of Monte Carlo Neutron Transport Calculation, PhD Dissertation, The University of New Mexico (2008).
8. K.W. Morton, "Criticality Calculations by Monte Carlo Methods," AERE-TR-1903, Harwell (1956).
9. B.R. Nease, F.B. Brown and T. Ueki, "Dominance Ratio Calculations with MCNP," Accepted, PHYSOR 2008, International Conference on the Physics of Reactors "Nuclear Power: A Sustainable Resource," to be held in Septermber 2008.
10. X-5 Monte Carlo Team, "MCNP – A General Purpose Monte Carlo N-Particle Transport Code, Version 5," LA-UR-03-1987, Los Alamos National Laboratory, Los Alamos, NM, April, 2003.
11. D.E. Kornreich and B.D. Ganapol, "The Green's Function Method for Nuclear Engineering Applications," *Nuclear Science and Engineering*, **31**, 293 (2003).
12. M. Nakagawa and T. Mori, "Whole Core Calculations of Power Reactors by Use of Monte Carlo Method," Journal of Nuclear Science and Technology, **30** [7], pp 692-701 (1993).

List of Attachments

B.R. Nease, Time Series Analysis of Monte Carlo Neutron Transport Calculation, PhD Dissertation, The University of New Mexico (2008).

B.R. Nease and T. Ueki, "Time Series Analysis of Monte Carlo Fission Sources: III. Coarse Mesh Projection," *Nuclear Science and Engineering*, **157**, 51-64 (2007).

B.R. Nease and T. Ueki, "Higher Eigenmode Analysis with Coarse Mesh Projection in Monte Carlo Fission Source Iterations," *Transactions of American Nuclear Society* **98**, 515 (2008).

Attachment 1

Time Series Analysis of Monte Carlo Neutron Transport Calculations

by

Brian R Nease

B.S. Mechanical Engineering, New Mexico Institute of Mining and Technology, 2003

M.S. Nuclear Engineering, University of New Mexico, 2005

Ph.D. Engineering, University of New Mexico, 2008

Abstract

A time series based approach is applied to the Monte Carlo (MC) fission source distribution to calculate the non-fundamental mode eigenvalues of the system. The approach applies Principal Oscillation Patterns (POPs) to the fission source distribution, transforming the problem into a simple autoregressive order one (AR(1)) process. Proof is provided that the stationary MC process is linear to first order approximation, which is a requirement for the application of POPs. The autocorrelation coefficient of the resulting AR(1) process corresponds to the ratio of the desired mode eigenvalue to the fundamental mode eigenvalue. All modern k-eigenvalue MC codes calculate the fundamental mode eigenvalue, so the desired mode eigenvalue can be easily determined.

The strength of this approach is contrasted against the Fission Matrix method (FMM) in terms of accuracy versus computer memory constraints. Multi-dimensional problems are considered since the approach has strong potential for use in reactor analysis, and the implementation of the method into production codes is discussed. Lastly, the appearance of complex eigenvalues is investigated and solutions are provided.

Table of Contents

List of Figures

List of Tables

Chapter 1: Introduction

In Nuclear Engineering, the neutron transport equation is used to describe the distribution of neutrons in a reactor and how it evolves in time. This equation is frequently made a steady state problem whose eigenvalues are called k-eigenvalues. Knowledge of the fundamental and non-fundamental mode k-eigenvalue solutions is useful in many areas of nuclear reactor analysis. The fundamental mode eigenfunction is everywhere non-negative over the physical space of the problem, and in Monte Carlo calculations it manifests itself as the stationary source distribution. The non-fundamental mode eigenfunctions are those that assume both positive and negative values, and in Monte Carlo calculations they manifest themselves as fluctuating components. While calculation of the fundamental mode eigenvalue is considered routine using power iteration methods (Duderstadt, 1976), it is the non-fundamental mode eigenvalues that often prove difficult to find. Note that throughout this work we refer to the non-fundamental mode k-eigenvalues simply as eigenvalues for the sake of repetition. Since the fundamental mode k-eigenvalue is easily obtained, it is not of primary concern here.

There are two general approaches by which the eigenvalue problem is typically solved. The first approach is deterministic whereby a set of discretized equations that describe the problem are solved exactly. The second approach is stochastic by Monte Carlo (MC) methods, by which a sufficient number of realizations of the problem are made through cycles of particle tracking and neutron population normalization so that the solution is calculated within statistical uncertainty. Historically, the deterministic methods have been the preferred approach to calculating the eigenvalues. MC methods

do exist, but they require estimating the fission kernel (or transfer function) in matrix form and using a linear solver to determine the eigenvalues. This can be computationally expensive, especially for three-dimensional problems. Computer memory limitations, processor speeds, and statistical noise inherent to MC all significantly impact the performance of current methods. The focus of this work is on improving eigenvalue estimation in MC calculations by developing a robust method that can be applied to a wide range of problems.

Despite the difficulty in obtaining eigenvalues in MC, there has been a significant amount of research linking them to important areas in reactor analysis. One such area is evaluating the autocorrelations of the fundamental mode eigenvalue k_0 and the MC fission source distribution in relation to the ratio of eigenvalues k_i/k_0, $i=1,2,\cdots$ (Ueki, 2003). The autocorrelations of the fission source distribution can be particularly large when the first non-fundamental eigenvalue k_1 is very close in magnitude to the fundamental eigenvalue k_0 ($k_1/k_0 \geq 0.99$). The ratio k_1/k_0 is known as the dominance ratio, DR. A high DR indicates that the MC cycles may be strongly correlated, thus biasing the error (or real variance) of the fission source distribution.

An iterative method of calculating the real variance was proposed by Ueki (1997), which works well for ratios of real and apparent variance up to 3.1. Demaret, *et. al*. and Jacquet *et. al.* suggested a fitting method to estimate covariances based on time series methodologies (Demaret, 1999; Jacquet, 2001). Other methods try to eliminate the autocorrelations via the superhistory method, which modifies the source particle normalization procedures (Brissenden, 1986), or by biasing the particle transport through path stretching methods (Ueki, 2002). Combining batches of cycles is yet another way to

eliminate autocorrelations so that the statistical error can be computed by the standard sample variance estimator. All of these methods have mixed results, however, depending on the strength of the autocorrelations, which are themselves strongly dependent on the eigenvalues of the particular problem. Having knowledge of the eigenvalues (specifically the ratio DR) could greatly assist in properly modeling the autocorrelations.

Another application of the eigenvalues is in Boiling Water Reactor (BWR) stability analysis (Hashimoto, 1993; Miro, 2002), where eigenvalues are used to model the out-of-phase oscillations due to excitation of higher-order modes. Eigenvalues can also be used to improve source convergence of MC calculations. Monte Carlo methods rely on the fission source distribution reaching a converged state (fluctuating around the true distribution), before computing tallies of physical properties. Urbatsch (1995) postulated three methods for improving convergence in problems with DR near unity (which are particularly problematic due to large autocorrelations), highlighting the need for an accurate and consistent method of determining eigenvalues.

Much of the foundation for this research can be traced back to Brissenden and Garlick (1986). They sought a method to account for the biases that occurred in traditional MC codes when calculating the fundamental eigenvalue. In their work, they derived an alternate representation of the fission source distribution and showed how error was propagated through the cycles. They linked the magnitude of the error to the eigenvalues and they showed that their formula led to two independently derived results of eigenvalue bias by Gerbard and Prael (1974) and Zolotukhim and Maiorov (1983). It wasn't until much later (Ueki, 2004), however, that time series methods were applied to this alternate representation to specifically extract information about DR. While

powerful, this method required the user to select an observation matrix based on prior knowledge of the eigenmode solution and perform a difficult autoregressive moving average fitting. These characteristics were undesirable for automating the computation of DR.

The limitation of current MC methods in calculating non-fundamental mode eigenvalues highlights the focus of this dissertation. A novel method to estimate eigenvalues in MC calculations is presented. It utilizes time series analysis techniques and is related to recent work on DR calculation (Ueki, 2004). The main objectives when developing this new method were to make it computationally efficient, require little-to-no knowledge of advanced transport equation solutions, and be robust enough to work on a variety of reactor-type problems. These criteria are particularly important if it is to be implemented in production MC radiation transport codes such as MCNP (X-5, 2003).

Before detailing the theory of the different MC methods used to estimate the eigenvalues, we will quickly present an overview of each one. The basic principles of each method are summarized and their differences are discussed and visually illustrated in Figure 1. These summaries are made only to convey a basic understanding of each method. The actual theory behind each method will be discussed in further detail in the coming chapters.

The traditional Fission Matrix Method (FMM) is relatively simple in concept. The spatial domain of the problem is discretized and the fission source kernel (or transfer function) is approximated in matrix form. The eigenvalues of this matrix are then numerically calculated. Unfortunately, the solutions are dependent on the dimensionality of the matrix used to model the kernel. If the matrix is not large enough, then

Fission Matrix Method

Process

Approximate transfer function in matrix form
Calculate eigenvalues of matrix using numerical solvers

Significance

High accuracy requires fine bins (cells)
Computationally intensive and long run-times

Time Series Methods

Process

Determine appropriate vector for eigenmode isolation
Apply vector to source fluctuation model
Perform time series analysis
Solve resulting polynomial for eigenvalue

Significance

Bin size does not matter if

i) Desired eigenmode does not cancel out
ii) Undesired eigenmodes are removed

Original time series method manually achieved i) and ii) using binary vector that was user specified for DR calculations only

New time series method (CMPM) achieves i) and ii) automatically for all eigenmodes

Figure 1: Summary of FMM and CMPM Characteristics

discretization error will strongly bias the results. These calculations are often memory intensive and have extremely long run-times.

The original time series method uses a fundamentally different approach. Instead of directly solving for the eigenvalues of the matrix, a binary projection vector is applied to the source distribution. This vector is chosen in a very specific manner so that a time series fitting can be performed to extract DR. This is a powerful method because it only uses two tally bins, making it extremely fast and efficient. The downsides are that the tally bins are problem dependent and must be specified by the user, and that the time series fitting is extremely complicated.

The new time series method, termed the Coarse Mesh Projection Method (CMPM), follows a similar structure to the original time series method. Instead of relying on a user specified binary projection vector, however, an improved projection vector is automatically calculated and applied. Using this projection vector assures several things: 1) only information about the desired eigenmode is extracted; 2) all undesired modes are cancelled out and removed; 3) the time series fitting order is extremely simple; and 4) any desired eigenvalue can be calculated as long as the corresponding eigenmode does not cancel out over the tally bins. The method also retains the strengths of the initial method too, being extremely fast and efficient. The characteristics of FMM and CMPM are summarized in Figure 1.

In the next chapter, the theory of the neutron transport eigenvalue problem is developed. FMM and initial time series technique to solve for the eigenvalues are discussed. The third chapter introduces the theory of the CMPM. Implementation of the method follows in the fourth chapter, where numerical results are analyzed and discussed.

Chapter 2: Monte Carlo (MC) Transport

In this chapter, the neutron transport equation is presented and manipulated into a form representing the fission source eigenvalue problem. A cycle-wise representation of the fission source distribution specific to MC is derived that proves the asymptotic linearity of the MC process and the bias of its eigenvalue solutions. Lastly, the original efforts to apply time series techniques to solve for the dominance ratio (DR) are presented.

Section 2.1: Fission Source Eigenvalues

The physical significance of the eigenvalues is discussed in this section, as well as the fission source eigenvalue equation. This equation (along with neutron population normalization) represents the stationary MC process by means of a fission kernel. The eigenvalues of the discrete form of this fission kernel correspond to the desired eigenvalues of the transport equation. The process by which this kernel has historically been calculated to estimate the eigenvalues is known as the Fission Matrix Method.

Transport Equation

The transport equation describes the evolution of the neutron distribution in a system over time, given material properties, geometry, and initial and boundary conditions. The equation is comprised of several terms that account for the creation and removal of neutrons in the system. Creation of neutrons is governed solely by fission, which has a

chance to occur when neutrons are absorbed in fissionable materials. Removal of neutrons is governed by absorption in the material and leakage out of the system. Until a neutron is either absorbed or leaked out, it simply scatters around within the system.

The entire transport equation can be expressed mathematically as

$$\frac{1}{\upsilon}\frac{\partial\Psi\left(\vec{r},\vec{\Omega},E,t\right)}{\partial t}+\vec{\Omega}\cdot\vec{\nabla}\Psi\left(\vec{r},\vec{\Omega},E,t\right)+\Sigma_t\left(\vec{r},E\right)\Psi\left(\vec{r},\vec{\Omega},E,t\right)= \int_0^{E_{\max}}\int_{4\pi}\Sigma_s\left(\vec{r},\vec{\Omega}',E'\rightarrow\vec{\Omega},E\right)\Psi\left(\vec{r},\vec{\Omega}',E',t\right)d\vec{\Omega}'dE' + \frac{\chi\left(E\right)}{4\pi}\int_0^{E_{\max}}\int_{4\pi}\nu\Sigma_f\left(\vec{r},E'\right)\Psi\left(\vec{r},\vec{\Omega}',E',t\right)d\vec{\Omega}'dE'+\mathbb{Q}\left(\vec{r}\right) \tag{2.1.1}$$

where Ψ is the angular neutron flux (defined as the product of the neutron speed and the angle-and-energy-dependent number density), υ is the neutron speed, $\vec{r}$ is spatial coordinate vector, $\vec{\Omega}$ is the angular unit vector in the direction of movement, E is energy, Σ_t is the macroscopic total cross section, Σ_s is the macroscopic double-differential scattering cross section, Σ_f is the macroscopic fission cross section, $\chi\left(E\right)$ is the energy spectrum of fission-born neutrons normalized to unity, ν is the average number of neutrons generated per fission event. $\mathbb{Q}\left(\vec{r}\right)$ is an external source term. Note that throughout this work vector quantities are implied by the arrow notation $\vec{r}$ as opposed to r.

The macroscopic cross sections represent the likelihood of a particular event per unit distance traveled. Thus, $\Sigma_t\left(\vec{r},E\right)\Psi\left(\vec{r},\vec{\Omega},E\right)d\vec{\Omega}dE$ is the mean number of collisions per unit volume at $\vec{r}$ for neutrons moving with energy E to dE and in the direction $d\vec{\Omega}$

about $\vec{\Omega}$. The ratio Σ_f/Σ_t can be physically understood as the probability of a fission event given a collision.

For criticality calculations, no external sources are considered (i.e. $\mathbb{Q}(\vec{r})=0$). In addition, Eq. (2.1.1) is time dependent; the first term on the left-hand side (LHS) represents the time rate of change of the neutron distribution. In this work, we are concerned only with steady-state (or time independent) solutions of the transport equation, in which case

$$\frac{\partial\Psi(\vec{r},\vec{\Omega},E,t)}{\partial t}=0. \tag{2.1.2}$$

If this term is removed, it will not have a solution unless there is an exact balance of terms (including geometry, cross-sections, etc.). For this reason, an arbitrary parameter k_{eff} is introduced, changing the equation to

$$\begin{aligned}\vec{\Omega}\cdot\vec{\nabla}\Psi(\vec{r},\vec{\Omega},E)+\Sigma_t(\vec{r},E)\Psi(\vec{r},\vec{\Omega},E)=&\\ \int_0^{E_{\max}}\int_{4\pi}\Sigma_s(\vec{r},\vec{\Omega}',E'\to\vec{\Omega},E)\Psi(\vec{r},\vec{\Omega}',E')d\vec{\Omega}'dE'&\\ +\frac{1}{k_{eff}}\frac{\chi(E)}{4\pi}\int_0^{E_{\max}}\int_{4\pi}\nu\Sigma_f(\vec{r},E')\Psi(\vec{r},\vec{\Omega}',E')d\vec{\Omega}'dE'&\end{aligned} \tag{2.1.3}$$

For some value of k_{eff}, this equation will have a solution. As will be shown, this parameter k_{eff} has important physical meaning. Before explaining this, however, the physical meaning of the terms in Eq. (2.1.3) will be discussed.

Eq. (2.1.3) can be manipulated to physically express the creation and removal terms. The creation term is derived first, solely from the last term on the right-hand side (RHS)

of Eq. (2.1.3), excluding the $1/k_{eff}$ factor for now. A source creation term is introduced as

$$Q(\vec{r}) = \int_0^{E_{\max}} \int_{4\pi} \nu\Sigma_f(\vec{r}, E')\Psi(\vec{r}, \vec{\Omega}', E')\, d\vec{\Omega}' dE' . \tag{2.1.4}$$

Note that this source creation term $Q(\vec{r})$ refers to only fission-born neutrons and is different from the external source term $\mathbb{Q}(\vec{r})$ mentioned previously. The energy spectrum of the fission-born neutrons is described solely by $\chi(E)$ where $\int_0^{E_{\max}} \chi(E)\, dE = 1$. It is assumed that fission-born neutrons appear isotropically in direction such that $\frac{1}{4\pi}\int_{4\pi} Q(\vec{r})\, d\vec{\Omega} = Q(\vec{r})$. Thus, if the last term on the RHS of Eq. (2.1.3) is integrated over the entire problem domain *V*, all angles 4π, and the energy range interval (0, $E_{\max}$), we obtain the total neutron production in the system.

$$\begin{aligned} &\int_V \int_{4\pi} \int_0^{E_{\max}} \frac{\chi(E)}{4\pi} Q(\vec{r})\, dE d\vec{\Omega} dV \\ &\qquad = \int_V Q(\vec{r})\, dV \equiv \text{Total neutron production.} \end{aligned} \tag{2.1.5}$$

The removal terms are derived next from the remaining terms in Eq. (2.1.3), beginning with the leakage term. It proceeds from the first term on the LHS of Eq. (2.1.3). $\vec{\Omega}\cdot\vec{\nabla}\Psi(\vec{r}, \vec{\Omega}, E)$ is the direction derivative of the angular flux in the direction $\vec{\Omega}$. If this term is integrated over all volume, energy and angle, then the result

$$\int_V \int_0^{E_{\max}} \int_{4\pi} \vec{\Omega}\cdot\vec{\nabla}\Psi(\vec{r}, \vec{\Omega}, E)\, d\vec{\Omega} dE dV \tag{2.1.6}$$

represents the summation of the net number of neutrons flowing out of the volume V. According to the divergence theorem (Gauss's theorm), this is also equivalent to the net flow of neutrons across the surface of the volume, *S*. In other words,

$$\begin{aligned}\int_V \vec{\Omega}\cdot\vec{\nabla}\Psi\left(\vec{r},\vec{\Omega},E\right)dV &= \int_V \vec{\nabla}\cdot\vec{\Omega}\Psi\left(\vec{r},\vec{\Omega},E\right)dV \\ &= \int_S \vec{\mathbf{n}}\cdot\vec{\Omega}\Psi\left(\vec{r},\vec{\Omega},E\right)dS\end{aligned} \tag{2.1.7}$$

where $\vec{\mathbf{n}}$ is the outward pointing unit normal vector of dS. Thus,

$$\begin{aligned}&\int_V \int_0^{E_{\max}} \int_{4\pi} \vec{\Omega}\cdot\vec{\nabla}\Psi\left(\vec{r},\vec{\Omega},E\right)d\vec{\Omega}dEdV \\ &\quad = \int_S \int_0^{E_{\max}} \int_{4\pi} \vec{\mathbf{n}}\cdot\vec{\Omega}\Psi\left(\vec{r},\vec{\Omega},E\right)d\vec{\Omega}dEdS \equiv \text{ Total neutron leakage}\end{aligned} \tag{2.1.8}$$

represents the net leakage of neutrons from the surface *S*. This is the first removal term.

Now the absorption will be derived from the remaining two terms in Eq. (2.1.3). The quantity

$$\Sigma_t\left(\vec{r},E\right)\Psi\left(\vec{r},\vec{\Omega},E\right) \tag{2.1.9}$$

represents the total number of collisions from neutrons at point $\vec{r}$ in direction $\vec{\Omega}$ with energy *E*, regardless of whether the collisions result in scatter or absorption. The quantity

$$\int_0^{E_{\max}} \int_{4\pi} \Sigma_s\left(\vec{r},\vec{\Omega}',E'\to\vec{\Omega},E\right)\Psi\left(\vec{r},\vec{\Omega}',E'\right)d\vec{\Omega}'dE' \tag{2.1.10}$$

represents the in-scatter or number of neutrons that scatter from direction $\vec{\Omega}'$ and energy E' into direction $\vec{\Omega}$ and energy E of interest. Since the scattering cross-section only depends on the scattering angle cosine $\mu = \vec{\Omega}'\cdot\vec{\Omega}$, we have that

$$\int_{4\pi} \Sigma_s\left(\vec{r},\vec{\Omega}',E'\to\vec{\Omega},E\right)d\vec{\Omega} = 2\pi\int_{-1}^{1} \Sigma_s\left(\vec{r},\mu,E'\to E\right)d\mu \tag{2.1.11}$$

$$= \Sigma_s\left(\vec{r}, E' \to E\right). \tag{2.1.12}$$

The dependence on $\vec{\Omega}'$ is removed once integrated over $\vec{\Omega}$ because of the relation of the scattering angle cosine. Furthermore, if the differential scattering cross section in Eq. (2.1.12) is integrated over the energy after scattering, the integral becomes the scattering cross section for the energy before scattering

$$\int_0^{E_{\max}} \Sigma_s\left(\vec{r}, E' \to E\right) dE = \Sigma_s\left(\vec{r}, E'\right). \tag{2.1.13}$$

Thus, starting with

$$\int_0^{E_{\max}} \int_{4\pi} \left[\int_0^{E_{\max}} \int_{4\pi} \Sigma_s\left(\vec{r}, \vec{\Omega}', E' \to \vec{\Omega}, E\right) \Psi\left(\vec{r}, \vec{\Omega}', E'\right) d\vec{\Omega}' dE' \right] d\vec{\Omega} dE, \tag{2.1.14}$$

the order of integration can be interchanged

$$= \int_0^{E_{\max}} \int_{4\pi} \left[\int_0^{E_{\max}} \int_{4\pi} \Sigma_s\left(\vec{r}, \vec{\Omega}', E' \to \vec{\Omega}, E\right) d\vec{\Omega} dE \right] \Psi\left(\vec{r}, \vec{\Omega}', E'\right) d\vec{\Omega}' dE'. \tag{2.1.15}$$

Performing the first set of integration according to Eqs. (2.1.11) and (2.1.13) yields

$$= \int_0^{E_{\max}} \int_{4\pi} \Sigma_s\left(\vec{r}, E'\right) \Psi\left(\vec{r}, \vec{\Omega}', E'\right) d\vec{\Omega}' dE'. \tag{2.1.16}$$

Since $\vec{\Omega}'$ and E' are the integration variables, they can be changed to

$$= \int_0^{E_{\max}} \int_{4\pi} \Sigma_s\left(\vec{r}, E\right) \Psi\left(\vec{r}, \vec{\Omega}, E\right) d\vec{\Omega} dE. \tag{2.1.17}$$

Combining the in-scatter and total cross-section terms (Eqs. (2.1.9) and (2.1.10)), integrating over the entire volume *V*, energy *E* and angle $\vec{\Omega}$, and applying Eqs. (2.1.14) – (2.1.17) yields

$$\int_V \int_0^{E_{\max}} \int_{4\pi} \left[\Sigma_t\left(\vec{r}, E\right) \Psi\left(\vec{r}, \vec{\Omega}, E\right) - \Sigma_s\left(\vec{r}, E\right) \Psi\left(\vec{r}, \vec{\Omega}, E\right) \right] d\vec{\Omega} dE dV \tag{2.1.18}$$

which is simply

$$= \int_V \int_0^{E_{\max}} \Sigma_a\left(\vec{r},E\right)\phi\left(\vec{r},E\right)dEdV \equiv \text{ Total neutron absorption .} \qquad (2.1.19)$$

after defining the absorption cross-section as $\Sigma_a\left(\vec{r},E\right)=\Sigma_t\left(\vec{r},E\right)-\Sigma_s\left(\vec{r},E\right)$ and the scalar flux $\int_{4\pi}\Psi\left(\vec{r},\vec{\Omega},E\right)d\vec{\Omega}=\phi\left(\vec{r},E\right)$. Eq. (2.1.19) represents the total number of neutrons absorbed in the system.

Eqs. (2.1.5), (2.1.8), and (2.1.19) describe all of the ways by which neutrons are created or removed in the system. From these quantities, we can determine whether more neutrons are created or removed in the system. The effective multiplication factor k_{eff} is used to measure this. It is obtained by integrating Eq. (2.1.3) over volume, energy and angle and using Eqs. (2.1.5), (2.1.8), and (2.1.14) – (2.1.19) as the ratio

$$k_{eff} = \frac{\int_V Q\left(\vec{r}\right)dV}{\int_S \int_0^{E_{\max}} \int_{4\pi} \vec{\mathbf{n}}\cdot\vec{\Omega}\Psi\left(\vec{r},\vec{\Omega},E\right)d\vec{\Omega}dEdV + \int_V \int_0^{E_{\max}} \Sigma_a\left(\vec{r},E\right)\phi\left(\vec{r},E\right)dEdV}. \qquad (2.1.20)$$

Thus, k_{eff}, called the effective neutron multiplication factor, is a ratio of neutron creation to neutron removal in the system and is used to gauge the criticality of the system. If $k_{eff}>1$ the system is supercritical and generates more neutrons than it removes. If $k_{eff}<1$ the system is sub-critical and removes more neutrons than it produces. If $k_{eff}=1$ the system is in a steady-state balance of neutron production.

Due to the complexity of the transport equation, it is often written compactly in operator notation. Two operators are used based on the physical interpretation of parameters described previously: a fission operator $\mathbf{F}\Psi$ (instead of $Q\left(\vec{r}\right)$) and a

transport operator $\mathbf{T}\Psi$. The fission operator includes the neutron creation terms and the transport operator includes the neutron removal terms. In other words,

$$\mathbf{F}\Psi = \int_0^{E_{\max}} \int_{4\pi} \nu\Sigma_f\left(\vec{r},E'\right)\Psi\left(\vec{r},\vec{\Omega}',E'\right)d\vec{\Omega}'dE' \tag{2.1.21}$$

$$\begin{aligned}\mathbf{T}\Psi = {} & \vec{\Omega}\cdot\vec{\nabla}\Psi\left(\vec{r},\vec{\Omega},E\right)+\Sigma_t\left(\vec{r},E\right)\Psi\left(\vec{r},\vec{\Omega},E\right) \\ & -\int_0^{E_{\max}} \int_{4\pi} \Sigma_s\left(\vec{r},\vec{\Omega}',E'\rightarrow\vec{\Omega},E\right)\Psi\left(\vec{r},\vec{\Omega}',E'\right)d\vec{\Omega}'dE'\end{aligned} \tag{2.1.22}$$

Using these operators and including the effective multiplication factor, the transport equation can be written compactly as

$$\mathbf{T}\Psi = \frac{1}{k_{eff}}\frac{\chi(E)}{4\pi}\mathbf{F}\Psi\,. \tag{2.1.23}$$

Fission Source Eigenvalue Equation

The transport equation will now be manipulated into the fission source eigenvalue equation, since the latter equation is representative of the actual Monte Carlo process. The operator $\mathbf{T}$ in Eq. (2.1.23) is formally inverted and both sides of the equation are operated on by $\mathbf{F}$

$$\mathbf{F}\Psi = \frac{1}{k_{eff}}\left[\mathbf{F}\mathbf{T}^{-1}\frac{\chi(E)}{4\pi}\right]\mathbf{F}\Psi\,. \tag{2.1.24}$$

It is common practice to rewrite the fission operator $\mathbf{F}\Psi$ as $S\left(\vec{r}\right)$ instead of $Q\left(\vec{r}\right)$, often termed the fission source distribution. After defining a new integral kernel $\mathbf{H}\left(\vec{r}'\rightarrow\vec{r}\right)$ as

$$\int_V \mathbf{H}\left(\vec{r}'\rightarrow\vec{r}\right)f\left(\vec{r}'\right)dV' = \left[\mathbf{F}\mathbf{T}^{-1}\frac{\chi(E)}{4\pi}\right](f)\,, \tag{2.1.25}$$

Eq. (2.1.24) can be rewritten as

$$S(\vec{r}) = \frac{1}{k_{eff}} \int_V \mathbf{H}(\vec{r}' \to \vec{r}) S(\vec{r}') dV' . \tag{2.1.26}$$

Physically, this kernel $\mathbf{H}(\vec{r}' \to \vec{r})$ can be understood as the expected number of direct-descendent (first generation) fission neutrons produced per unit volume at $\vec{r}$ due to a fission neutron that was produced at $\vec{r}'$. Eq. (2.1.26) is a special case of the eigenvalue equation shown below in Eq. (2.1.27). In the eigenvalue equation, the eigenvalues k_j, $j \geq 0$ are assumed to be discrete and ordered $|k_0| > |k_1| > |k_2| > \cdots$ and the corresponding eigenfunctions are denoted $S_i(\vec{r})$, $i = 0,1,\cdots$ (where "0" implies the fundamental mode).

$$S_j(\vec{r}) = \frac{1}{k_j} \int_V \mathbf{H}(\vec{r}' \to \vec{r}) S_j(\vec{r}') dV' \tag{2.1.27}$$

This is the fission source eigenvalue equation. The fundamental mode eigenvalue k_0 is k_{eff} and its eigenfunction is normalized as

$$k_{eff} \equiv k_0 = \int_V S_0(\vec{r}) dV . \tag{2.1.28}$$

This normalization cannot be done for all non-fundamental mode eigenfunctions because some modes may integrate to zero over the problem domain. However,

$$k_j = \int_V S_j(\vec{r}) dV \quad \text{when} \int_V S_j(\vec{r}) dV \neq 0 . \tag{2.1.29}$$

It is not known whether all eigenvalues of continuous energy cross-section problems are real and discrete. However, proofs do exist for mono-energetic transport, regardless of whether scattering is isotropic or anisotropic (Sahni, 1996).

Fission Matrix Method

As early as the mid-fifties, Morton (1956) suggested estimating the kernel $\mathbf{H}(\vec{r}' \to \vec{r})$ so that the eigenvalues could be directly calculated from it. In a discrete form, $\mathbf{H}(\vec{r}' \to \vec{r})$ is known as the fission matrix. It can be calculated in a straightforward fashion in MC calculations by dividing up the spatial domain into different regions and tallying how many fission neutrons are created in one particular region due to fission neutrons generated in the other regions. Explicitly, the $(i,j)^{th}$ element of the fission matrix is the likelihood that a fission neutron created in region *j* will cause a fission neutron to be created in region *i*. The fission matrix method was implemented as early as 1966 into the O5R Monte Carlo code at Oak Ridge National Laboratory (Morrison, 1966) for assisting with initial source convergence, but the method has always met with limited success due to statistical noise inherent to MC.

The Fission Matrix method suffers from computational drawbacks, since the accuracy of the non-fundamental eigenvalues is dependent upon the dimensionality of the fission matrix. The larger the dimensionality of the fission matrix, the more discrete eigenvalues there are to approximate the infinite set of the real continuous problem, and the higher the accuracy. However, increasing the dimensionality can quickly make the method computationally prohibitive. If the problem is based on *N* regions, then the fission matrix requires N^2 storage elements. It is easy to see that for three dimensional analyses with bins in each coordinate direction, the number of elements can quickly become unmanageable for modern computers. For this reason, the fission matrix method is generally used to provide rough estimates of eigenvalues.

Section 2.2: Cycle-Wise Representation of MC Fission Source

In this section, the stationary MC process is shown to be asymptotically linear. Proving the asymptotic linearity of the process results in an alternate representation of how the fluctuating part of the fission source distribution evolves from one cycle to the next. The application of the time series methodology, particularly the Coarse Mesh Projection Method developed in Chapter 3, is dependent on this particular representation. The theory presented below has been compiled from several sources (Gelbard, 1974; Brissenden, 1986; Sutton, 1991; Ueki, 2003; Ueki, 2004). After this representation is developed, an analysis is made that relates the magnitude of the k-eigenvalues to the strength of the MC cycle correlations.

Linearity of the Stationary Monte Carlo Process

In modern MC calculations, batches of neutrons are generated in a specified distribution and tracked to accumulate statistics of physical properties. Simulating one batch of neutrons (one realization of the problem) is known as running one cycle. This process is repeated for many cycles, always with the same number of starting neutrons. The starting location for the neutrons in each cycle is dependent on the location of fission events from the previous cycle. These starting locations are updated each cycle so that they eventually match the true source distribution of the problem within statistical fluctuations. When this condition is met, the distribution is said to be stationary.

Assuming that the fission source distribution is stationary, a particular cycle m (or realization) of the fission source distribution can be divided into a deterministic part and a fluctuating part

$$\hat{S}^{(m)}(\vec{r}) = NS(\vec{r}) + \sqrt{N}\hat{e}^{(m)}(\vec{r}). \tag{2.2.1}$$

The hat above $\hat{S}^{(m)}(\vec{r})$ is used to indicate a stochastic realization of the fission source and N represents the number of particles per cycle. The terms N and $\sqrt{N}$ are included as scaling factors, as will be explained next.

The deterministic part $S(\vec{r})$ is the expected normalized value of the fission source distribution defined as

$$S(\vec{r}) \equiv \frac{1}{N} E\left[\hat{S}^{(m)}(\vec{r})\right] \tag{2.2.2}$$

Eqs. (2.2.1) and (2.2.2) imply that

$$E\left[\hat{e}^{(m)}(\vec{r})\right] = 0. \tag{2.2.3}$$

Since $\int_V \hat{S}^{(m)}(\vec{r})\,dV \simeq O(N)$, it is clear that $\int_V S(\vec{r})\,dV \simeq O(1)$. The variance of $\int_V \hat{S}^{(m)}(\vec{r})\,dV$ is also $O(N)$ and is defined as

$$\mathrm{var}\left[\int_V \hat{S}^{(m)}(\vec{r})\,dV\right] \equiv E\left[\left\{\int_V \hat{S}^{(m)}(\vec{r}) - NS(\vec{r})\,dV\right\}^2\right] \tag{2.2.4}$$

Applying Eq. (2.2.1) yields

$$= E\left[\left\{\int_V \sqrt{N}\hat{e}^{(m)}(\vec{r})\,dV\right\}^2\right] \tag{2.2.5}$$

or

$$= NE\left[\left\{\int_V \hat{e}^{(m)}(\vec{r})\,dV\right\}^2\right] \tag{2.2.6}$$

indicating that $\int_V \hat{e}^{(m)}(\vec{r})\,dV \simeq O(1)$ also. No assumptions about the distribution of $\hat{e}^{(m)}(\vec{r})$ are made.

After each cycle *m*, the fundamental mode eigenvalue is estimated as

$$\widehat{k}^{(m)} = \frac{1}{N}\int_V \widehat{S}^{(m)}\left(\vec{r}\right) dV \,. \tag{2.2.7}$$

The expected eigenvalue is

$$k \equiv E\left[\widehat{k}^{(m)}\right] = \int_V S\left(\vec{r}\right) dV \,. \tag{2.2.8}$$

Next, a model is developed that describes how the source distribution evolves from one cycle to the next. The fission source distribution after simulating one batch of particles can be written as

$$\widehat{S}^{(m)}\left(\vec{r}\right) = \mathbf{W}^{(m)}\left(\vec{r}\right) = \sum_{i=1}^{C_m} w_i^{(m)} \delta\left(\vec{r} - \vec{r}_i\right), \tag{2.2.9}$$

where C_m is the number of fission sites during the m^{th} stationary cycle, $w_i^{(m)}$ is the statistical weight assigned to particular fission site, and δ is a Dirac delta function such that $\int \delta\left(\vec{r} - \vec{r}_i\right)\left(f\right) dV = f\left(\vec{r}_i\right)$ and $\delta\left(\vec{r} - \vec{r}_i\right) = 0$ when $\vec{r} \neq \vec{r}_i$. $\mathbf{W}^{(m)}$ is the collection of weights $\left(\text{i.e. } w_j^{(m)} = \left(\mathbf{W}^{(m)}\right)_j = \int_{\Delta V_j} \widehat{S}^{(m)}\left(\vec{r}\right) dV,\ \vec{r}_j \in \Delta V_j,\ \vec{r}_i \notin \Delta V_j,\ i \neq j \right)$ that correspond to the specific fission sites $\vec{r}_1, \vec{r}_2, \cdots, \vec{r}_{C_m}$. The particle weights are normalized such that

$$\sum_{i=1}^{C_m} w_i^{(m)} = \int_V \widehat{S}^{(m)}\left(\vec{r}\right) dV \,. \tag{2.2.10}$$

The probability that a particular fission site $\vec{r}_j$ is chosen as a neutron source location in the cycle $m+1$ is determined from the weight distribution of the previous cycle *m* as

$$p\left(\vec{r}^{(m+1)} = \vec{r}_j\right) = \frac{w_j^{(m)}}{\sum_{i=1}^{C_m} w_i^{(m)}} \,. \tag{2.2.11}$$

If N total starter neutrons are used in cycle $m+1$, then it is expected that $N\ p\left(\vec{r}^{(m+1)}=\vec{r}_j\right)$ will start at that particular fission site $\vec{r}_j$.

Using the kernel $\mathbf{H}\left(\vec{r}_j\rightarrow\vec{r}\right)$, the expected distribution of weights from all neutrons that start at location $\vec{r}$ in cycle $m+1$ given the unit weight at the fission site $\vec{r}_j$ in cycle m is

$$E\left[\mathbf{W}^{(m+1)}\,|\left(\mathbf{W}^{(m)}\right)_j=1\right]=N\ \mathbf{H}\left(\vec{r}_j\rightarrow\vec{r}\right). \tag{2.2.12}$$

Note that $\left(\mathbf{W}^{(m)}\right)_j=1$ above corresponds to $\widehat{S}^{(m)}\left(\vec{r}\right)=\delta\left(\vec{r}-\vec{r}_j\right)$. If Eq. (2.2.12) is multiplied by $p\left(\vec{r}^{(m+1)}=\vec{r}_j\right)$ from Eq. (2.2.11) and is summed over all possible fission sites $\left(\vec{r}_1,\vec{r}_2,\cdots,\vec{r}_{C_m}\right)$, then the expected distribution of weights $\mathbf{W}^{(m+1)}$ at $\vec{r}$ given the distribution of weights $\mathbf{W}^{(m)}$ from all neutrons in the previous cycle (expressed in Eq. (2.2.9)) is

$$E\left[\mathbf{W}^{(m+1)}\,|\,\mathbf{W}^{(m)}\right]=N\frac{\sum_{j=1}^{C_m}w_j^{(m)}\mathbf{H}\left(\vec{r}_j\rightarrow\vec{r}\right)}{\sum_{j=1}^{C_m}w_j^{(m)}}. \tag{2.2.13}$$

Instead of expressing this in terms of a collection of statistical weights, however, it will be expressed in terms of the fission source distribution $\widehat{S}^{(m)}\left(\vec{r}\right)$. The numerator of Eq. (2.2.13) can be manipulated as

$$\sum_{j=1}^{C_m}w_j^{(m)}\mathbf{H}\left(\vec{r}_j-\vec{r}\right)=\sum_{j=1}^{C_m}w_j^{(m)}\mathbf{H}\left(\vec{r}_j\rightarrow\vec{r}\right)\int_V\delta\left(\vec{r}'-\vec{r}_j\right)dV' \tag{2.2.14}$$

$$=\int_V\sum_{j=1}^{C_m}w_j^{(m)}\delta\left(\vec{r}'-\vec{r}_j\right)\mathbf{H}\left(\vec{r}_j\rightarrow\vec{r}\right)dV' \tag{2.2.15}$$

$$= \int_V \sum_{j=1}^{C_m} w_j^{(m)} \delta\left(\vec{r}' - \vec{r}_j\right) \mathbf{H}\left(\vec{r}' \to \vec{r}\right) dV' . \qquad (2.2.16)$$

Eq. (2.2.16) is obtained from the relation $\delta(x-y) f(x) = \delta(x-y) f(y)$. Applying Eq. (2.2.9) at this point yields

$$\sum_{j=1}^{C_m} w_j^{(m)} \mathbf{H}\left(\vec{r}_j - \vec{r}\right) = \int_V \sum_{j=1}^{C_m} w_j^{(m)} \delta\left(\vec{r}' - \vec{r}_j\right) \mathbf{H}\left(\vec{r}' \to \vec{r}\right) dV'$$

$$= \int_V \hat{S}^{(m)}\left(\vec{r}'\right) \mathbf{H}\left(\vec{r}' \to \vec{r}\right) dV' . \qquad (2.2.17)$$

Using Eq. (2.2.10) and Eq. (2.2.17) and the correspondence of $\hat{S}^{(m)}(\vec{r})$ and $\mathbf{W}^{(m)}(\vec{r})$, the normalized source distribution described by Eq. (2.2.13) is rewritten as

$$E\left[\hat{S}^{(m+1)}(\vec{r}) \,|\, \hat{S}^{(m)}(\vec{r})\right] = N \frac{\int \hat{S}^{(m)}\left(\vec{r}'\right) \mathbf{H}\left(\vec{r}' \to \vec{r}\right) dV'}{\int \hat{S}^{(m)}\left(\vec{r}'\right) dV'} . \qquad (2.2.18)$$

This is a conditional distribution that represents the expected source distribution in cycle $m+1$ given the source distribution from the previous cycle $\hat{S}^{(m)}(\vec{r})$. It was only assumed in previous work (Sutton, 1991), but has been formally derived here.

The stochastic equation describing $\hat{S}^{(m+1)}$ can then be written as

$$\hat{S}^{(m+1)}(\vec{r}) = N \frac{\int \hat{S}^{(m)}\left(\vec{r}'\right) \mathbf{H}\left(\vec{r}' \to \vec{r}\right) dV'}{\int \hat{S}^{(m)}\left(\vec{r}'\right) dV'} + \sqrt{N} \hat{\varepsilon}^{(m+1)}(\vec{r}) . \qquad (2.2.19)$$

The fluctuating term $\hat{\varepsilon}^{(m+1)}(\vec{r})$ is a random noise component resulting from population normalization of starting neutrons and subsequent tracking. As before, the N and $\sqrt{N}$ are scaling terms. Eqs. (2.2.18) and (2.2.19) imply that $\hat{\varepsilon}^{(m)}(\vec{r})$ satisfies

$$E\left[\hat{\varepsilon}^{(m+1)}(\vec{r}) \,|\, \hat{S}^{(m)}(\vec{r})\right] = 0 . \qquad (2.2.20)$$

This result further implies that

$$E\left[\hat{\varepsilon}^{(m+1)}\left(\vec{r}\right)\right]=E\left[E\left[\hat{\varepsilon}^{(m+1)}\left(\vec{r}\right)|\hat{S}^{(m)}\left(\vec{r}\right)\right]\right]=0. \tag{2.2.21}$$

No assumptions about the distribution of $\hat{\varepsilon}^{(m)}\left(\vec{r}\right)$ are made. It is important to note that following directly from Eqs. (2.2.1) and (2.2.20),

$$E\left[\hat{\varepsilon}^{(m+1)}\left(\vec{r}\right)|\hat{e}^{(m)}\left(\vec{r}\right)\right]=0. \tag{2.2.22}$$

Similarly,

$$E\left[\hat{\varepsilon}^{(m+1)}\left(\vec{r}\right)\right]=E\left[E\left[\hat{\varepsilon}^{(m+1)}\left(\vec{r}\right)|\hat{e}^{(m)}\left(\vec{r}\right)\right]\right]=0. \tag{2.2.23}$$

Now there are two expressions describing the fission source in cycle m and $m+1$. Substituting Eq. (2.2.1) into Eq. (2.2.19) and dividing through by N results in

$$S\left(\vec{r}\right)+\frac{1}{\sqrt{N}}\hat{e}^{(m+1)}\left(\vec{r}\right)=\frac{\int_V\left[NS\left(\vec{r}'\right)+\sqrt{N}\hat{e}^{(m)}\left(\vec{r}'\right)\right]H\left(\vec{r}'\to\vec{r}\right)dV'}{\int_V\left[NS\left(\vec{r}'\right)+\sqrt{N}\hat{e}^{(m)}\left(\vec{r}'\right)\right]dV'}+\frac{1}{\sqrt{N}}\hat{\varepsilon}^{(m+1)}\left(\vec{r}\right) \tag{2.2.24}$$

To reduce Eq. (2.2.24) further, the first term on the right hand side (RHS) of the equation must be manipulated. First, N^{-1} is applied throughout. Next, the numerator is expanded and Eq. (2.2.8) is applied to the denominator resulting in

$$\frac{\int_V H\left(\vec{r}'\to\vec{r}\right)S\left(\vec{r}'\right)dV'+\frac{1}{\sqrt{N}}\int_V H\left(\vec{r}'\to\vec{r}\right)\hat{e}^{(m)}\left(\vec{r}'\right)dV'}{k\left(1+\frac{1}{k\sqrt{N}}\int_V\hat{e}^{(m)}\left(\vec{r}'\right)dV'\right)} \tag{2.2.25}$$

At this point, the denominator is in the form $\left(1+x\right)^{-1}$ with $x<1$, which can also be written in series form as $1-x+x^2-x^3+\cdots$. Rewriting the denominator this way yields

$$\left[\frac{1}{k}\int_V H\left(\vec{r}'\to\vec{r}\right)S\left(\vec{r}'\right)dV'+\frac{1}{k\sqrt{N}}\int_V H\left(\vec{r}'\to\vec{r}\right)\hat{e}^{(m)}\left(\vec{r}'\right)dV'\right]$$
$$\times\left(1-\frac{1}{k\sqrt{N}}\int_V \hat{e}^{(m)}\left(\vec{r}'\right)dV'+\frac{1}{k^2N}\left(\int_V \hat{e}^{(m)}\left(\vec{r}'\right)dV'\right)\left(\int_V \hat{e}^{(m)}\left(\vec{r}''\right)dV''\right)-\cdots\right) \tag{2.2.26}$$

All terms are multiplied out and the terms of order N^{-1} or greater are combined into a leading order term $O\left(N^{-1}\right)$, yielding

$$\frac{1}{k}\int_V H\left(\vec{r}'\to\vec{r}\right)S\left(\vec{r}'\right)dV'+\frac{1}{k\sqrt{N}}\int_V H\left(\vec{r}'\to\vec{r}\right)\hat{e}^{(m)}\left(\vec{r}'\right)dV'$$
$$-\frac{1}{k^2\sqrt{N}}\int_V H\left(\vec{r}''\to\vec{r}\right)S\left(\vec{r}''\right)dV''\int_V \hat{e}^{(m)}\left(\vec{r}'\right)dV'+O\left(N^{-1}\right) \tag{2.2.27}$$

A kernel term is defined

$$\mathbf{A}\left(\vec{r}'\to\vec{r}\right)=\frac{1}{k}\left[H\left(\vec{r}'\to\vec{r}\right)-\frac{1}{k}\int_V H\left(\vec{r}''\to\vec{r}\right)S\left(\vec{r}''\right)dV''\right] \tag{2.2.28}$$

allowing Eq. (2.2.27) to be simplified to

$$\frac{1}{k}\int_V H\left(\vec{r}'\to\vec{r}\right)S\left(\vec{r}'\right)dV'+\frac{1}{\sqrt{N}}\int_V \mathbf{A}\left(\vec{r}'\to\vec{r}\right)\hat{e}^{(m)}\left(\vec{r}'\right)dV'+O\left(N^{-1}\right) \tag{2.2.29}$$

Now that the first term on the RHS of Eq. (2.2.24) has been manipulated into this form, it can be substituted back into Eq. (2.2.24) to obtain

$$S\left(\vec{r}\right)+\frac{1}{\sqrt{N}}\hat{e}^{(m+1)}\left(\vec{r}\right)=\frac{1}{k}\int_V H\left(\vec{r}'\to\vec{r}\right)S\left(\vec{r}'\right)dV'$$
$$+\frac{1}{\sqrt{N}}\int_V \mathbf{A}\left(\vec{r}'\to\vec{r}\right)\hat{e}^{(m)}\left(\vec{r}'\right)dV'+\frac{1}{\sqrt{N}}\hat{\varepsilon}^{(m+1)}\left(\vec{r}\right)+O\left(N^{-1}\right) \tag{2.2.30}$$

Before continuing with the cycle-wise representation of the MC fission source, we must mention an important detail: a bias exists in the fission source distribution and its associated eigenvalue when using MC iterative source methods. These biases will be quickly derived before proceeding further.

Taking the expectation of Eq. (2.2.30) yields

$$S(\vec{r}) = \frac{1}{k}\int_V H(\vec{r}' \to \vec{r}) S(\vec{r}')\, dV' + O\left(N^{-1}\right). \tag{2.2.31}$$

Recall that the exact fundamental mode solution is

$$S_0(\vec{r}) = \frac{1}{k_0}\int_V H(\vec{r}' \to \vec{r}) S_0(\vec{r}')\, dV'. \tag{2.2.32}$$

Subtracting Eq. (2.2.32) from Eq. (2.2.31) yields

$$S(\vec{r}) - S_0(\vec{r}) - \int_V H(\vec{r}' \to \vec{r}) \left[\frac{S(\vec{r}')}{k} - \frac{S_0(\vec{r}')}{k_0}\right] dV' = O\left(N^{-1}\right). \tag{2.2.33}$$

A bias of order $O\left(N^{-a}\right)$ is allowed to exist between the exact solution and the MC solution such that

$$S(\vec{r}) - S_0(\vec{r}) = O\left(N^{-a}\right), \tag{2.2.34}$$

which implies that

$$k - k_0 = O\left(N^{-a}\right), \tag{2.2.35}$$

by Eqs. (2.2.28) and (2.2.8). Using Eqs. (2.2.34) and (2.2.35), Eq. (2.2.33) can be rewritten

$$O\left(N^{-a}\right) = O\left(N^{-1}\right). \tag{2.2.36}$$

It is clear that the order of bias must be equivalent, i.e. $a = 1$, otherwise the RHS and LHS of Eq. (2.2.36) will differ by orders of magnitude as $N \to \infty$. Thus, a bias exists when evaluating the fission source distribution and its associated eigenvalue by MC iterative source methods

$$S(\vec{r}) - S_0(\vec{r}) = O\left(N^{-1}\right) \tag{2.2.37}$$

$$k - k_0 = O\left(N^{-1}\right). \tag{2.2.38}$$

Though the MC evaluation of these quantities is biased, in the limit of large N (particles per cycle) MC yields the correct unbiased solution of the fission source distribution and the fundamental k-eigenvalue.

Having pointed out the biases inherent to MC iterative source methods, we can return to the derivation of the cycle-wise representation of the fission source. Subtracting Eq. (2.2.31) from Eq. (2.2.30) and multiplying through by $\sqrt{N}$ yields

$$\hat{e}^{(m+1)}\left(\vec{r}\right) = \int_V \mathbf{A}\left(\vec{r}' \to \vec{r}\right)\hat{e}^{(m)}\left(\vec{r}'\right)dV' + \hat{\varepsilon}^{(m+1)}\left(\vec{r}\right) + O\left(N^{-1/2}\right) \tag{2.2.39}$$

A new operator $\mathbf{A}_0\left(\vec{r}' \to \vec{r}\right)$ is introduced corresponding to the fundamental-mode solution of the transport equation:

$$\mathbf{A}_0\left(\vec{r}' \to \vec{r}\right) = \frac{1}{k_0}\left[H\left(\vec{r}' \to \vec{r}\right) - S_0\left(\vec{r}\right)\right]. \tag{2.2.40}$$

From Eqs. (2.2.32), (2.2.37) and (2.2.38), it is clear that

$$\mathbf{A}\left(\vec{r}' \to \vec{r}\right) = \mathbf{A}_0\left(\vec{r}' \to \vec{r}\right) + O\left(N^{-1}\right). \tag{2.2.41}$$

Applying $\mathbf{A}_0\left(\vec{r}' \to \vec{r}\right)$ to Eq. (2.2.39) and using operator notation such that

$$\mathbf{A}_0\hat{e}^{(m)} = \int \mathbf{A}_0\left(\vec{r}' \to \vec{r}\right)\hat{e}^{(m)}\left(\vec{r}'\right)dV', \tag{2.2.42}$$

we obtain the working form

$$\hat{e}^{(m+1)} = \mathbf{A}_0\hat{e}^{(m)} + \hat{\varepsilon}^{(m+1)} + O\left(N^{-1/2}\right). \tag{2.2.43}$$

Eq. (2.2.43) is the key equation in describing how error is propagated throughout the cycles. The operator $\mathbf{A}_0$ is termed the Noise Propagation (NP) operator. As will be

shown, its eigenvalues correspond to the eigenvalue ratios of the fission source distribution and the larger the eigenvalues of $\mathbf{A}_0$, the stronger the cycle correlations.

Eq. (2.2.43) also illustrates the asymptotic linearity of the process (or Markov nature). The process can be represented in terms of discrete time events as

$$\cdots \rightarrow \hat{e}^{(i)} \xrightarrow[\downarrow]{\hat{\varepsilon}^{(i+1)}} \hat{e}^{(i+1)} \xrightarrow[\downarrow]{\hat{\varepsilon}^{(i+2)}} \hat{e}^{(i+2)} \xrightarrow[\downarrow]{\hat{\varepsilon}^{(i+3)}} \hat{e}^{(i+3)} \rightarrow \cdots$$

Each particular state of the source fluctuation $\hat{e}^{(i+1)}$ is completely determined by the previous state $\hat{e}^{(i)}$ and the generated noise $\hat{\varepsilon}^{(i+1)}$. This asymptotic linearity leads to two important lemmas about the noise terms $\hat{\varepsilon}^{(p)}$:

$$E\left[\hat{\varepsilon}^{(p)}\hat{e}^{(q)}\right] = 0, \quad p > q \tag{2.2.44}$$

$$E\left[\hat{\varepsilon}^{(p)}\hat{\varepsilon}^{(q)}\right] = 0, \quad p > q\,. \tag{2.2.45}$$

Eq. (2.2.44) can be proven by considering for cycles $p > q$

$$E\left[\hat{\varepsilon}^{(p)}\hat{e}^{(q)}\right] = E\left[E\left[\hat{\varepsilon}^{(p)}\hat{e}^{(q)} \mid \hat{e}^{(p-1)}, \hat{e}^{(q)}\right]\right] \tag{2.2.46}$$

by the theorem of iterated expression in standard probability theory. This means that the quantities $\hat{e}^{(p-1)}$ and $\hat{e}^{(q)}$ are fixed. Since $\hat{e}^{(q)}$ is fixed, it follows that it can be pulled out of the expectation becoming

$$= E\left[\hat{e}^{(q)}E\left[\hat{\varepsilon}^{(p)} \mid \hat{e}^{(p-1)}, \hat{e}^{(q)}\right]\right]. \tag{2.2.47}$$

The effect of $\hat{e}^{(q)}$ is incorporated in $\hat{e}^{(p-1)}$ due to the linearity of the process, so this can be further reduced to

$$= E\left[\hat{e}^{(q)}E\left[\hat{\varepsilon}^{(p)} \mid \hat{e}^{(p-1)}\right]\right]. \tag{2.2.48}$$

Note that once $\hat{e}^{(p-1)}$ is fixed, $\hat{\varepsilon}^{(p)}$ is solely governed by particle population normalization and tracking. The inner expectation is zero by Eq. (2.2.22), implying that

$$E\left[\hat{\varepsilon}^{(p)}\hat{e}^{(q)}\right]=0,\quad p>q. \tag{2.2.49}$$

Eq. (2.2.45) can be proven similarly by considering

$$\begin{aligned}E\left[\hat{\varepsilon}^{(p)}\hat{\varepsilon}^{(q)}\right]&=E\left[E\left[\hat{\varepsilon}^{(p)}\hat{\varepsilon}^{(q)}\mid\hat{e}^{(p-1)},\hat{\varepsilon}^{(q)}\right]\right]\\&=E\left[\hat{\varepsilon}^{(q)}E\left[\hat{\varepsilon}^{(p)}\mid\hat{e}^{(p-1)},\hat{\varepsilon}^{(q)}\right]\right]\\&=E\left[\hat{\varepsilon}^{(q)}E\left[\hat{\varepsilon}^{(p)}\mid\hat{e}^{(p-1)}\right]\right]\\&=0.\end{aligned} \tag{2.2.50}$$

This can also be proven alternatively as follows. By Eq. (2.2.19), $\hat{\varepsilon}^{(p)}$ is completely governed by population normalization and particle tracking once $\hat{e}^{(p-1)}$ is fixed. Therefore, $\hat{\varepsilon}^{(p)}$ and $\hat{\varepsilon}^{(q)}$ are conditionally independent upon a realization of $\hat{e}^{(p-1)}$. This implies that

$$E\left[\hat{\varepsilon}^{(p)}\hat{\varepsilon}^{(q)}\mid\hat{e}^{(p-1)}\right]=E\left[\hat{\varepsilon}^{(p)}\mid\hat{e}^{(p-1)}\right]E\left[\hat{\varepsilon}^{(q)}\mid\hat{e}^{(p-1)}\right]. \tag{2.2.51}$$

From Eq. (2.2.22), the first expectation on the RHS is zero so

$$E\left[\hat{\varepsilon}^{(p)}\hat{\varepsilon}^{(q)}\mid\hat{e}^{(p-1)}\right]=0. \tag{2.2.52}$$

Therefore,

$$E\left[\hat{\varepsilon}^{(p)}\hat{\varepsilon}^{(q)}\right]=E\left[E\left[\hat{\varepsilon}^{(p)}\hat{\varepsilon}^{(q)}\mid\hat{e}^{(p-1)}\right]\right]=0. \tag{2.2.53}$$

As a final note, conditional independence and Markovity both imply each other (Cover, 1991). In particular, this means that the individual states of the Markov process described by Eq. (2.2.43) are such that

$$p\left(\hat{e}^{(i-1)},\hat{e}^{(i+1)}\mid\hat{e}^{(i)}\right)=p\left(\hat{e}^{(i-1)}\mid\hat{e}^{(i)}\right)p\left(\hat{e}^{(i+1)}\mid\hat{e}^{(i)}\right). \tag{2.2.54}$$

Thus, given some state $\hat{e}^{(i)}$, the future states $i+1,\ i+2,\ \cdots$ are conditionally independent from the past states $i-1,\ i-2,\ \cdots$.

Analysis of Cycle Correlations

Before describing the time series representation of the fission source distribution, the cycle correlations and their relationship to the NP operator and its eigenvalues (specifically the dominance ratio, DR) are discussed first. As stated earlier, the larger the eigenvalues the stronger the cycle correlations. The central Eqs. (2.2.40) and (2.2.43) are rewritten for convenience:

$$\mathbf{A}_0\left(\vec{r}'\to\vec{r}\right)=\frac{1}{k_0}\left[H\left(\vec{r}'\to\vec{r}\right)-S_0\left(\vec{r}\right)\right] \tag{2.2.55}$$

$$\hat{e}^{(m+1)}=\mathbf{A}_0\hat{e}^{(m)}+\hat{\varepsilon}^{(m+1)}+O\left(N^{-1/2}\right). \tag{2.2.56}$$

Eq. (2.2.56) is critical to describing the cycle-to-cycle correlations of the error propagation. The source fluctuation $\vec{e}^{(m)}$ can be expanded in terms of the basis of eigenmodes in Eq. (2.1.27) as

$$\hat{e}^{(m)}\left(\vec{r}\right)=\alpha_0^{(m)}S_0\left(\vec{r}\right)+\alpha_1^{(m)}S_1\left(\vec{r}\right)+\alpha_2^{(m)}S_2\left(\vec{r}\right)+\cdots. \tag{2.2.57}$$

Depending on how the operator $\mathbf{A}_0$ affects the fluctuation of the source distribution, the cycle correlations will be stronger or weaker. To understand the effect of the operator, two cases are examined: 1) applying the operator $\mathbf{A}_0$ to the fundamental mode eigenfunction $S_0\left(\vec{r}\right)$ and 2) applying the operator to the non-fundamental mode eigenfunction $S_j\left(\vec{r}\right),\ j\geq 1$. In the first case,

$$\left[\mathbf{A}_0S_0\right]\left(\vec{r}\right)=\frac{1}{k_0}\int\left[H\left(\vec{r}'\to\vec{r}\right)-S_0\left(\vec{r}\right)\right]S_0\left(\vec{r}'\right)dV'$$

$$= \frac{1}{k_0}\left[\int H\left(\vec{r}' \to \vec{r}\right) S_0\left(\vec{r}'\right) dV' - \int S_0\left(\vec{r}\right) S_0\left(\vec{r}'\right) dV'\right]$$

$$= S_0\left(\vec{r}\right) - S_0\left(\vec{r}\right)$$

$$= 0 \tag{2.2.58}$$

where Eq. (2.1.28) was used at the third equality. In the second case,

$$\left[\mathbf{A}_0 S_j\right]\left(\vec{r}\right) = \frac{1}{k_0}\int\left[H\left(\vec{r}' \to \vec{r}\right) - S_0\left(\vec{r}\right)\right] S_j\left(\vec{r}'\right) dV'$$

$$= \frac{1}{k_0}\int H\left(\vec{r}' \to \vec{r}\right) S_j\left(\vec{r}'\right) dV' - \frac{1}{k_0}\int S_0\left(\vec{r}\right) S_j\left(\vec{r}'\right) dV'$$

$$= \frac{k_j}{k_0} S_j\left(\vec{r}\right) - \frac{S_0\left(\vec{r}\right)}{k_0}\int S_j\left(\vec{r}'\right) dV'. \tag{2.2.59}$$

Depending on the integral of the j[th] source eigenfunction over the domain (whether or not this integral is zero) we have one of two possibilities:

$$\left[\mathbf{A}_0 S_j\right]\left(\vec{r}\right) = \frac{k_j}{k_0} S_j\left(\vec{r}\right) \qquad \text{if} \quad \int_V S_j\left(\vec{r}\right) dV = 0,\ j \geq 1 \tag{2.2.60}$$

$$\begin{aligned}\left[\mathbf{A}_0 S_j\right]\left(\vec{r}\right) &= \mathbf{A}_0\left[S_j\left(\vec{r}\right) - S_0\left(\vec{r}\right)\right] \\ &= \frac{k_j}{k_0}\left[S_j\left(\vec{r}\right) - S_0\left(\vec{r}\right)\right] \quad \text{if} \quad \int_V S_j\left(\vec{r}\right) dV \neq 0,\ j \geq 1\end{aligned} \tag{2.2.61}$$

where Eq. (2.1.29) was used to arrive at Eq. (2.2.61). Eqs. (2.2.58), (2.2.60), and (2.2.61) have several important implications. First, as indicated by Eq. (2.2.58), the fundamental eigenmode $S_0\left(\vec{r}\right)$ is mapped identically to zero. Second, since the eigenvalues are ordered $\left|k_0\right| > \left|k_1\right| > \left|k_2\right| > \cdots$, the eigenmodes near the fundamental mode tend to be more correlated than the higher order eigenmodes. For example, $\alpha_1^{(m)} S_1$ and $\alpha_1^{(m+1)} S_1$ from Eq. (2.2.57) tend to be more correlated than $\alpha_5^{(m)} S_5$ and $\alpha_5^{(m+1)} S_5$. Furthermore, the

correlations between higher order eigenmodes decay by a ratio of the respective eigenvalue to the fundamental eigenvalue. This means that the correlations between $\alpha_i^{(m)} S_i$ and $\alpha_i^{(m+j)} S_i$ decay as $\left(k_i/k_0\right)^j$

This analysis also has important implications when considering correlations cycle in differently sized spatial regions of the problem (i.e. whole domain analysis versus a small bin analysis, such as for a fuel pin). If the NP operator $\mathbf{A}_0$ is similarly applied and integrated over a cell *q* then, for the fundamental mode eigenfunction,

$$\int_q \mathbf{A}_0 S_0\left(\vec{r}\right) dV = 0 \tag{2.2.62}$$

and for the non-fundamental mode eigenfunctions

$$\int_q \mathbf{A}_0 S_j\left(\vec{r}\right) dV = \frac{k_j}{k_0} \int_q S_j\left(\vec{r}\right) dV \qquad \text{if } \int_V S_j\left(\vec{r}\right) dV = 0,\ j \geq 1 \tag{2.2.63}$$

$$\int_q \mathbf{A}_0 S_j\left(\vec{r}\right) dV = \frac{k_j}{k_0} \int_q \left[S_j\left(\vec{r}\right) - S_0\left(\vec{r}\right) \right] dV \quad \text{if } \int_V S_j\left(\vec{r}\right) dV \neq 0,\ j \geq 1. \tag{2.2.64}$$

If the spatial bin *q* covers the entire problem domain *V*, Eqs. (2.2.63) and (2.2.64) become

$$\int_V \mathbf{A}_0 S_j\left(\vec{r}\right) dV = 0 \qquad \text{if } \int_V S_j\left(\vec{r}\right) dV = 0,\ j \geq 1 \tag{2.2.65}$$

$$\int_V \mathbf{A}_0 S_j\left(\vec{r}\right) dV = \frac{k_j}{k_0}\left(k_j - k_0\right) \quad \text{if } \int_V S_j\left(\vec{r}\right) dV \neq 0,\ j \geq 1 \tag{2.2.66}$$

where Eqs. (2.1.28) and (2.1.29) are used to arrive at Eq. (2.2.66). These equations highlight an important fact about the cycle correlations. When examining the entire problem domain, the cycle correlations may not be large because many eigenfunctions cancel out when integrated $\left(\text{or } \left| \frac{k_j - k_0}{k_0} \right| << 1 \right)$. However, when examining a small bin,

the eigenfunctions are less likely to cancel out over the integration range, possibly resulting in larger cycle correlations.

In the past, a relation describing the decay of the cycle correlations of the fission source distribution was speculated by MacMillan (1972). He explained that the modes of source fluctuation corresponding to larger eigenvalues decay more slowly than those corresponding to small eigenvalues, resulting in strong correlations. From this observation he speculated that the covariance could be represented as

$$E\left[\xi_k \xi_{k+l}\right] = \lambda_1^l E\left[\eta_1^2\right] + \lambda_2^l E\left[\eta_2^2\right] + \cdots \tag{2.2.67}$$

where λ_n is the n^{th} eigenvalue of the source distribution error propagation and $E\left[\eta_n^2\right]$ is the expectation of the square of the fluctuation of the n^{th} component of the source distribution. ξ_k is the fluctuation of the source distribution, defined such that

$$S_k = S + \xi_k . \tag{2.2.68}$$

Note the similarity between Eq. (2.2.68) and Eq. (2.2.1). Both are describing the same quantity. MacMillan went further to give a conservative estimate of the covariance in Eq. (2.2.67) as

$$E\left[\xi_k \xi_{k+l}\right] \approx \lambda_1^{l-1} E\left[\xi_k \xi_{k+1}\right]. \tag{2.2.69}$$

He implied that the covariance between cycles decayed exponentially according to λ_1, which was later shown to correspond to DR by Ueki (2004). Since the eigenvalues are ordered $k_0 > k_1 > k_2 > \cdots$, this estimate does give an upper bound to correlation decay between cycles. However, using an approach based on MacMillan's estimate in Eq. (2.2.69) can lead to gross overestimation of the variance of the fission source distribution (Nease, 2005).

Section 2.3: Time Series Representation

In this section, the time series representation of the fission source fluctuation is developed. The representation belongs to the framework of the Wold decomposition that states that any non-deterministic zero-mean stationary process can be expressed as a sum of a deterministic process and an infinite order moving average process. The Wold decomposition theory will be explained to assist in understanding how the original attempts at applying time series analysis were developed.

Discrete Representation

Before introducing the time series methodology, we will quickly cover the discrete representation of the equations of importance, assuming *N* (the number of particles per cycle) is sufficiently large: Eqs. (2.2.3), (2.2.23), (2.2.43) – (2.2.45).

$$\vec{e}^{(m+1)} = \mathbf{A}_0 \vec{e}^{(m)} + \vec{\varepsilon}^{(m+1)} \tag{2.3.1}$$

$$E\left[\vec{e}^{(m)}\right] = 0 \tag{2.3.2}$$

$$E\left[\vec{\varepsilon}^{(m)}\right] = 0 \tag{2.3.3}$$

$$E\left[\vec{\varepsilon}^{(m)} \otimes \vec{e}^{(n)}\right] = 0,\ m > n \tag{2.3.4}$$

$$E\left[\vec{\varepsilon}^{(m)} \otimes \vec{\varepsilon}^{(n)}\right] = 0,\ m > n \tag{2.3.5}$$

In these equations, $\vec{e}^{(m)}$ and $\vec{\varepsilon}^{(m)}$ are $p \times 1$ matrices (column vectors with *p* entries), $\mathbf{A}_0$ is assumed to be the discrete $p \times p$ matrix corresponding to the operator in Eq. (2.2.43), and $\otimes$ signifies an outer product (or tensor product). An outer product of two column vectors is equivalent to term by term multiplication, i.e. $\vec{e} \otimes \vec{\varepsilon} \equiv \vec{e}\vec{\varepsilon}^{\mathbf{T}}$, where $\mathbf{T}$ signifies a transpose. *p* stands for the number of spatial bins where the source distribution is tallied.

Wold Decomposition

According to Wold (Priestly, 1981), any stationary process $\mathbf{X}_t$ can be expressed as the sum of two uncorrelated processes $\mathbf{X}_t = \mathbf{U}_t + \mathbf{V}_t$ where $\mathbf{U}_t$ is a moving average process of infinite order and $\mathbf{V}_t$ is a deterministic process. Writing the moving average term as

$$\mathbf{U}_t = \sum_{j=0}^{\infty} \Psi_j \mathbf{Z}_{t-j} \,, \tag{2.3.6}$$

$\mathbf{X}_t$ can be written as

$$\mathbf{X}_t = \sum_{j=0}^{\infty} \Psi_j \mathbf{Z}_{t-j} + \mathbf{V}_t \tag{2.3.7}$$

where the following conditions hold:

$$\Psi_0 = 1 \text{ and } \sum_{j=0}^{\infty} \Psi_j^2 < \infty \tag{2.3.8}$$

$$\{\mathbf{Z}_t\} \sim \mathrm{WN}\left(0, \sigma^2\right), \text{ i.e., } E\left[\mathbf{Z}_t \mathbf{Z}_{t+l}\right] = \begin{cases} \sigma^2 & \text{if } l = 0 \\ 0 & \text{if } l > 0 \end{cases} \text{ for all } t \tag{2.3.9}$$

$$E\left[\mathbf{Z}_t \mathbf{V}_s\right] = 0 \text{ for all } s, t \in \mathbb{Z} \tag{2.3.10}$$

$$\{\mathbf{V}_t\} \text{ is deterministic, i.e., } E\left[\left(\mathbf{V}_t - E\left[\mathbf{V}_t\right]\right)^2\right] = 0 \,. \tag{2.3.11}$$

$\mathbf{Z}_t$ is a white noise process (defined in Eq. (2.3.9)) uncorrelated with $\mathbf{V}_t$. The fluctuation of the fission source distribution $\vec{e}^{(m)}$, which is a stationary zero-mean process by Eqs. (2.3.2) and (2.3.4), can likewise be represented in the form of Eq. (2.3.7). Since the fluctuation is a zero-mean process, there is no reason to expect a non-zero deterministic component $\mathbf{V}_t$ so the source fluctuation can be written as

$$\vec{e}^{(m)} = \Psi\left(B\right)\vec{\varepsilon}^{(m)} = \sum_{j=0}^{\infty} \Psi_j \vec{\varepsilon}^{(m-j)}, \quad \Psi_0 = 1 \tag{2.3.12}$$

where $\vec{\varepsilon}^{(m-j)}$ is white noise (also known as a shock or residual) corresponding to $\mathbf{Z}_t$ introduced above, and *B* is a one-cycle backwards-shift operator such that

$$B\vec{\varepsilon}^{(m)} = \vec{\varepsilon}^{(m-1)} \tag{2.3.13}$$

$$\Psi\left(B\right) = \Psi_0 + \Psi_1 B + \Psi_2 B^2 + \cdots. \tag{2.3.14}$$

Ψ_j are coefficients to be determined. It can be shown that $\vec{e}^{(m)}$ in Eq. (2.3.12) can be manipulated into a weighted sum of past values of itself (with different coefficients) plus a noise component $\vec{\varepsilon}^{(m)}$ by applying the backwards-shift operator $\phi\left(B\right)$ such that

$$\vec{e}^{(m)} = \Psi\left(B\right)\vec{\varepsilon}^{(m)} \tag{2.3.15}$$

$$\phi\left(B\right)\vec{e}^{(m)} = \phi\left(B\right)\Psi\left(B\right)\vec{\varepsilon}^{(m)} \tag{2.3.16}$$

where $\phi\left(B\right) = \phi_0 + \phi_1 B + \phi_2 B^2 + \cdots$. Thus,

$$\phi\left(B\right)\vec{e}^{(m)} = \theta\left(B\right)\vec{\varepsilon}^{(m)} \tag{2.3.17}$$

where $\theta\left(B\right) = \phi\left(B\right)\Psi\left(B\right) = \theta_0 + \theta_1 B + \theta_2 B^2 + \cdots$. If summations of $\phi\left(B\right)$ and $\theta\left(B\right)$ are both truncated to *p* and *q* respectively, such that

$$\sum_{i=0}^{p} \phi_i \vec{e}^{(m-i)} = \sum_{j=0}^{q} \theta_j \vec{\varepsilon}^{(m-j)}, \quad \phi_0 = \theta_0 = 1, \tag{2.3.18}$$

then the resulting process is known as an autoregressive moving average process of order *p* and *q*, commonly abbreviated as ARMA(*p*,*q*). This explanation of the Wold decomposition will be necessary in understanding the process of calculating DR using an ARMA representation, which will be explained next.

Binary Half-Domain Fitting Method

With Eqs. (2.3.1) – (2.3.5) and an understanding of the Wold decomposition, we can proceed to the autoregressive moving average (ARMA) representation that will allow for the computation of the dominance ratio, $\mathrm{DR} = k_1/k_0$ First, an observation matrix $\mathbf{C}$ is applied to the fluctuation. This can be any matrix with *p* columns, where *p* is the number of bins used to tally the fission source

$$\vec{y}^{(m)} = \mathbf{C}\vec{e}^{(m)}. \tag{2.3.19}$$

This forms a linear observation $\vec{y}^{(m)}$ and it was shown (Ueki, 2004) that after applying $\mathbf{C}$, the observation $\vec{y}^{(m)}$ and noise $\vec{\varepsilon}^{(m)}$ also satisfy the conditions of the Wold decomposition in Eq. (2.3.18) so that

$$a(B)\vec{y}^{(m)} = E(B)\vec{\varepsilon}^{(m)} \tag{2.3.20}$$

$$\sum_{i=0}^{p} a_i \vec{y}^{(m-i)} = \sum_{j=0}^{p-1} E_j \vec{\varepsilon}^{(m-j)} \tag{2.3.21}$$

where the a_i's and E_i's are coefficients. The ARMA orders were derived to be *p* and $p-1$. It was also shown that the a_i's are the coefficients of the characteristic polynomial of the NP matrix $\mathbf{A}_0$

$$f(\lambda) = \lambda^p + \sum_{n=1}^{p} a_n \lambda^{p-n} = \left|\lambda \mathrm{I} - \mathbf{A}_0\right|; \ \ (\mathrm{I} \text{ being the identity matrix}) \tag{2.3.22}$$

which satisfy

$$f(k_i/k_0) = 0 \text{ for } i = 1, 2, \ldots \text{ when } p >> 1 \text{ (continuous limit)}. \tag{2.3.23}$$

Also, the E_i's in Eq. (2.3.21) can be represented using the NP matrix $\mathbf{A}_0$ as

$$E_i = \mathbf{C}\left(\mathbf{A}_0^i + a_1\mathbf{A}_0^{i-1} + \cdots + a_i\mathbf{I}\right), \ \ E_0 = \mathbf{C}. \tag{2.3.24}$$

This is a significant result because the largest zero of the characteristic polynomial in Eq. (2.3.22) corresponds to DR. Thus, to compute DR, we need only to determine the coefficients of the ARMA process and solve the polynomial.

The observation matrix for the k_0 confidence interval estimation is the $1\times p$ matrix (row vector):

$$\mathbf{C}_{k_{eff}} = [1,1,\ldots,1]. \tag{2.3.25}$$

Since p can be any positive integer in terms of the observation $\mathbf{C}_{k_{eff}}\vec{e}^{(m)}$, the autocovariance estimation of a k_0 series can be reduced to choosing the most appropriate model from ARMA(1,0)=AR(0) and ARMA(p, p–1), p > 1.

To compute the eigenvalue ratio k_1/k_0, Ueki showed (2004) that a simple two-bin scheme with a binary observation matrix $\mathbf{C}=[1,0]$ $(p=2)$ and an ARMA(2,1) fitting consistently produces accurate estimates for a variety of problems. This observation matrix is equivalent to a larger bin scheme where $\mathbf{C}=[1,\cdots,1,0,\cdots,0]$ $(p>>1)$. The success of such a simple scheme is understandable considering the eigenmode corresponding to DR. According to diffusion theory, the first eigenfunction of a homogeneous slab reactor $0\le x\le L$ with vacuum boundary conditions (Parsons, 2003) is $\sin(2\pi x/L)$, meaning that from $0<x<L/2$ the value is positive and from $L/2<x<L$ the value is negative. Thus, an observation matrix $\mathbf{C}=[1,0]$ attempts to capture this feature. Perhaps an observation matrix $\mathbf{C}=[1,-1]$ would be more appropriate in this case to properly model the eigenfunction, but the ARMA(2,1) fitting (where the order p = 2 was chosen corresponding to the two source tally bins) can still draw enough information

from the applied binary observation matrix to calculate an accurate estimate. This is an important aspect of the methodology: *the fluctuation of the binned source contains uncompromised information of the eigenvalue ratio* k_i/k_0 *if the complete cancellation of the corresponding eigenmode does not occur*. This is the significance of the time series methodology that was illustrated in Figure 1 in Chapter 1.

Through this discussion, several of the strengths and drawbacks of this method have been highlighted. Highly accurate estimates can be obtained from simple binning schemes, even for very complex problems. However, the solution requires knowledge of transport solutions from the user to properly choose the observation matrix. Also, the ARMA fitting method can be very complex since it uses non-linear least squares iterations for the preliminary parameter guesses, often requiring fine tuning from the user for convergence control. It also backwards-estimates parameters from the beginning of the series and it can be difficult to automate how many backward cycles are needed. These are the issues which are addressed with the Coarse Mesh Projection Method, which uses this time series methodology as a foundation to calculate any desired eigenvalue ratio with minimal input from the user.

Chapter 3: Eigenvalue Estimation

The Coarse Mesh Projection Method (CMPM) takes an alternate approach to the application of time series techniques to address the shortcomings of previous methods (the need for a complicated ARMA fitting), while retaining the strengths (high accuracy without large memory intensive binning schemes). Parts of this method are similar in form to Principal Oscillation Patterns (POPs) analysis, which is often used in atmospheric research (Storch, 1999). As will be shown, the method is not limited to calculating only DR; it extends to other higher-order eigenvalue ratios as well.

In the first section of this chapter, CMPM process is derived, including error estimation of the results. This is followed by a discussion on selecting bin schemes that prevent cancellation of the desired eigenmode while ensuring cancellation of all others.

Section 3.1: Coarse Mesh Projection Method

The Coarse Mesh Projection Method has several parts. The Noise Propagation Matrix must be computed first so that the eigenvectors of it can be calculated. One of these eigenvectors is chosen as the projection vector and applied to the source fluctuation. A time series fitting is performed on the projected series and the autocorrelation coefficient is calculated. As will be shown, this coefficient is the desired eigenvalue ratio.

Noise Propagation Matrix

The first task is to properly estimate the discrete form of the NP matrix $\mathbf{A}_0$. Eqs. (2.3.1) – (2.3.5) are rewritten for convenience:

$$\vec{e}^{(m+1)} = \mathbf{A}_0 \vec{e}^{(m)} + \vec{\varepsilon}^{(m+1)} \tag{3.1.1}$$

$$E\left[\vec{\varepsilon}^{(m)}\right] = 0 \tag{3.1.2}$$

$$E\left[\vec{e}^{(m)}\right] = 0 \tag{3.1.3}$$

$$E\left[\vec{\varepsilon}^{(m)} \otimes \vec{e}^{(n)}\right] = 0, \quad m > n \tag{3.1.4}$$

$$E\left[\vec{\varepsilon}^{(m)} \otimes \vec{\varepsilon}^{(n)}\right] = 0, \quad m > n \tag{3.1.5}$$

Eq. (3.1.1) can be multiplied throughout by $\vec{e}^{(m)}$ as an outer product yielding

$$\vec{e}^{(m+1)} \otimes \vec{e}^{(m)} = \mathbf{A}_0 \vec{e}^{(m)} \otimes \vec{e}^{(m)} + \vec{\varepsilon}^{(m+1)} \otimes \vec{e}^{(m)}. \tag{3.1.6}$$

Taking the expectation of this and using the results of Eq. (3.1.4) gives

$$E\left[\vec{e}^{(m+1)} \otimes \vec{e}^{(m)}\right] = \mathbf{A}_0 E\left[\vec{e}^{(m)} \otimes \vec{e}^{(m)}\right]. \tag{3.1.7}$$

Defining a general covariance matrix as

$$\mathbf{L}_i \equiv E\left[\vec{e}^{(m+i)} \otimes \vec{e}^{(m)}\right] \tag{3.1.8}$$

such that the cross and lag covariances are

$$\mathbf{L}_0 = E\left[\vec{e}^{(m)} \otimes \vec{e}^{(m)}\right] \tag{3.1.9}$$

$$\mathbf{L}_1 = E\left[\vec{e}^{(m+1)} \otimes \vec{e}^{(m)}\right] \tag{3.1.10}$$

the matrix $\mathbf{A}_0$ can be expressed as

$$\mathbf{A}_0 = \mathbf{L}_1 \mathbf{L}_0^{-1} \tag{3.1.11}$$

Thus, if $\left(\vec{e}^{(m)}\right)^{\mathbf{T}} = \left(e_1^{(m)}, e_2^{(m)}, \cdots, e_p^{(m)}\right)$, the explicit form of $\mathbf{A}_0$ can be written as

$$\mathbf{A}_0 = \begin{bmatrix} E\left[e_1^{(m+1)} \otimes e_1^{(m)}\right] \cdots E\left[e_1^{(m+1)} \otimes e_p^{(m)}\right] \\ \vdots \quad\quad \vdots \quad\quad \vdots \\ E\left[e_p^{(m+1)} \otimes e_1^{(m)}\right] \cdots E\left[e_p^{(m+1)} \otimes e_p^{(m)}\right] \end{bmatrix} \begin{bmatrix} E\left[e_1^{(m)} \otimes e_1^{(m)}\right] \cdots E\left[e_1^{(m)} \otimes e_p^{(m)}\right] \\ \vdots \quad\quad \vdots \quad\quad \vdots \\ E\left[e_p^{(m)} \otimes e_1^{(m)}\right] \cdots E\left[e_p^{(m)} \otimes e_p^{(m)}\right] \end{bmatrix}^{-1} \tag{3.1.12}$$

and the matrix $\mathbf{A}_0$ can be evaluated through the computation of the sample cross and lag covariance matrices $\mathbf{L}_0$ and $\mathbf{L}_1$.

If the bins are made sufficiently fine ($p >> 1$), then Eqs. (2.2.60) and (2.2.61) imply that the eigenvalues of the discrete version of $\mathbf{A}_0$ approach the eigenvalues k_i/k_0, $i = 1, 2, \ldots$ of the continuous operator. In fact, k_i/k_0 could be directly calculated from $\mathbf{A}_0$ via matrix solvers assuming a sufficient number of bins, cycles, and particles per cycle. This approach would suffer from the same drawbacks as the fission matrix method, however, becoming computationally prohibitive due to the large numbers of bins needed to reduce the discretization error. Thus, it is preferable to use a computational approach that is free of the effects of discretization error, which is why a method based on time series analysis and guided by the eigenvectors of $\mathbf{A}_0$ is pursued.

Projection Process

The eigenvalue problem of $\mathbf{A}_0$ is

$$\mathbf{A}_0 \vec{b}_i = \lambda_i \vec{b}_i \qquad i = 1, \cdots, p \tag{3.1.13}$$

$$\mathbf{A}_0^* \vec{d}_j = \lambda_j^* \vec{d}_j \quad j = 1, \cdots, p\,. \tag{3.1.14}$$

$\mathbf{A}_0^*$ is the adjoint (or conjugate transpose) of matrix of $\mathbf{A}_0$. Since $\mathbf{A}_0$ is real, the adjoint is equal to the transpose $\left(\mathbf{A}_0^* = \mathbf{A}_0^{\mathrm{T}}\right)$. It is well known that $\det\left(\mathbf{A}_0 - \lambda I\right) = \det\left(\mathbf{A}_0^T - \lambda I\right)$

(where det is the determinant and *I* is the identity matrix), which implies that $\mathbf{A}_0$ and $\mathbf{A}_0^{\mathbf{T}}$ share the same set of eigenvalues, i.e.,

$$\lambda_i = \lambda_j^* \quad \text{for} \quad i = j\,. \tag{3.1.15}$$

In addition, their eigenvectors satisfy

$$\left\langle \vec{b}_i, \vec{d}_j \right\rangle = 0 \quad \text{if} \quad \lambda_i \neq \lambda_j^* \quad \text{and} \quad i \neq j \tag{3.1.16}$$

where $\langle \cdot \rangle$ indicates an inner product (or dot product) of the two column vectors. In other notation, this is equivalent to $\left\langle \vec{d}, \vec{b} \right\rangle = \vec{d}^{\mathbf{T}} \vec{b}$. Eq. (3.1.16) can easily be proven. We know that for some $1 \leq i, j \leq p$

$$\mathbf{A}_0 \vec{b}_i = \lambda_i \vec{b}_i \tag{3.1.17}$$

$$\mathbf{A}_0^{\mathbf{T}} \vec{d}_j = \lambda_j \vec{d}_j\,. \tag{3.1.18}$$

Taking the transpose of each side of Eq. (3.1.18) yields

$$\left(\mathbf{A}_0^{\mathbf{T}} \vec{d}_j \right)^{\mathbf{T}} = \left(\lambda_j \vec{d}_j \right)^{\mathbf{T}} \tag{3.1.19}$$

$$\vec{d}_j^{\,\mathbf{T}} \mathbf{A}_0 = \lambda_j \vec{d}_j^{\,\mathbf{T}}\,. \tag{3.1.20}$$

Thus, if $\vec{d}_j^{\,\mathbf{T}}$ is applied to the LHS in Eq. (3.1.17), there are two possible results depending on which operation is performed first:

$$\vec{d}_j^{\,\mathbf{T}} \left(\mathbf{A}_0 \vec{b}_i \right) = \lambda_i \vec{d}_j^{\,\mathbf{T}} \vec{b}_i \tag{3.1.21}$$

or

$$\left(\vec{d}_j^{\,\mathbf{T}} \mathbf{A}_0 \right) \vec{b}_i = \lambda_j \vec{d}_j^{\,\mathbf{T}} \vec{b}_i\,. \tag{3.1.22}$$

Subtracting these two equations, it is clear that

$$\begin{aligned} 0 &= \lambda_j \vec{d}_j^{\mathrm{T}} \vec{b}_i - \lambda_i \vec{d}_j^{\mathrm{T}} \vec{b}_i \\ &= \left(\lambda_j - \lambda_i\right) \vec{d}_j^{\mathrm{T}} \vec{b}_i \end{aligned} \tag{3.1.23}$$

implying that either $\lambda_i = \lambda_j$ or $\vec{d}_j^{\mathrm{T}} \vec{b}_i = 0$.

It is important to note that $\mathbf{A}_0$ is not a symmetric matrix; its eigenvalues are not guaranteed to be real. Even when analyzing problems that are proven to have all real eigenvalues there is a possibility to obtain complex results from this estimation. This topic will be considered in the next chapter.

To utilize Eqs. (3.1.13) and (3.1.14), Eq. (3.1.1) must be applied recursively

$$\vec{e}^{(m+1)} = \mathbf{A}_0^{m+1} \vec{e}^{(0)} + \mathbf{A}_0^{m} \vec{\varepsilon}^{(1)} + \mathbf{A}_0^{m-1} \vec{\varepsilon}^{(2)} + \cdots + \vec{\varepsilon}^{(m+1)}. \tag{3.1.24}$$

Next, using vectors $\vec{b}_i$ as the basis, $\vec{e}^{(0)}$ and $\vec{\varepsilon}^{(i)}$ can be expanded as

$$\vec{e}^{(0)} = \alpha_1 \vec{b}_1 + \alpha_2 \vec{b}_2 + \cdots + \alpha_p \vec{b}_p \tag{3.1.25}$$

$$\vec{\varepsilon}^{(i)} = \eta_1^{(i)} \vec{b}_1 + \eta_2^{(i)} \vec{b}_2 + \cdots + \eta_p^{(i)} \vec{b}_p. \tag{3.1.26}$$

where the α_i and η_i are arbitrary coefficients. These expansions can then be substituted into Eq. (3.1.24) and combined according to the respective basis. Applying Eq. (3.1.13) yields

$$\begin{aligned} \vec{e}^{(m+1)} = &\left(\alpha_1 \lambda_1^{m+1} + \eta_1^{(1)} \lambda_1^{m} + \eta_1^{(2)} \lambda_1^{m-1} + \cdots + \eta_1^{(m)} \lambda_1 + \eta_1^{(m+1)}\right) \vec{b}_1 \\ &+ \cdots \\ &+ \left(\alpha_p \lambda_p^{m+1} + \eta_p^{(1)} \lambda_p^{m} + \eta_p^{(2)} \lambda_p^{m-1} + \cdots + \eta_p^{(m)} \lambda_p + \eta_p^{(m+1)}\right) \vec{b}_p \end{aligned} \tag{3.1.27}$$

Now the orthogonal properties of the eigenvectors in Eq. (3.1.16) can be taken advantage of by taking the projection onto some $\vec{d}_i$, $1 \le i \le p$. This is equivalent to taking the inner product of the quantities. This projection vector can be any eigenvector corresponding to the desired eigenvalue. This yields

$$\begin{aligned}\left\langle \vec{d}_i, \vec{e}^{(m+1)} \right\rangle = & \left(\alpha_1 \lambda_1^{m+1} + \eta_1^{(1)} \lambda_1^{m} + \eta_1^{(2)} \lambda_1^{m-1} + \cdots + \eta_1^{(m)} \lambda_1 + \eta_1^{(m+1)} \right) \left\langle \vec{d}_i, \vec{b}_1 \right\rangle \\ & + \cdots \\ & + \left(\alpha_p \lambda_p^{m+1} + \eta_p^{(1)} \lambda_p^{m} + \eta_p^{(2)} \lambda_p^{m-1} + \cdots + \eta_p^{(m)} \lambda_p + \eta_p^{(m+1)} \right) \left\langle \vec{d}_i, \vec{b}_p \right\rangle \end{aligned} \tag{3.1.28}$$

Before taking advantage of Eq. (3.1.16) and removing orthogonal terms, the possibility of multiplicity (degeneracy of the eigenvalues) must be considered (where $\lambda_{i-j} = \cdots = \lambda_{i-1} = \lambda_i = \lambda_{i+1} = \cdots = \lambda_{i+k}$ and $\lambda_i \neq \lambda_l,\ l < i-j,\ l > i+k$) in the system. This occurs frequently in problems with geometric symmetry, resulting in

$$\begin{aligned}\left\langle \vec{d}_i, \vec{e}^{(m+1)} \right\rangle = & \left(\alpha_{i-j} \lambda_i^{m+1} + \eta_{i-j}^{(1)} \lambda_i^{m} + \eta_{i-j}^{(2)} \lambda_i^{m-1} + \cdots + \eta_{i-j}^{(m)} \lambda_i + \eta_{i-j}^{(m+1)} \right) \left\langle \vec{d}_i, \vec{b}_{i-j} \right\rangle \\ & + \cdots \\ & + \left(\alpha_{i+k} \lambda_i^{m+1} + \eta_{i+k}^{(1)} \lambda_i^{m} + \eta_{i+k}^{(2)} \lambda_i^{m-1} + \cdots + \eta_{i+k}^{(m)} \lambda_i + \eta_{i+k}^{(m+1)} \right) \left\langle \vec{d}_i, \vec{b}_{i+k} \right\rangle \end{aligned} \tag{3.1.29}$$

If $m+1$ is replaced by m in Eq. (3.1.29)

$$\begin{aligned}\left\langle \vec{d}_i, \vec{e}^{(m)} \right\rangle = & \left(\alpha_{i-j} \lambda_i^{m} + \eta_{i-j}^{(1)} \lambda_i^{m-1} + \eta_{i-j}^{(2)} \lambda_i^{m-2} + \cdots + \eta_{i-j}^{(m-1)} \lambda_i + \eta_{i-j}^{(m)} \right) \left\langle \vec{d}_i, \vec{b}_{i-j} \right\rangle \\ & + \cdots \\ & + \left(\alpha_{i+k} \lambda_i^{m} + \eta_{i+k}^{(1)} \lambda_i^{m-1} + \eta_{i+k}^{(2)} \lambda_i^{m-2} + \cdots + \eta_{i+k}^{(m-1)} \lambda_i + \eta_{i+k}^{(m)} \right) \left\langle \vec{d}_i, \vec{b}_{i+k} \right\rangle \end{aligned} \tag{3.1.30}$$

Notice the similarities between the above two equations. If λ_i is multiplied throughout Eq. (3.1.30), it can be substituted into Eq. (3.1.29) and rewritten as

$$\left\langle \vec{d}_i, \vec{e}^{(m+1)} \right\rangle = \lambda_i \left\langle \vec{d}_i, \vec{e}^{(m)} \right\rangle + \eta_{i-j}^{(m+1)} \left\langle \vec{d}_i, \vec{b}_{i-j} \right\rangle + \cdots + \eta_{i+k}^{(m+1)} \left\langle \vec{d}_i, \vec{b}_{i+k} \right\rangle . \tag{3.1.31}$$

This can be further reduced to

$$\left\langle \vec{d}_i, \vec{e}^{(m+1)} \right\rangle = \lambda_i \left\langle \vec{d}_i, \vec{e}^{(m)} \right\rangle + \left\langle \vec{d}_i, \eta_{i-j}^{(m+1)} \vec{b}_{i-j} + \cdots + \eta_{i+k}^{(m+1)} \vec{b}_{i+k} \right\rangle . \tag{3.1.32}$$

Recalling Eqs. (3.1.16), (3.1.26), and the multiplicity assumption of λ_i, the right most term is nothing more than

$$\left\langle \vec{d}_i, \eta_{i-j}^{(m+1)} \vec{b}_{i-j} + \cdots + \eta_{i+k}^{(m+1)} \vec{b}_{i+k} \right\rangle = \left\langle \vec{d}_i, \vec{\varepsilon}^{(m+1)} \right\rangle , \tag{3.1.33}$$

leaving

$$\left\langle \vec{d}_i, \vec{e}^{(m+1)} \right\rangle = \lambda_i \left\langle \vec{d}_i, \vec{e}^{(m)} \right\rangle + \left\langle \vec{d}_i, \vec{\varepsilon}^{(m+1)} \right\rangle . \tag{3.1.34}$$

If the components of a scalar time series are defined as

$$y^{(m)} \equiv \left\langle \vec{d}_i, \vec{e}^{(m)} \right\rangle \tag{3.1.35}$$

$$z^{(m)} \equiv \left\langle \vec{d}_i, \vec{\varepsilon}^{(m)} \right\rangle , \tag{3.1.36}$$

then Eqs. (3.1.35) and (3.1.36) imply that $y^{(m)}$ satisfies

$$y^{(m+1)} = \lambda_i y^{(m)} + z^{(m+1)} . \tag{3.1.37}$$

In addition, using Eqs. (3.1.2), (3.1.3) and (3.1.5)

$$E\left[y^{(m)} \right] = E\left[\left\langle \vec{d}_i, \vec{e}^{(m)} \right\rangle \right] = \left\langle \vec{d}_i, E\left[\vec{e}^{(m)} \right] \right\rangle = 0 \tag{3.1.38}$$

$$E\left[z^{(m)} \right] = E\left[\left\langle \vec{d}_i, \vec{\varepsilon}^{(m)} \right\rangle \right] = \left\langle \vec{d}_i, E\left[\vec{\varepsilon}^{(m)} \right] \right\rangle = 0 \tag{3.1.39}$$

$$\begin{aligned} E\left[z^{(m)} z^{(n)} \right] &= E\left[\left\langle \vec{d}_i, \vec{\varepsilon}^{(m)} \right\rangle \left\langle \vec{d}_i, \vec{\varepsilon}^{(n)} \right\rangle \right] \\ &= \left\langle \vec{d}_i \otimes \vec{d}_i, E\left[\vec{\varepsilon}^{(m)} \otimes \vec{\varepsilon}^{(n)} \right] \right\rangle = 0, \quad m > n. \end{aligned} \tag{3.1.40}$$

The second equality in Eq. (3.1.40) is proven in Appendix A.

Thus, $y^{(m)}$ follows an autoregressive process of order one [AR(1)] with the i^{th} eigenvalue of $\mathbf{A}_0$ as the autocorrelation coefficient. An AR(1) process is the simplest time series to solve and is guaranteed to be stable if the coefficients are such that $|\lambda_i| < 1$. Since the eigenvalues are ordered $|k_0| > |k_1| > |k_2| > \cdots$, the condition of the ratios being less than unity is always satisfied.

Time Series Autoregressive Process

To solve for the coefficient λ_i in Eq. (3.1.37), $y^{(m)}$ is multiplied throughout and the expectation of the quantities is taken:

$$E\left[y^{(m+1)}y^{(m)}\right] = \lambda_i E\left[y^{(m)}y^{(m)}\right] + E\left[z^{(m+1)}y^{(m)}\right]. \tag{3.1.41}$$

Using Eq. (3.1.4) the last term on the RHS is

$$\begin{aligned} E\left[z^{(m+1)}y^{(m)}\right] &= E\left[\left\langle \vec{d}_i, \vec{\varepsilon}^{(m+1)} \right\rangle \left\langle \vec{d}_i, \vec{e}^{(m)} \right\rangle\right] \\ &= \left\langle \vec{d}_i \otimes \vec{d}_i, E\left[\vec{\varepsilon}^{(m+1)} \otimes \vec{e}^{(m)}\right] \right\rangle = 0 \end{aligned} \tag{3.1.42}$$

(the second inequality is proven in Appendix A) allowing Eq. (3.1.41) to be reduced to

$$E\left[y^{(m+1)}y^{(m)}\right] = \lambda_i E\left[y^{(m)}y^{(m)}\right] \tag{3.1.43}$$

and the coefficient can be solved for as

$$\lambda_i = \frac{E\left[y^{(m+1)}y^{(m)}\right]}{E\left[y^{(m)}y^{(m)}\right]}. \tag{3.1.44}$$

These are covariance terms by definition. In fact, the denominator is simply the variance of the new times series and the numerator is the lag one covariance of the time series.

The described projection method has been termed the Coarse Mesh Projection Method (CMPM). This projection method offers numerous advantages over other methods to calculate eigenvalues. As was stated in the previous section, $\lambda_i \approx k_i/k_0$ can be computed directly from the noise propagation matrix $\mathbf{A}_0$ using matrix solvers, but those estimates will contain discretization error due to the geometric sizes of bins, much like the fission matrix method. Previous work has shown (Ueki, 2004) that discretization error does not exist for the computation of k_1/k_0 if it is obtained directly via the time series analysis of the fission source fluctuation. The numerical results in that work

convincingly show that two source bins and a projection vector of $\vec{p} = [1, 0]$ (known as a half-domain fitting) are enough to get an unbiased estimate of k_1/k_0 if the first mode eigenfunction $\vec{S}_1$ does not completely cancel out over the chosen half domain by $\vec{p}$; the fluctuation contains uncompromised information about DR. However, the half domain fitting approach is based on the Autoregressive Moving Average model of orders *p* and $p-1$ (ARMA($p, p-1$)), which was derived via the Akaike's theory of Markovian representation (Akaike, 1976). This ARMA model requires preliminary guesses of the coefficients for the least square implementation, which are normally computed by the method of moments for the AR part and iterative calculations for the MA part. The least square calculation is non-linear and iterative, and requires backwards estimation (Box, 1997; Visual Numerics, 1997) from the initial value of the time series ($\vec{e}^{(0)}$ in this work), which can be difficult to automate. In some cases the fluctuation can departure from its typical behavior, forcing the software user to fine-tune the number of time steps for the backward estimation.

The Coarse Mesh Projection Method is free of such problems. According to the derived theory, a simple AR(1) fitting is enough for any desired eigenvalue. Since $|\lambda_i| < 1$, $i \geq 1$, the fitting is guaranteed to be stable (Box, 1997). This is a significant improvement over previous methods and will allow for nearly black-box DR calculations, requiring very little input from a code user due to the ease of the AR calculation. This is a preferred feature for Monte Carlo code developers who attempt to make DR computations a part of production codes like MCNP.

Error Estimation

The error of the estimated eigenvalue ratio is measured according to a technique described by Box and Jenkins (1997). Since the eigenvalue ratio is the autocorrelation coefficient of an AR(1) process, we can estimate the error of the desired ratio as the error of the AR(1) coefficient. The variance of an estimated lag *k* autocorrelation coefficient of a stationary Normal process is given by

$$\mathrm{var}\left[r_k\right] \simeq \frac{1}{N}\sum_{\upsilon=-\infty}^{\infty}\left\{\rho_\upsilon^2 + \rho_{\upsilon+k}\rho_{\upsilon-k} - 4\rho_k\rho_{\upsilon-k} + 2\rho_\upsilon^2\rho_k^2\right\}. \tag{3.1.45}$$

where r_k is the estimated lag k autocorrelation, ρ_k is the actual lag k autocorrelation and N is the number of active cycles. No assumption about the process $\vec{e}^{(m)}$ had been made, however this error estimator assumes the process to be Normal. As the number of cycles increases, we expect this assumption to be valid because $\vec{e}^{(m)}$ is the sum of $\mathbf{A}_0^i\vec{\varepsilon}^{(m-i)}$, $i = 0,1,2,\cdots$ by Eq. (3.1.24) and $\vec{\varepsilon}^{(m)}$ are uncorrelated by Eq. (2.2.21). Also, the linearity of Eq. (3.1.1) assumes that there are a sufficient number of neutrons causing fission events in each individual tally bin, such that every binned source can be assumed Normal. For autocorrelation functions that damps out exponentially, such as in the AR(1) case where $\rho_k = \phi^{|k|}$ for $\left(-1 < \phi < 1\right)$, Box and Jenkins (1997) said that Eq. (3.1.45) can be further estimated as

$$\mathrm{var}\left[r_k\right] \simeq \frac{1}{N}\left[\frac{\left(1+\phi^2\right)\left(1-\phi^{2k}\right)}{1-\phi^2} - 2k\phi^{2k}\right]. \tag{3.1.46}$$

In particular, for a lag 1 case (i.e. $k = 1$), this reduces to

$$\mathrm{var}\left[r_1\right] \simeq \frac{1}{N}\left(1-\phi^2\right). \tag{3.1.47}$$

This is the expression that is used to estimate the variance of the autocorrelation coefficient, i.e. the eigenvalue ratio.

Interestingly, the number of particles per cycle used does not appear in the error estimator, suggesting that the calculated eigenvalue ratio is independent of it. While a formal proof is not presented, numerical results will be presented showing that this is indeed the case for a sufficiently large number of particles per cycle. Since CMPM computes the ratio of eigenvalues k_i/k_0, it is theorized that the effect of particles per cycle effectively cancels out when performing this calculation. To determine the actual eigenvalue k_i, the ratio k_i/k_0 must be multiplied by fundamental mode eigenvalue k_0 from the MC calculation. This eigenvalue k_0 is dependent on the number of particles per cycle, which shows up in that respective error calculation.

Section 3.2: Mesh Analysis

Even though CMPM is free of discretization error, we must still consider the binning system for the fission source fluctuation. Time series methods analyze fluctuations and, therefore, do not suffer from discretization error in the same sense as directly solving the NP matrix. However, the fluctuation being analyzed must exclusively contain the desired eigenmode. In this way, accurate eigenvalue estimation is possible regardless of the mesh size as long as 1) the complete cancellation of the desired eigenmode does not occur over the mesh and 2) the undesired modes are removed. This section develops the relation between the source mesh and the eigenvalues of interest so that those two conditions can occur automatically (in the case of DR) without input from the user.

It has been shown (Ueki, 2003) that if the eigenfunction $S_1(\vec{r})$ completely cancels over the bin, then the fluctuating mode associated with k_1/k_0 will disappear as well. The implication with higher eigenvalue ratios is assumed to be similar. Thus, to extract information about a particular eigenvalue ratio, the corresponding mode must not completely cancel out over the bin. The question becomes, is there a binning scheme of general nature that always prevents the cancellation of the desired eigenfunction from occurring?

The largest eigenvalue ratio k_1/k_0 known as the dominance ratio, DR, is discussed first. The fundamental eigenfunction $S_0(\vec{r})$ is everywhere non-negative; it does not change sign. The first eigenfunction $S_1(\vec{r})$ changes sign once over the domain if simply put. For example, Figure 2 shows the first eigenmode of a homogeneous slab reactor with vacuum boundary condition and no external source according to diffusion theory (Parsons, 2003).

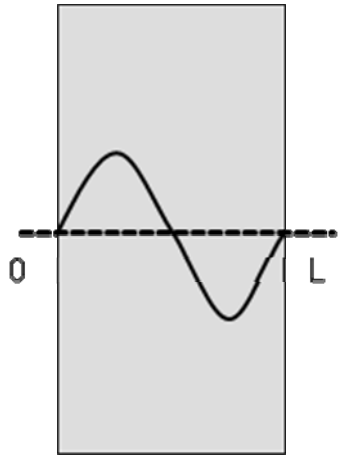

Figure 2: First Eigenmode of 1-D homogeneous Slab

While other one-dimensional problems may not have such a simple eigenmode, the first non-fundamental eigenmode for any problem is guaranteed to only change sign once across the domain. If a single bin is applied over the range $0 \le x \le L$, the first eigenfunction will only completely cancel when integrated over the range. Instead, if two bins are applied from $0 \le x \le L/2$ and $L/2 \le x \le L$, then the complete cancellation will not occur when integrated over each bin. Some information about the mode in each bin will be preserved.

For a two-dimensional case, consider the scenario illustrated in Figure 3. If the geometry and material distribution are symmetric with respect to x and y Cartesian coordinate axes, the first eigenfunction changes sign once with respect to these axes. If the geometry and material distribution are diagonally symmetric, the first eigenfunction changes sign across the diagonal lines. To pick up the fluctuation associated with the first mode, the integral of source distribution should not cancel over at least one of the bins.

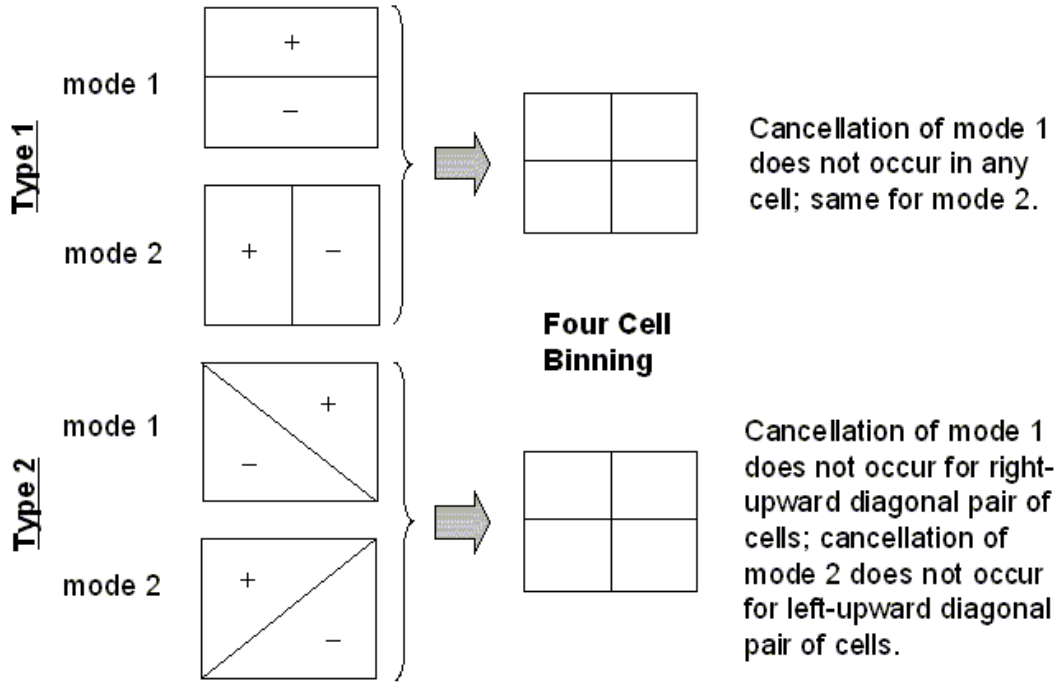

Figure 3: First and Second Non-Fundamental Eigenmodes of 2-D Problem and Four Cell Binning Scheme

This condition is satisfied by the four bin mesh in Figure 3. Even for problems without any symmetric material placement, the complete cancellation of the first eigenfunction over all four bins in Figure 2 will not occur, since the first eigenfunction only changes sign once. Similarly, the number of bins is eight for three-dimensional rectangular geometry. An analysis comparing accuracy versus mode cancellation will be given in the next chapter.

In general, partial to complete cancellation of the higher eigenmodes is likely to occur in all four bins in Figure 3 due to the frequent sign changes. For this reason, simple bin schemes cannot be applied to compute higher eigenvalue ratios. One observation can be made, however. The absolute minimum number of bins necessary to calculate the i^{th} eigenvalue ratio in any problem is $i+1$. This is because the number of source tally bins p

corresponds to the size of the NP matrix ($p \times p$), implying that at most only p eigenvalues can be obtained. In addition, one of the eigenvalues always corresponds to the $S_0(\vec{r})$ eigenmode. Thus, for example, to calculate k_3/k_0 , an absolute minimum of four source tally bins are needed.

The actual implementation of the bin tally schemes is described in Appendix B. Source tallies were usually generated using fine bins schemes and saved in file format for later use. This allowed us to analyze the problem using CMPM multiple times with varying bin schemes (by combining bins) without having to re-run the problem, since many of the validation runs took several days to complete.

Chapter 4: Method Implementation

This chapter covers the full range of results obtained after implementing CMPM. This includes eigenvalue ratio results for 1-D, 2-D, and 3-D mono-energetic problem types using a personal research code and results from implementing the method into the production code MCNP (X-5, 2003) including continuous-energy problems.

Section 4.1: CMPM Eigenvalue Ratio Results

The first results presented are the eigenvalue ratios for 1-D, 2-D, and 3-D mono-energetic problem types. DR calculations are provided, followed by higher-order eigenvalue ratios. Bias checks are then made by running multiple replicas of different problems. The mean is estimated as the average of the replicas and the confidence interval containment rate of the error estimator is checked.

Accuracy Verification

The accuracy of CMPM was first checked by performing eigenvalue ratio calculations for four different problem types. In all four cases, the problems were run with a very large number of particles per cycle and active cycles to gauge the accuracy of the method. The ratios were computed using different bin schemes ranging from the simplest possible (the minimum number of bins in each coordinate direction) to larger bin schemes (on the order of 100 – 200 bins total). The actual method used to reduce bin

schemes down to coarse meshes is described in Appendix B. Very large numbers of particles per cycle and active cycles were used to obtain solid benchmark results.

The first problem is a mono-energetic, homogeneous 1-D slab with isotropic scattering and vacuum boundary conditions using 200 inactive cycles, 10,000 active cycles, 10,000 particles per cycle. The geometric and material properties are as follows: Slab thickness 200 cm, $\Sigma_t = 1.0\ \text{cm}^{-1}$, $\Sigma_s = 0.7\ \text{cm}^{-1}$, $\Sigma_a = 0.3\ \text{cm}^{-1}$, $\Sigma_f = 0.15\ \text{cm}^{-1}$, $\nu = 2.6$, $\nu\Sigma_f = 0.39\ \text{cm}^{-1}$. Since the slab thickness is 200 mean free paths, the first four eigenvalue ratios were calculated accurately using one-group diffusion theory (Duderstadt, 1976), where

$$k_n = \frac{\nu\Sigma_f / \Sigma_a}{1 + \frac{D}{\Sigma_a}\left(\frac{n\pi}{\tilde{L}}\right)^2}, \quad n = 1, 2, \cdots. \tag{4.1.1}$$

k_{eff} was calculated to be 1.29964 by diffusion and 1.299698 ± 0.000064 by MC. Table 1 compares these benchmark values to CMPM with a 2σ confidence interval using the minimum mesh size for each eigenvalue. As was explained in Section 3.2, the minimum mesh size to compute k_i / k_0 is an $(i+1)$-bin mesh. Table 2 compares the benchmark values to CMPM results with a finer 10-bin mesh.

	Benchmark Diffusion Results	CMPM 2σ Interval Using Minimum Mesh	Benchmark Contained in 2σ?
k_1/k_0	0.999178	(0.997318, 0.999554)	Yes
k_2/k_0	0.997812	(0.995361, 0.998493)	Yes
k_3/k_0	0.995906	(0.992385, 0.996581)	Yes
k_4/k_0	0.993465	(0.990747, 0.995439)	Yes

Table 1: First Four Eigenvalue Ratios of Problem 1
Benchmark vs CMPM with i+1-bin Mesh for ki/k0 and 2σ std. dev.

	Benchmark Diffusion Results	CMPM 2σ Interval Using 10-bin Mesh	Benchmark Contained in 2σ?
k_1/k_0	0.999178	(0.997601, 0.999685)	Yes
k_2/k_0	0.997812	(0.995296, 0.998456)	Yes
k_3/k_0	0.995906	(0.993775, 0.997507)	Yes
k_4/k_0	0.993465	(0.990936, 0.995572)	Yes

Table 2: First Four Eigenvalue Ratios of Problem 1
Benchmark vs CMPM with 10-bin Mesh and 2σ std. dev.

In all cases of varying bin sizes, CMPM correctly estimated each eigenvalue ratio within two standard deviations. This problem was analyzed as a proof-of-principle. The minimum size mesh for each eigenvalue ratio was enough to provide accurate estimates, since the eigenmodes of this problem are simple. For problems with more complicated eigenmode structure, the minimum mesh size may not be sufficient to accurately compute eigenvalues higher order than DR. This will be illustrated in Problem 2.

A final point to note is that DR for this problem is extremely large (~0.999178), making the problem very difficult to analyze. This is because a high accuracy is needed to differentiate DR from unity and because the cycles are extremely correlated. As a rough estimate, the correlation between cycles decays as λ_1^n, where *n* is the number of active cycles. This implies that cycles separated by a distance of 5,000 are still correlated by roughly $0.999178^{5000} = 1.6\%$.

The second problem is a mono-energetic, multi-region 1-D slab with isotropic scattering and vacuum boundary conditions using 400 inactive cycles, 40,000 active cycles and 80,000 particles per cycle. The make-up of Problem 2 is illustrated in Figure 4. There are two fuel regions on either end of the slab with scattering and absorbing material between them. This type of problem would most likely be found in criticality safety work. The first four eigenvalue ratios of this problem were computed using the

Green's Function Method (GFM) (Kornreich, 2003) with a 1,800-bin mesh across the entire domain. k_{eff} was calculated to be 0.424314 by GFM and 0.424314 ± 0.000007 by MC. Table 3 shows CMPM results using the minimum mesh size and Table 4 shows the result of the CMPM method using a 10-bin mesh (5 bins per fuel region). These results are compared to the benchmark GFM using a 1,800-bin mesh. Due to the complicated nature of the eigenmodes for this problem, CMPM has also been applied using a 30-bin mesh (15 bins per fuel region) as shown in Table 5.

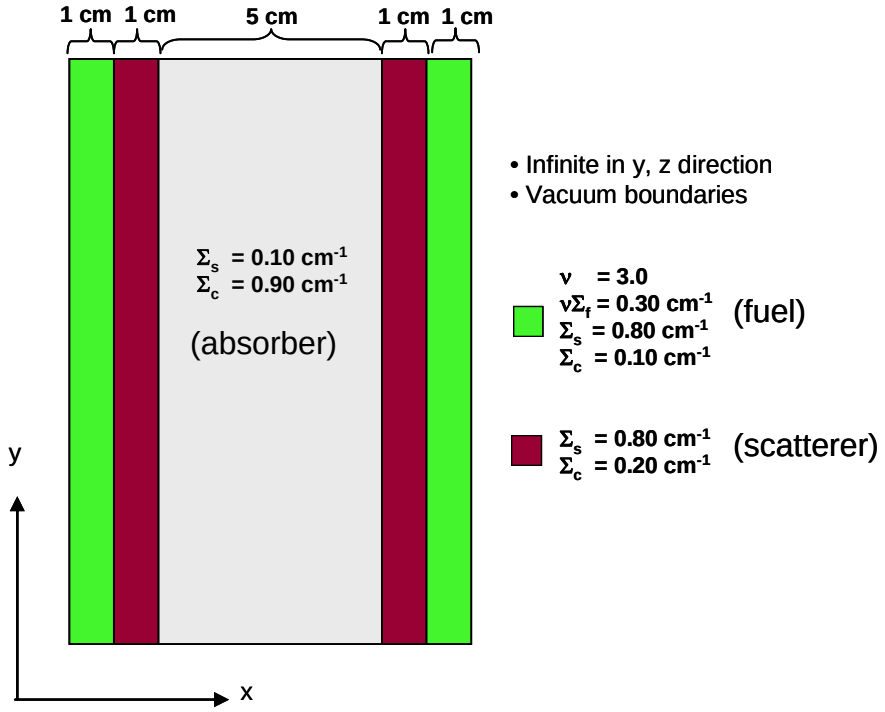

Figure 4: Problem 2 – 1D Heterogeneous Slab

	GFM Using 1,800-bin Mesh	CMPM 2σ Interval Using Minimum Mesh	Benchmark Contained in 2σ?
k_1/k_0	0.999565	(0.999094, 0.999768)	Yes
k_2/k_0	0.304653	(0.240241, 0.259606)	No
k_3/k_0	0.304635	(0.259391, 0.278653)	No
k_4/k_0	0.167738	(0.132929, 0.152724)	No

Table 3: First Four Eigenvalue Ratios of Problem 2
Benchmark vs CMPM with i+1-bin Mesh for ki/k0 and 2σ std. dev.

	GFM Using 1,800-bin Mesh	CMPM 2σ Interval Using 10-bin Mesh	Benchmark Contained in 2σ?
k_1/k_0	0.999565	(0.999060, 0.999750)	Yes
k_2/k_0	0.304653	(0.302578, 0.312710)	Yes
k_3/k_0	0.304635	(0.280032, 0.299176)	No
k_4/k_0	0.167738	(0.145242, 0.164998)	No

Table 4: First Four Eigenvalue Ratios of Problem 2
Benchmark vs CMPM with 10-bin Mesh and 2σ std. dev.

	GFM Using 1,800-bin Mesh	CMPM 2σ Interval Using 30-bin Mesh	Benchmark Contained in 2σ?
k_1/k_0	0.999565	(0.999405, 0.999750)	Yes
k_2/k_0	0.304653	(0.292868, 0.311932)	Yes
k_3/k_0	0.304635	(0.285621, 0.304730)	Yes
k_4/k_0	0.167738	(0.161231, 0.180936)	Yes

Table 5: First Four Eigenvalue Ratios of Problem 2
Benchmark vs CMPM with 30-bin Mesh and 2σ std. dev.

The first two eigenvalue ratios estimated by CMPM using a 10-bin mesh (Table 4) fall within range of the benchmark GFM value. k_3/k_0 is within 4σ and k_4/k_0 is within 3σ. This is still relatively close considering the magnitude of the confidence interval. If a 30-bin mesh is used instead (Table 5), all results fall within the 2σ interval range. The estimates improve when using a finer mesh because it is able to capture the fluctuations of the higher-order eigenvalue ratios. Applying a mesh that has greater than 30 bins, however, does not further increase performance. Also, note in Table 3 – Table 5, k_1/k_0 is accurately computed using only the minimum 2-bin mesh. This is because the first non-fundamental mode eigenfunction is known to only change sign once over the domain and the application of a 2-bin mesh will always prevent the complete cancellation of the mode. It is recommended that the coarsest mesh be used that prevents significant

cancellation of the eigenmode to increase computational performance and reduce memory usage.

Problem 3 is a monoenergetic 2-D checkerboard with isotropic scattering and vacuum boundary conditions illustrated in Figure 5. This problem was run using 400 inactive cycles, 40,000 active cycles and 80,000 particles per cycle. There are two types of fuel placed alternately in a checkerboard manner making the problem symmetric along the diagonals. The ratio of the first two eigenvalues (k_1/k_0) was estimated by the analysis of the spectral radius of outer iterations in discontinuous finite element discrete ordinates methods (Wareing, 2001) and are considered the benchmark result for DR. k_{eff} was calculated to be 1.05450 (DR = 0.9581) by discrete ordinates and 1.054504 ± 0.000010 by MC. The higher order eigenvalues were not available by the spectral radius analysis and so were obtained by the Fission Matrix Method (FMM) using the same discontinuous finite element discrete ordinates method with a 2304-bin mesh (48 bins in each coordinate direction) instead. Table 6 compares the DR benchmark result described above versus CMPM using a 4-bin mesh (two bins in each coordinate direction). Table 7 and Table 8 show the first four eigenvalue ratios computed using CMPM with a 9-bin mesh and 36-bin mesh, respectively. These results are compared to the FMM results described above using a 2,304-bin mesh.

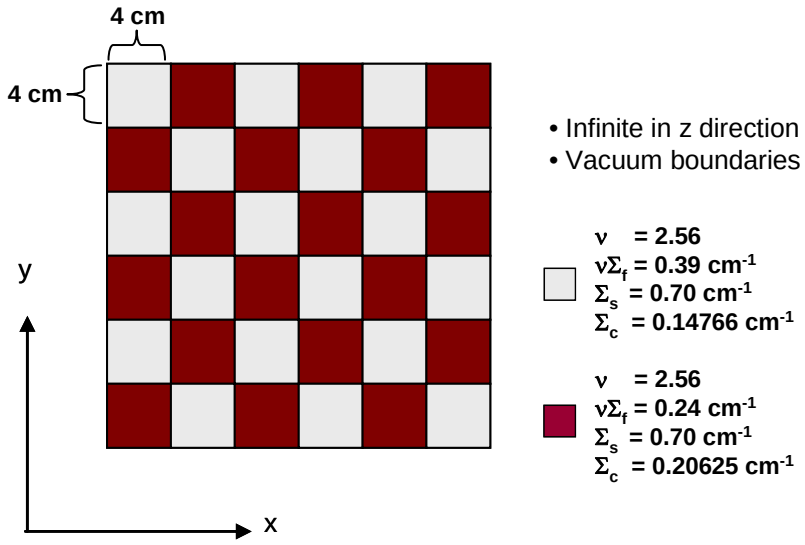

Figure 5: Problem 3 – 2D Checkerboard

	Benchmark by Discrete Ordinates	CMPM 2σ Interval Using 4-bin Mesh	Benchmark Contained in 2σ?
k_1/k_0	0.9581	(0.953156, 0.959017)	Yes

Table 6: DR of Problem 3
Benchmark vs CMPM with Minimum 4-bin Mesh and 2σ std. dev.

	FMM Using 2,304-bin Mesh	CMPM 2σ Interval Using 9-bin Mesh	FMM Result Contained in 2σ?
k_1/k_0	0.95740	(0.953650, 0.959480)	Yes
k_2/k_0	0.95710	(0.953650, 0.959480)	Yes
k_3/k_0	0.92031	(0.908889, 0.917050)	No
k_4/k_0	0.89708	(0.887557, 0.896594)	No

Table 7: First Four Eigenvalue Ratios of Problem 3
Benchmark vs CMPM with 9-bin Mesh and 2σ std. dev.

	FMM Using 2,304-bin Mesh	CMPM 2σ Interval Using 36-bin Mesh	FMM Result Contained in 2σ?
k_1/k_0	0.95740	(0.954088, 0.959891)	Yes
k_2/k_0	0.95710	(0.953242, 0.959098)	Yes
k_3/k_0	0.92031	(0.917194, 0.924981)	Yes
k_4/k_0	0.89708	(0.894094, 0.902874)	Yes

Table 8: First Four Eigenvalue Ratios of Problem 3
Benchmark vs CMPM with 36-bin Mesh and 2σ std. dev.

This problem is interesting in several regards. First, similar to the previous problem, the first two eigenvalue ratios were accurately contained in the 2σ interval when using a very coarse mesh (9 bins in this case). The third and fourth eigenvalue ratios were close (within 4σ) but not contained. Using a slightly finer 36-bin mesh, CMPM was able to accurately compute all of the first four eigenvalue ratios within the 2σ interval. Second, since the problem is symmetric along the diagonal, it is affected by multiplicity where the first and second non-fundamental eigenvalues (and likewise, the eigenvalue ratios) are theoretically equal. Interestingly, using a 9-bin mesh, k_1/k_0 and k_2/k_0 are exactly the same. This is because the two largest eigenvalues of the NP matrix were complex conjugates of each other. For this particular calculation, the magnitudes of the imaginary parts were very small compared to the real parts of the result, and so the imaginary parts were simply ignored. Later in this chapter the appearance of complex results will be discussed and ways to account for the imaginary parts will be considered. At this point, however, it is enough to note that using only the real part of the eigenvector produced accurate results that contained the benchmark values.

The fourth problem is a mono-energetic 3-D homogeneous cube with isotropic scattering and vacuum boundary conditions using 200 inactive cycles, 40,000 active cycles and 80,000 particles per cycle. The geometric and material properties are as follows: Length 200 cm (each side), $\Sigma_t = 1.0\ \text{cm}^{-1}$, $\Sigma_s = 0.75\ \text{cm}^{-1}$, $\Sigma_a = 0.25\ \text{cm}^{-1}$, $\Sigma_f = 0.11\ \text{cm}^{-1}$, $\nu\Sigma_f = 0.275\ \text{cm}^{-1}$. Benchmarks for the first four eigenvalue ratios were obtained by the discontinuous finite element discrete ordinates method with Krylov subspace iterations (Warsa, 2000). k_{eff} was calculated to be 1.098912 ± 0.000009 by discrete ordinates and 1.098912 ± 0.000009 by MC. Table 9 compares CMPM with an 8-

bin mesh (2 bins in each coordinate direction). Table 10 compares the same, but with a finer 216-bin CMPM mesh (6 bins in each direction).

	Benchmark by Discrete Ordinates	CMPM 2σ Interval Using 8-bin Mesh	Benchmark Contained in 2σ?
k_1/k_0	0.99903	(0.998448, 0.999380)	Yes
k_2/k_0	0.99903	(0.998147, 0.999180)	Yes
k_3/k_0	0.99903	(0.997719, 0.998884)	No
k_4/k_0	0.99806	(0.996508, 0.997990)	No

Table 9: First Four Eigenvalue Ratios of Problem 4
Benchmark vs CMPM with Minimum 8-bin Mesh and 2σ std. dev.

	Benchmark by Discrete Ordinates	CMPM 2σ Interval Using 216-bin Mesh	Benchmark Contained in 2σ?
k_1/k_0	0.99903	(0.998028, 0.999100)	Yes
k_2/k_0	0.99903	(0.998028, 0.999100)	Yes
k_3/k_0	0.99903	(0.997215, 0.998520)	No
k_4/k_0	0.99806	(0.996868, 0.998263)	Yes

Table 10: First Four Eigenvalue Ratios of Problem 4
Benchmark vs CMPM with 216-bin Mesh and 2σ std. dev.

Due to the multiplicity of this problem, each eigenmode has three corresponding eigenvalues equal to each other. Using the 8-bin mesh and 216-bin mesh, the first two eigenvalue ratios were contained in the 2σ interval. While the third ratio was not contained, it was still within a 4σ interval in both cases.

As was seen in this section, CMPM performs well for 1-D, 2-D, and 3-D mono-energetic problem types, regardless of whether the problem contains multiplicity effects or not. The 2^n-bin mesh requirement for DR (k_1/k_0) calculations (where n is the number of dimensions of the problem) works as was predicted in the Mesh Analysis section. Increasing the number of bins beyond the necessary amount does not increase accuracy. While calculation of the higher-order eigenvalue ratios often requires a finer

bin structure than the minimum, the number of required bins is still much less than the counterpart Discrete Ordinates Method or Fission Matrix Method. A more rigorous analysis of the eigenmode cancellation effect due to bin discretization will be presented in Section 4.2.

The strength of the method has been shown in several examples that use very large numbers of particles per cycle and active cycles. Next, results are presented for using much smaller numbers of particles and cycles, more akin to what a user might encounter while running quick calculations. Many replicas are made for these smaller runs to check for bias in the eigenvalue ratios and its associated variance.

Bias Criteria

To ensure the precision of the method, the eigenvalue ratios were computed for multiple replicas. The multiple replicas were also made to gauge the reliability of the error calculation that was used.

Before showing the results of these analyses, the methodology to determine the presence of bias is presented. The expected value of the eigenvalue ratios are estimated using CMPM over multiple replicas. These replicas are all independent, using completely different random number seeds. The expected value of the eigenvalue ratio is calculated as the average of all ratios produced from the different replicas:

$$\bar{\lambda}_n = \frac{1}{R}\sum_{i=1}^{R} \lambda_n^{(i)} \tag{4.1.2}$$

where $\lambda_n^{(i)}$ corresponds to the eigenvalue ratio k_n/k_0 generated during the i^{th} replica and R is the total number of replicas. The variance of the mean is estimated as

$$\sigma_{\bar{\lambda}_n}^2 = \frac{\sigma_{\lambda_n}^2}{R} \tag{4.1.3}$$

where $\sigma_{\lambda_n}^2$ is the variance of each individual replica, estimated as

$$\sigma_{\lambda_n}^2 = \frac{1}{R-1}\sum_{i=1}^{R}\left(\lambda_n^{(i)} - \bar{\lambda}_n\right)^2 . \tag{4.1.4}$$

This analysis yields the first bias check for the actual eigenvalue ratio.

Bias Check #1 – Bias of the Eigenvalue Ratio

- If the estimated expected value $\bar{\lambda}_n \pm 3\sigma_{\bar{\lambda}_n}$ contains the benchmark value, then that particular analysis is strongly considered to be unbiased.

The bias of the error estimator is judged by the containment rate of the benchmark value. It is expected that 68.27% of all calculated ratios $\lambda_n^{(i)}$ will contain the benchmark value within a 1σ interval if the estimator $\left(1-\lambda_n^2\right)\big/N$ from Eq. (3.1.47) is used. If, after R replicas, ν replicas correctly contain the benchmark, then the likelihood of this is estimated as

$$\text{Prob}\left(\nu \text{ correct in } R \text{ replicas}\right) = \binom{R}{\nu} p^{\nu}\left(1-p\right)^{R-\nu} . \tag{4.1.5}$$

where $\left(R/\nu\right)$ is a binomial calculated as

$$\binom{R}{\nu} = \frac{R!}{\nu!\left(R-\nu\right)!} \tag{4.1.6}$$

and p is the probability of 1σ containment assuming no bias for the error estimator; $p = 0.6812$. In all of the following tests, 50 replicas are consistently made for each problem. Knowing this, the interval of ν having Rp at the center that will contain 95%

of the most likely occurances of a 1σ containment can be calculated. When $R = 50$, this interval is $27 < \nu < 41$, so the sum of the probability in Eq. (4.1.5) from $\nu = 28$ through $\nu = 40$ is 0.95 with $Rp = 34$ in the middle. Doing this yields the second bias test.

Bias Check #2 – Bias of the Error

- If the number of replicas that correctly contain the benchmark value lies within the range $27 < \nu < 41$ out of 50 replicas, then the analysis is considered strongly unbiased.

These are the two criterion used to test for bias of the estimated eigenvalue ratio and its associated error.

Bias Verification

The results in this section illustrate the bias effects due to too few active cycles. As was indicated in Section 2.2, the correlations between cycles decay roughly as the exponential of DR, or λ_1^m, where *m* is the number of active cycles. We impose that there either be a minimum of 500 active cycles or less than a 0.1% correlation between the first and last cycles to ensure unbiased results. If this is the case, the minimum number of active cycles necessary to obtain unbiased results is estimated as

$$\eta_{AC} = \max\left[500, \frac{\ln\left(10^{-3}\right)}{\ln\left(\lambda_1\right)}\right]. \tag{4.1.7}$$

As will be shown, this number is sufficient unless two eigenvalues are extremely close in magnitude ($k_{i+1}/k_i > 0.99$). In these cases, the rule works for the larger eigenvalue k_i, but not for the smaller (degenerate) eigenvalue k_{i+1}. The degenerate

eigenvalue is very difficult to determine, often requiring thousands more cycles. This applies even to DR. As such, no specific rule is provided as to the minimum number of active cycles to calculate an unbiased estimate of the smaller degenerate eigenvalue.

The results of Problem 3 are shown first. Problem 3 was run using 200 inactive cycles, 500 active cycles and 10,000 particles per cycle. All other problem parameters remained the same. The k_1/k_0 results were made using a 4-bin mesh (2 bins in each coordinate direction) and the k_2/k_0 and k_3/k_0 results were made using a 36-bin mesh (6 bins in each coordinate direction).

Figure 6 shows k_1/k_0 estimates with a 1σ interval. The average of the replicas was 0.95698 ± 0.001539 (1σ), which contains the benchmark value of 0.9581 within 3σ. 36 out of 50 replicas contained the benchmark value within a 1σ interval, which is within the interval $27 < \nu < 41$. This analysis does not appear biased.

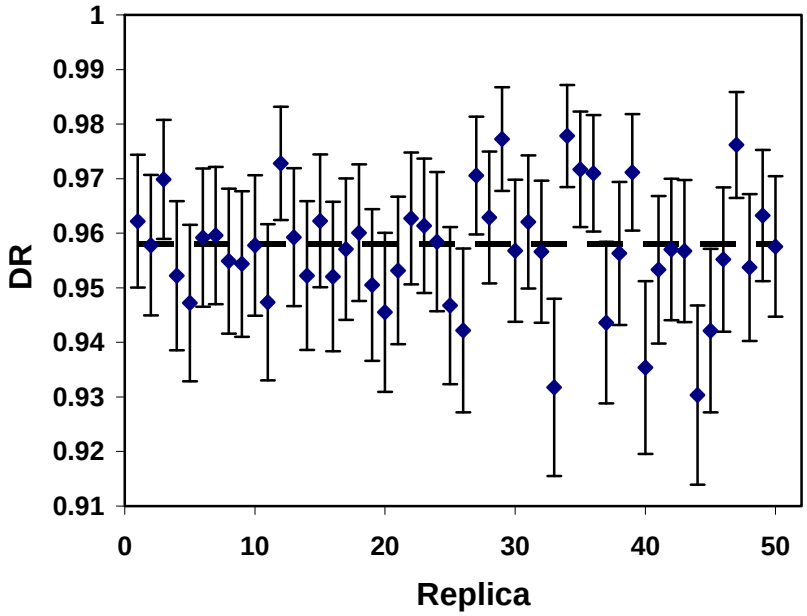

Figure 6: 50 k1/k0 Replicas of Problem 3 Using 500 Active Cycles Benchmark vs CMPM with Minimum 4-bin Mesh and 1σ std. dev.

Figure 7 and Figure 8 show the k_2/k_0 and k_3/k_0 results, respectively, for Problem 3. The k_2/k_0 average was 0.93096 ± 0.00222 (1σ) and 13 out of 50 replicas contained the benchmark value within a 1σ interval. This result does not contain the benchmark result of 0.95710 within a 3σ range and is not quite within the containment range; it appears to be biased. The k_3/k_0 average was 0.91155 ± 0.00187 (1σ) and 39 out of 50 replicas contained the benchmark value within a 1σ interval. This result contains the benchmark value of 0.92031 and is within the containment range; it is unbiased.

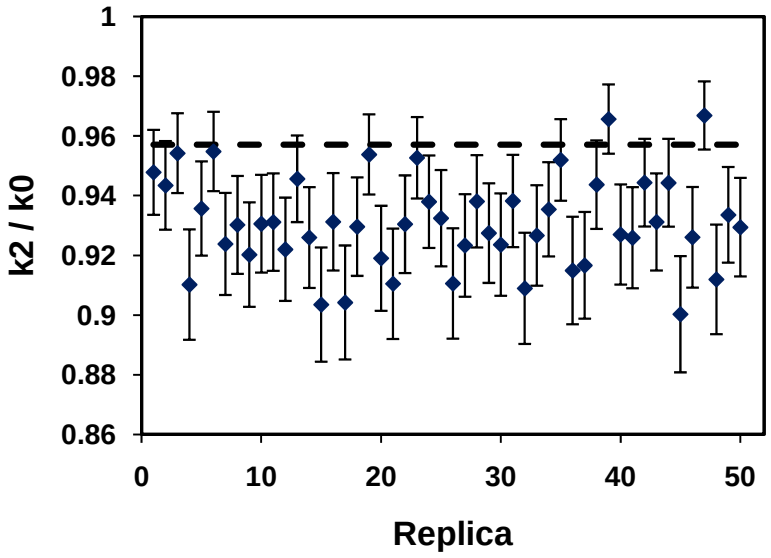

Figure 7: 50 k2/k0 Replicas of Problem 3 Using 5,000 Active Cycles Benchmark vs CMPM with 36-bin Mesh and 1σ std. dev.

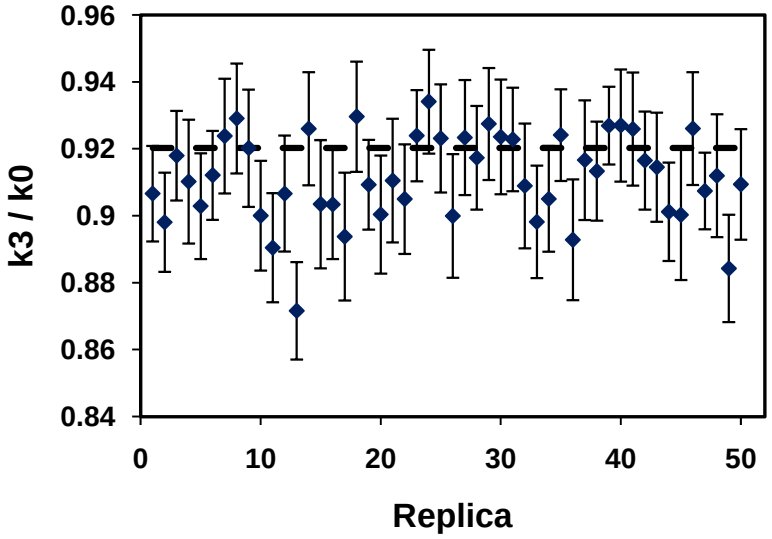

Figure 8: 50 k3/k0 Replicas of Problem 3 Using 5,000 Active Cycles Benchmark vs CMPM with 36-bin Mesh and 1σ std. dev.

Problem 2 was run twice, each with 50 replicas. The first run used 500 inactive cycles, 5,000 active cycles and 30,000 particles per cycle. The second run used 500 inactive cycles, 11,000 active cycles and 30,000 particles per cycle. This was done to illustrate the effect of using too few active cycles. All other problem parameters remained the same.

Figure 9 shows k_1/k_0 estimates for 50 replicas of Problem 2 using 5,000 active cycles with a 2-bin mesh and 1σ interval. Using 5,000 active cycles, the first and last cycles are estimated to still be correlated by $0.999566^{5000} = 11.4\%$. It was expected that these results would be highly biased since too few cycles were used. The average was 0.99839 ± 0.00014 (1σ) and 18 out of 50 replicas contained the benchmark value within a 1σ interval. As expected, neither of the bias criteria is met.

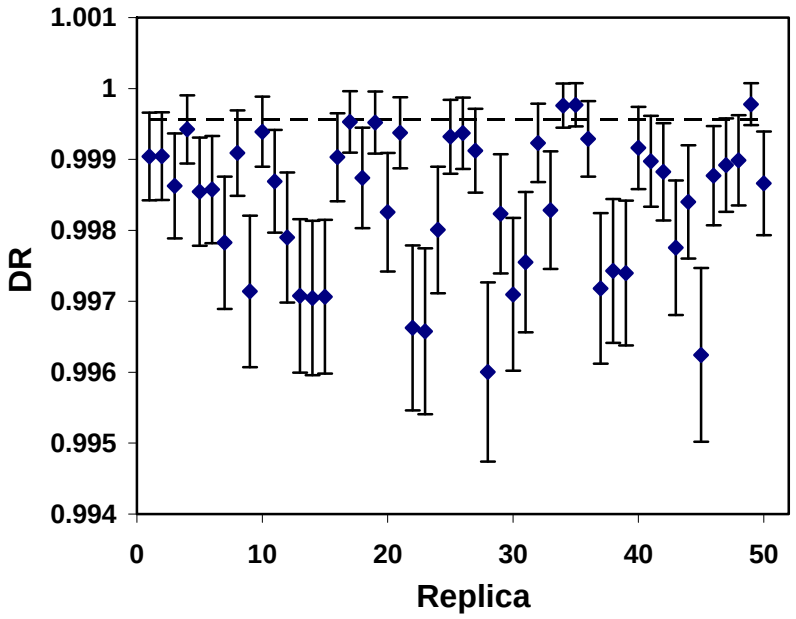

Figure 9: 50 k1/k0 Replicas of Problem 2 Using 5,000 Active Cycles Benchmark vs CMPM with Minimum 2-bin Mesh and 1σ std. dev.

Figure 10 shows DR estimates for Problem 2 using 11,000 active cycles and a 2-bin CMPM mesh. The average was 0.99907 ± 0.00007 (1σ) and 25 out of 50 replicas contained the benchmark value within a 1σ interval. These results are still slightly biased, though markedly improved.

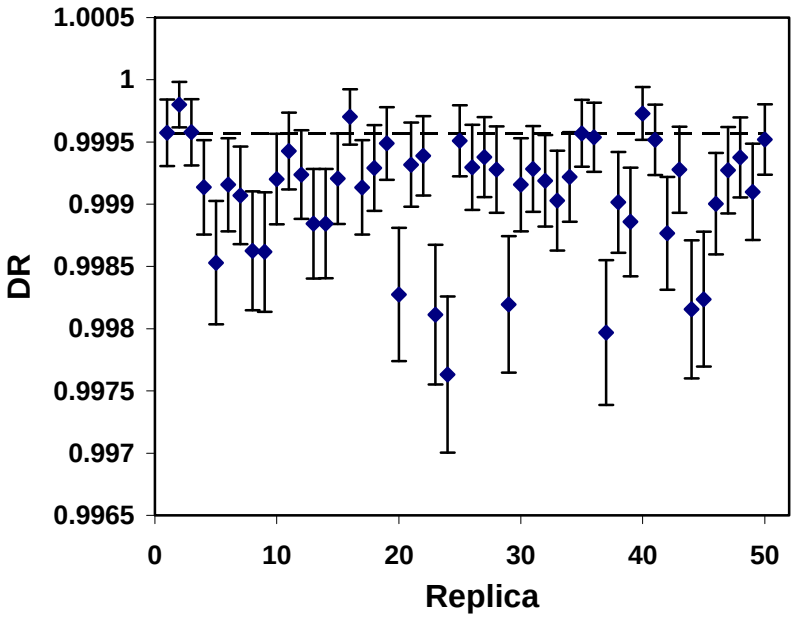

Figure 10: 50 k1/k0 Replicas of Problem 2 Using 11,000 Active Cycles Benchmark vs CMPM with Minimum 2-bin Mesh and 1σ std. dev.

Figure 11 and Figure 12 show the k_2/k_0 and k_3/k_0 results, respectively, for Problem 2 using 11,000 active cycles and a 25-bin CMPM mesh. The k_2/k_0 average was 0.307379 ± 0.00130 (1σ) and 35 out of 50 replicas contained the benchmark value within a 1σ interval. This result contains the benchmark result of 0.304653 with a 3σ range and is well within the containment range; it appears to be unbiased. The k_3/k_0 average was 0.290177 ± 0.00132 (1σ) and 13 out of 50 replicas contained the benchmark value within a 1σ interval. This result does not contain the benchmark value of 0.304635 and is not within the containment range; it is concluded to be biased.

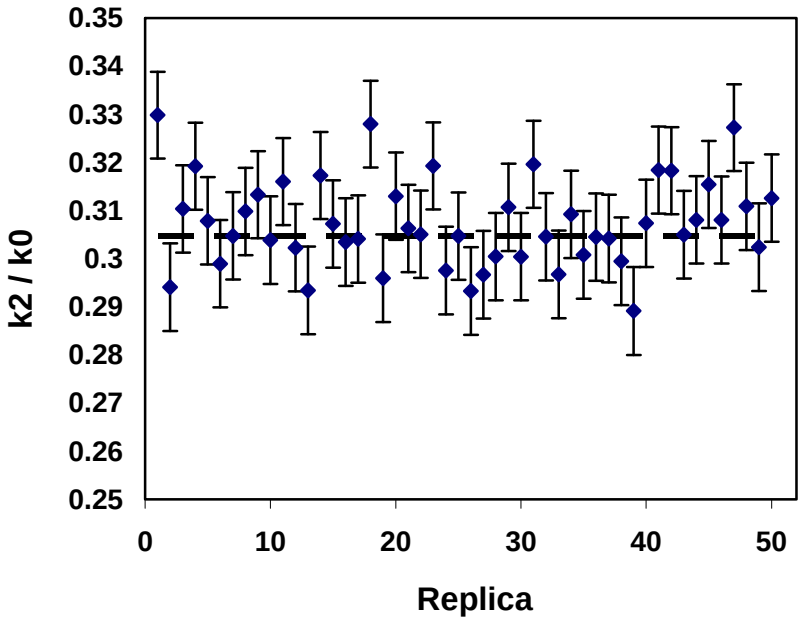

Figure 11: 50 k2/k0 Replicas of Problem 2 Using 11,000 Active Cycles Benchmark vs CMPM with 25-bin Mesh and 1σ std. dev.

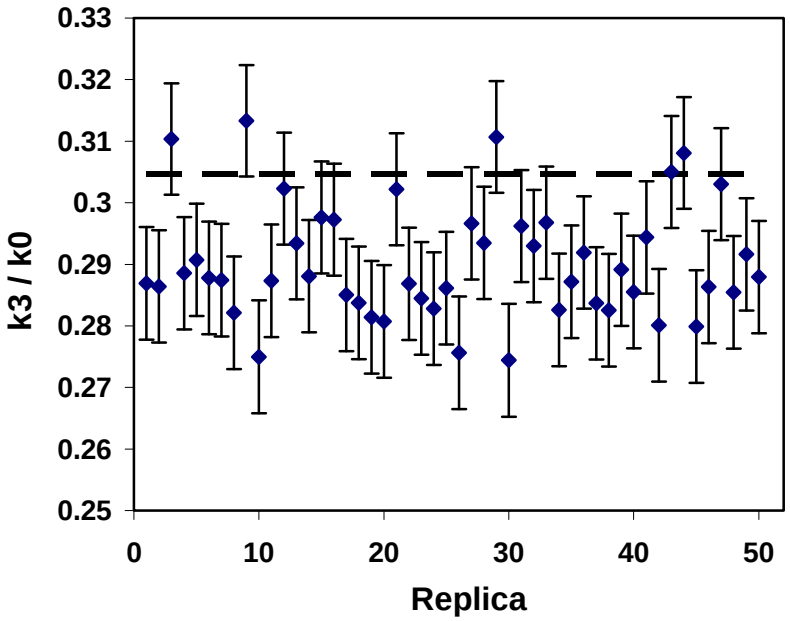

Figure 12: 50 k3/k0 Replicas of Problem 2 Using 11,000 Active Cycles Benchmark vs CMPM with 25-bin Mesh and 1σ std. dev.

Out of all of the results presented above, certain results appear biased while others do not. As was mentioned earlier, the biased results only appear in the smaller of the degenerate eigenvalues (i.e. k_{i+1} when $k_{i+1}/k_i > 0.99$), despite that thousands of active cycles were used. This is the case in Figure 7, Figure 10, and Figure 12. These results are representative of others encountered. In these cases, however, the largest eigenvalue k_i is accurately calculated using the number of active cycles required by Eq. (4.1.7).

Eventually, the bias does disappear given enough active cycles. One particular replica of Problem 2 was tested by increasing the number of cycles further. Replica 45 from the 50 replicas shown in Figure 9 and Figure 10 was chosen since it was biased using both 5,000 and 11,000 active cycles. The convergence of k_1/k_0 versus the number of active cycles is shown in Figure 13.

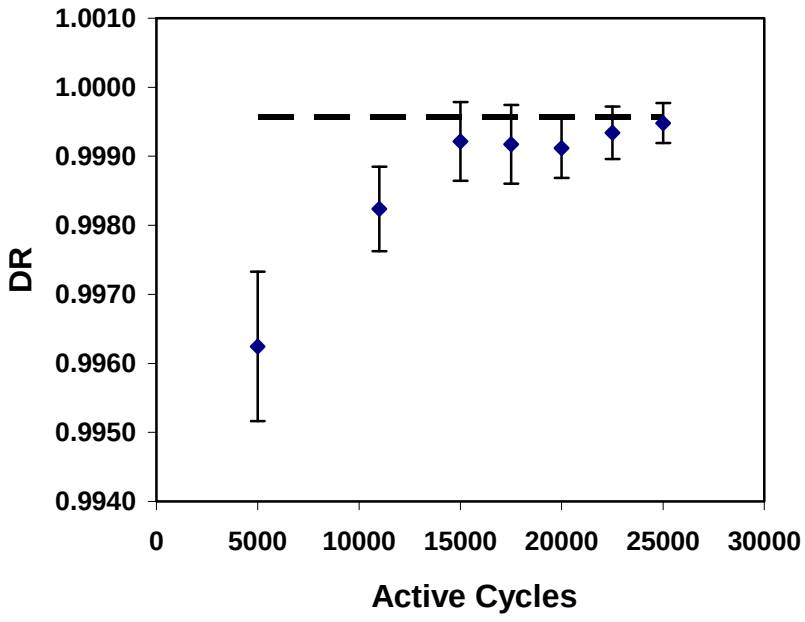

Figure 13: DR Convergence vs # of Active Cycles Replica #45 of Problem 2 Benchmark vs CMPM with Minimum 2-bin Mesh and 1σ std. dev.

As illustrated above, the bias decreases as the number of active cycles increases. This result is also representative of others that were encountered. Based on Figure 6 and Figure 11, the recommended number of active cycles $\eta_{AC} = \max\left[500, \ln\left(10^{-3}\right)/\ln\left(\lambda_1\right)\right]$ in Eq. (4.1.7) appears to be sufficient for eigenvalues that are not degenerate and for the larger of the two degenerate eigenvalues k_i (where $k_{i+1}/k_i > 0.99$). In addition, the criterion appeared to be sufficient even for the smaller near-degenerate eigenvalue k_1 from Problem 2 (as shown in Figure 13). However, it was not sufficient for smaller degenerate eigenvalue k_2 in Problem 3 (as shown in Figure 7). In the latter case, 500 active cycles were sufficient, though biased results still appeared when using 5,000 active cycles. Thus, the criteria of Eq. (4.1.7) cannot be said to always apply in cases of the smaller of two degenerate eigenvalues k_{i+1}. Significantly more active cycles are typically required, often on the orders of $O\left(10^3\right)$ – $O\left(10^4\right)$. Problems with degenerate eigenvalues are typically known a priori, since the multiplicity is often due to symmetry within the problem geometry. In such cases, it is recommended that a much larger number of active cycles be used, or that the larger repeated eigenvalue be used.

Section 4.2: Complex Solutions

Another consequence of the degenerate eigenvalues (besides a lasting bias that makes the eigenvalues difficult to calculate) is the appearance of complex solutions. In this section, an analysis is made of the complex eigenvalue solutions.

There are several immediate observations that can be made before beginning the analysis. First, it has been proven that the k-eigenvalue solutions of the mono-energetic transport equation are all real and discrete (Sahni, 1996). A similar statement cannot be made for continuous energy problems, though the author does not know of any real-world problems where complex eigensolutions have been encountered. Second, the NP matrix $\mathbf{A}_0$ is not symmetric (nor is it symmetric in the limit of active cycles, *m*), so it cannot be guaranteed that the eigenvalues of $\mathbf{A}_0$ are all real.

The questions that must be investigated are 1) under what conditions complex components arise, 2) how frequent complex components occur, 3) what the relative magnitude of the imaginary part is with respect to the real part, and 4) how to properly account for the appearance of complex solutions. This analysis provides mainly numerical results in answer to these questions, since analytical derivations cannot be made for the spurious complex output that is due to large or irregular statistical fluctuation.

The conditions under which complex components arise are considered first. When only few active cycles are used $\left(\sim O\left(10^2\right)\right)$, consecutive eigenvalues sometimes appeared as complex conjugates even when their relative magnitude was only $k_{i+1}/k_i > 0.9$. When the number of active cycles became larger $\left(\sim O\left(10^3\right)\right)$ and the eigenvalues became more distinguishable, this did not occur. When the consecutive eigenvalues were much closer in magnitude $\left(k_{i+1}/k_i > 0.99\right)$ the frequency of complex components was high.

Table 11 shows the frequency of the k_2/k_0 and k_3/k_0 eigenvalues appearing as complex conjugates of each other in the 50 replicas of Problem 2 using a 25-bin mesh. Table 12 shows the frequency of the k_1/k_0 and k_2/k_0 eigenvalues appearing as complex conjugates of each other in the 50 replicas of Problem 3 using a 4-bin mesh. For Problem 3, the k_1 and k_2 eigenvalues (and likewise the k_1/k_0 and k_2/k_0 eigenvalues) are theoretically equal due to the symmetry in the problem.

As a quick aside, note that an odd number of source tally bins (25 in this case) were applied across the fissionable regions for the first case in Table 11, meaning that one bin covered part of the left and right regions. This is not a concern, however, because as long as there is only minimal cancellation of the associated eigenmode, any bin scheme can be applied. This will be demonstrated in the next section.

Active Cycles	Frequency of Complex
5000	24%
8000	14%
11000	20%

Table 11: Frequency of Complex k2/k0 and k3/k0 Eigenvalues in Problem 2

Active Cycles	Frequency of Complex
300	32%
500	24%
5000	18%

Table 12: Frequency of Complex k1/k0 and k2/k0 Eigenvalues in Problem 3

Though these results suggests that the frequency of complex components may decrease as the number of active cycles is increased, it is still quite variable and there is a relatively high rate of occurrence even with thousands of active cycles. Simply running more

cycles does not seem to be an optimal way to remove the influence of the complex components.

The magnitude of the imaginary part relative to the real part is also important to consider. Specifically, we wish to quantify an upper bound of the imaginary part and study whether or not the magnitude changes based on the number of active cycles. It was expected that the largest imaginary parts would occur in problems with the fewest active cycles. Problem 2 and Problem 3 were used again, and this assumption was confirmed.

Active Cycles	Average Imaginary
5000	0.01058
8000	0.00680
11000	0.00549

Table 13: Average Magnitude of Imaginary k2/k0 Component of A_0 in Problem 2 over 50 replicas

Active Cycles	Average Imaginary
300	0.01883
500	0.01114
2000	0.00452
5000	0.00230

Table 14: Average Magnitude of Imaginary k1/k0 Component of A_0 in Problem 3 over 50 replicas

The average magnitudes of the imaginary components that were measured in the tables above were plotted in a log-log plot in Figure 14 below. These magnitudes were contrasted against N^{-1} and $N^{-1/2}$ to illustrate how the imaginary component decreases based on the number of active cycles. As can be seen, the magnitude is bounded and appears to decrease no slower than $N^{-1/2}$.

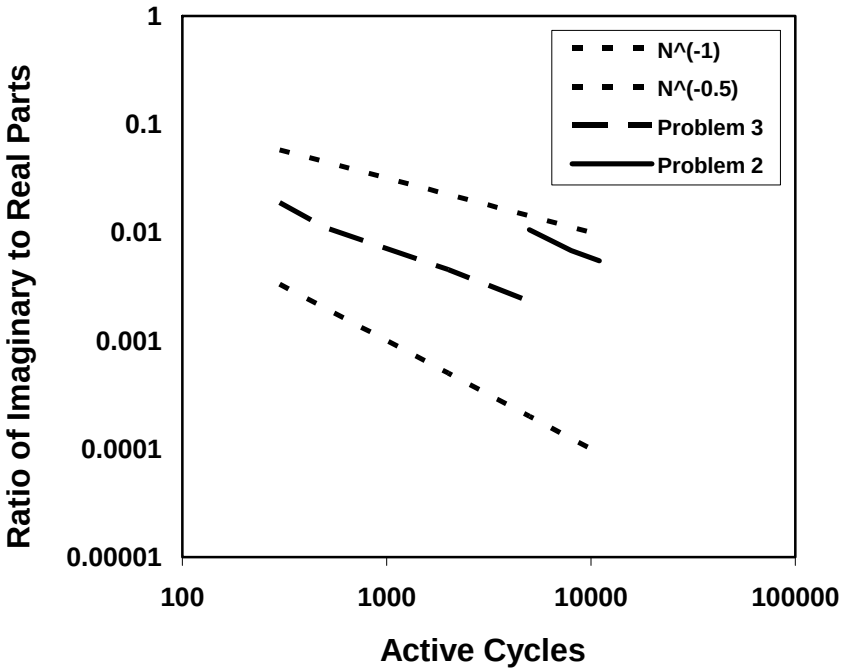

Figure 14: Ratio of Imaginary to Real Parts of k2/k0 and k1/k0 Eigenvalue of A_0 in Problem 2 and Problem 3, respectively

Quantifying the magnitude of the imaginary parts will allow us to select appropriate methods to account for the appearance of complex eigenvalues. Two such ideas are presented. The first method is to use the real part of the eigenvector as the projection vector and simply ignore the imaginary part. Since $\mathbf{A}_0$ is a real matrix, the eigenvalue problem described in Eq. (3.1.13) is rewritten as

$$\mathbf{A}_0 \vec{p} = \lambda \vec{p} \tag{4.1.8}$$

$$\mathbf{A}_0 \vec{p}^{\,*} = \lambda^* \vec{p}^{\,*} \tag{4.1.9}$$

where the conjugate quantities are defined as

$$\vec{p} = \vec{p}_R + i\vec{p}_I \tag{4.1.10}$$

$$\vec{p}^{\,*} = \vec{p}_R - i\vec{p}_I \tag{4.1.11}$$

$$\lambda = \lambda_R + i\lambda_I \tag{4.1.12}$$

$$\lambda^* = \lambda_R - i\lambda_I \,. \tag{4.1.13}$$

R and *I* signify the real and imaginary parts, respectively. Taking the sum of Eqs. (4.1.8) and (4.1.9) yields

$$\mathbf{A}_0\left(\vec{p} + \vec{p}^*\right) = \lambda\vec{p} + \lambda^*\vec{p}^* \,. \tag{4.1.14}$$

The RHS and LHS of the equation can be manipulated individually as

$$\text{LHS: } \vec{p} + \vec{p}^* = \left(\vec{p}_R + i\vec{p}_I\right) + \left(\vec{p}_R - i\vec{p}_I\right) = 2\vec{p}_R \tag{4.1.15}$$

$$\begin{aligned}\text{RHS: } \lambda\vec{p} + \lambda^*\vec{p}^* &= \left(\lambda_R + i\lambda_I\right)\left(\vec{p}_R + i\vec{p}_I\right) + \left(\lambda_R - i\lambda_I\right)\left(\vec{p}_R - i\vec{p}_I\right) \\ &= 2\lambda_R\vec{p}_R - 2\lambda_I\vec{p}_I\end{aligned} \tag{4.1.16}$$

Substituting these into Eq. (4.1.14), we obtain

$$\mathbf{A}_0 2\vec{p}_R = 2\lambda_R\vec{p}_R - 2\lambda_I\vec{p}_I \,. \tag{4.1.17}$$

Assuming that the magnitude of the real eigenvalue component is much larger than the magnitude of the imaginary part, i.e., $\left|\lambda_I\right| << \left|\lambda_R\right|$, then the RHS of Eq. (4.1.17) can be approximated as

$$\mathbf{A}_0 2\vec{p}_R = 2\lambda_R\vec{p}_R - 2\lambda_I\vec{p}_I \approx 2\lambda_R\vec{p}_R \,. \tag{4.1.18}$$

Thus, the eigenvalue problem remains the same even if only the real part of the eigenvector is used. This proof is based on the assumption that the magnitude of the imaginary part of the eigenvalue is much less than the real part. Since the magnitude was found to be bounded by the number of active cycles in Figure 14, this assumption appears to be valid. This was the method used in this research. All results presented use only the real part of the eigenvector as the projection vector.

As an interesting side note, if the eigenvectors are subtracted instead of added in Eq. (4.1.14) and a similar derivation is followed, we can show that

$$\mathbf{A}_0 2i\vec{p}_I = 2i\lambda_R \vec{p}_I + 2i\lambda_I \vec{p}_R \approx 2i\lambda_R \vec{p}_I . \tag{4.1.19}$$

This indicates that the imaginary part of the eigenvector can be used as the projection vector (ignoring the real part) and real eigenvalues can still be obtained. Note that $|\lambda_I| << |\lambda_R|$ does not necessarily imply that $\|\vec{p}_I\| << \|\vec{p}_R\|$.

To show that using the imaginary part of the eigenvector can be used as the projection vector, a numerical result is presented. The third replica of Problem 2 shown in Figure 11 and Figure 12 had complex conjugate eigenvalues for k_2/k_0 and k_3/k_0 when using a 25-bin mesh. The ratio k_2/k_0 was re-calculated using only the imaginary part $\vec{p}_I$ of the eigenvector (instead of solely the real part) as the projection vector. The results are shown below.

	GFM Using 1,800-bin Mesh	CMPM 2σ CI Using Real Eigenvector	CMPM 2σ CI Using Imaginary Eigenvector
k_2/k_0	0.304653	(0.293625, 0.329863)	(0.288569, 0.324869)

Table 15: k_2/k_0 of Problem 2 Using Real & Imaginary Eigenvectors CMPM with 25-bin Mesh and 2σ std. dev.

The second method to account for the imaginary components is to perform the autoregressive fitting using a complex time series vector. This would be a desirable method if the magnitude of the imaginary component was not negligible or if it were believed that the eigenvalue was, in fact, complex in nature. Allowing for complex valued processes is not difficult, though it does require some changes to the definitions of the autocovariance functions.

Suppose that a projection vector $\vec{p} = \vec{p}_R + i\vec{p}_I$ is applied to the source fluctuation as done in Section 3.1, but creating a complex valued time series instead where

$y^{(m)} = y_R^{(m)} + iy_I^{(m)}$. According to Priestly (1981), in complex cases the autocovariance function of a zero-mean stationary process $y^{(m)}$ is defined as

$$\gamma_i = E\left[y^{(m)*} y^{(m+i)} \right] \tag{4.1.20}$$

where $y^{(m)*}$ is the complex conjugate such that $y^{(m)*} = y_R^{(m)} - iy_I^{(m)}$. Following the form of Eq. 3.1.35, the eigenvalue ratio is defined as

$$\lambda_i = \frac{E\left[y^{(m+i)} y^{(m)*} \right]}{E\left[y^{(m)} y^{(m)*} \right]}. \tag{4.1.21}$$

In general, $\gamma_i,\ i \geq 1$ always remains complex if $y^{(m)}$ is complex, but

$$\gamma_0 = E\left[y^{(m)} y^{(m)*} \right] = E\left[\left| y^{(m)} \right|^2 \right] \tag{4.1.22}$$

is always real valued.

Eq. (4.1.21) allows for complex time series to be considered in cases where the imaginary part is not negligible or if the problem is believed to contain complex solutions. Most beneficial is that the process follows the simple procedure described in Chapter 3, requiring only a simple AR(1) fitting order. Numerical results are not presented since the author does not know of any real-world problems that have complex eigensolutions and did not encounter problems where $\left|\lambda_I\right|$ was not negligible compared to $\left|\lambda_R\right|$; only these theoretical arguments are provided.

Section 4.3: Eigenmode Cancellation Effect

A significant result of the Binary Half-Domain Fitting Method (Ueki, 2004) was that the fluctuation of the binned source contained uncompromised information of the

eigenvalue ratio k_1/k_0 if the complete cancellation of the corresponding eigenmode did not occur. Thus, performing time series analysis on the source fluctuation from only half of the domain yielded accurate DR results when applying an ARMA(2,1) fitting. While this implies that the eigenvalue ratios can be determined using only part of the source fluctuation, it does not guarantee a simple fitting order. In this section, a perturbation analysis is made to illustrate the effect of irregular mesh schemes on the accuracy of the estimated eigenvalue, with emphasis on keeping a simple AR(1) fitting order in CMPM. This will be important when applying CMPM to problems with complicated geometries, though the concept can be demonstrated using only one-dimensional problems.

Two problems are considered: Problem 2 (shown in Figure 4) and Problem 5. Problem 5 has nearly the same material and geometry as Problem 2 except for one difference: the right-most fuel region is 1.01 cm thick instead of 1 cm. These are the only differences between the two problems. Despite only a small variation, the flux shapes are considerably different; at certain points within the slab, they are orders of magnitude different. Figure 15 and Figure 16 below show the fundamental and first non-fundamental eigenmode of the flux for Problem 2 and Problem 5.

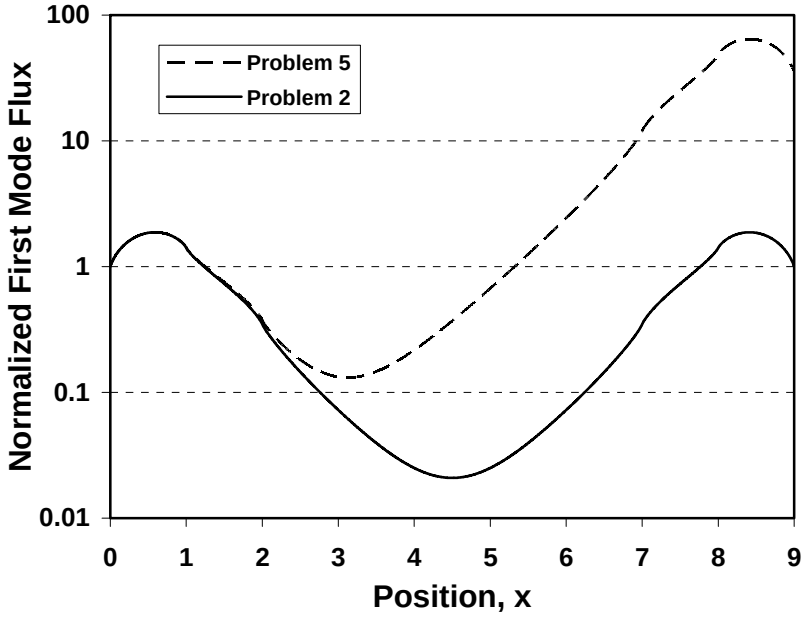

Figure 15: Fundamental Mode Flux Profile Comparison of Problem 2 and Problem 5

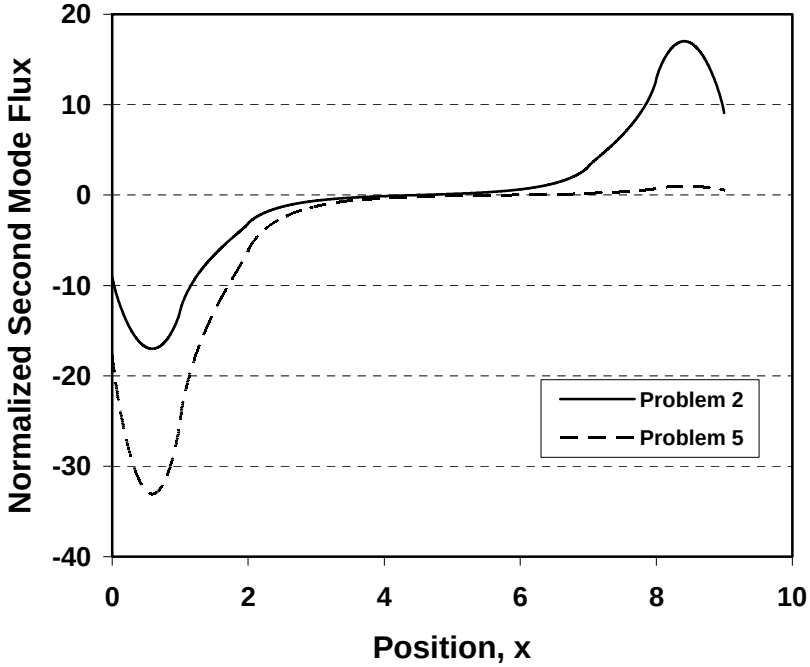

Figure 16: First Non-fundamental Mode Flux Profile Comparison of Problem 2 and Problem 5

The first four eigenvalue ratios of Problem 5 were computed using the Green's Function method (GFM) (Kornreich, 2003) with a 1,800-bin mesh across the entire domain. k_{eff} was calculated to be 0.427425 by GFM and 0.4274242 ± 0.000006 by MC.

	GFM Using 1,800-bin Mesh
k_1/k_0	0.992504
k_2/k_0	0.305628
k_3/k_0	0.302427
k_4/k_0	0.168273

Table 16: First Four Eigenvalue Ratios of Problem 5
Benchmark GFM with 1800-bin mesh

These problems are extremely difficult to analyze using traditional deterministic methods because of these complicated flux shapes. The left and right peaks of Problem 5 differ by over an order of magnitude. To obtain the benchmark results presented in Table 3 and Table 16, the problems were analyzed using an 1800-bin mesh over the domain. Using MC techniques and CMPM, however, the eigenvalues can be solved for using much fewer bins. This is because CMPM analyzes the fluctuation of the desired eigenmode only and removes all other eigenmodes. To produce accurate results using only the simplest AR(1) fitting, though, the applied mesh must minimize the cancellation of the desired mode. For instance, Figure 17 and Figure 18 show the eigenvector of matrix $\mathbf{A}_0$ corresponding to the eigenvalue ratio k_1/k_0 in Problem 2 and Problem 5, respectively.

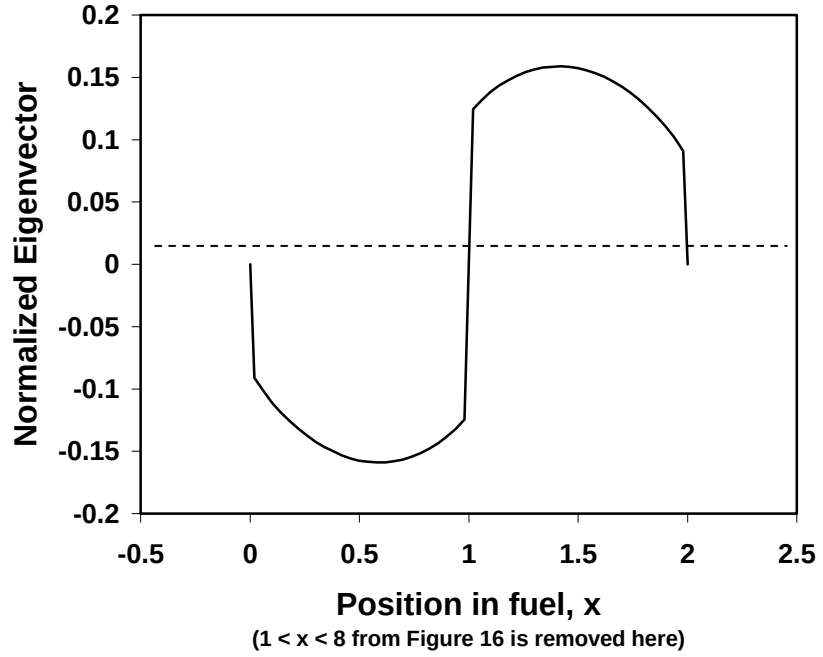

Figure 17: Normalized k1/k0 Eigenvector of A_0 of Problem 2

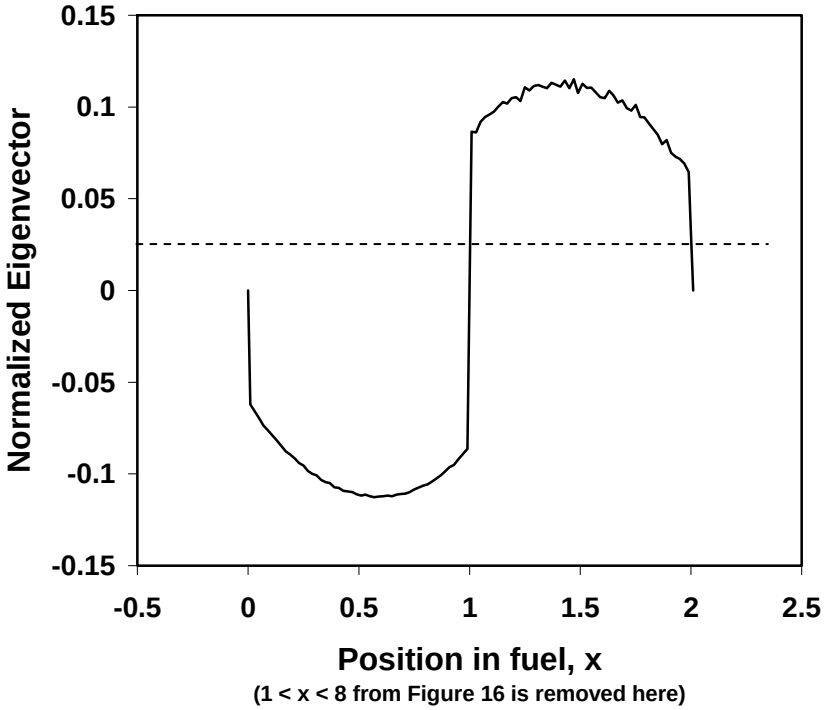

Figure 18: Normalized k1/k0 Eigenvector of A_0 of Problem 5

As can be seen, even though the flux shapes are drastically different between Problem 2 and Problem 5, the eigenvectors of $\mathbf{A}_0$ corresponding to k_1/k_0 are very similar. In addition, the first non-fundamental mode eigenfunction of the flux changes sign in the middle of the problem domain (shown in Figure 15 and Figure 16), which further supports that no cancellation will occur if the standard 2-bin mesh is applied. This is why applying a 2-bin mesh (one bin over each fuel region), produces accurate DR results. As long as there is minimal cancellation of the eigenmode over each bin, accurate eigenvalue results can be obtained.

To further illustrate this, DR is calculated using an irregular mesh for Problem 2. Five fission source tally bins are used. The bin sizes covering the fuel regions from the left-most boundary to the right-most are as follows: 1 cm, 0.4 cm, 0.3 cm, 0.2 cm, 0.1 cm. Note there is one bin for the left fuel region and four bins for the right fuel region. The eigenmode corresponding to k_1/k_0 changes sign between the two fuel regions (i.e. at 1 cm), so this mesh prevents any cancellation from occurring. Using 400 inactive cycles, 40,000 active cycles, 80,000 particles per cycle, DR was calculated as 0.999429 ± 0.000169. This result contains the benchmark GFM result within a 2-σ confidence interval. It is representative of all other bin arrangements where the cancellation of the eigenmode was prevented. As long as cancellation of the eigenmode is prevented, the bins can be any size, whatsoever.

A perturbation analysis of Problem 2 and Problem 5 was performed to quantitatively define the amount of cancellation that can occur before erroneous results are obtained. Since the shape of the eigenvector corresponding to the desired eigenvalue in Problem 2

is known (Figure 17), an irregular bin scheme is applied. A 3-bin mesh is applied to both problems as shown in Figure 19.

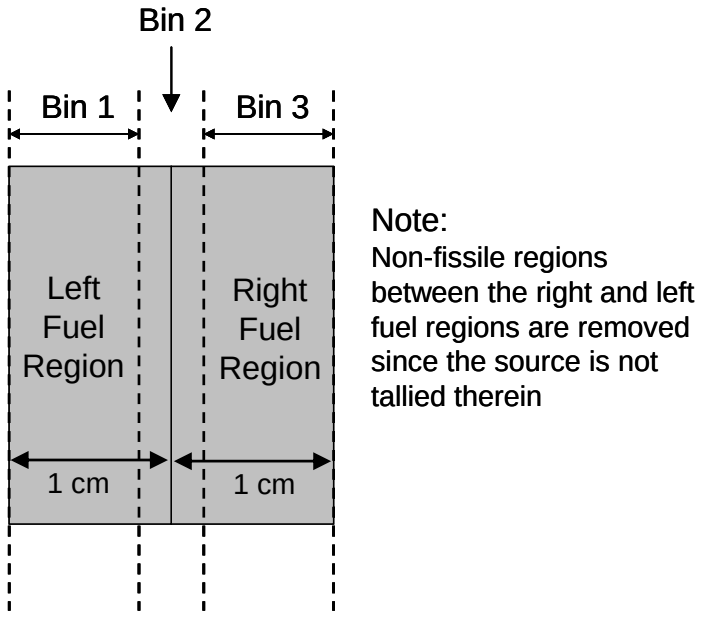

Figure 19: Mesh Scheme for Perturbation Analysis of Problem 2

Bin 1 and Bin 3 are the same size. Bin 2 is varied in size to gauge the amount of cancellation that occurs versus accuracy. In equation form, if Δ_1, Δ_2, Δ_3 are the widths of bins 1, 2, 3, respectively, then

$$\Delta_1 = \Delta_3$$

$$\Delta_1 = 1 - \frac{\Delta_2}{2}.$$

Figure 20 shows the results of this analysis.

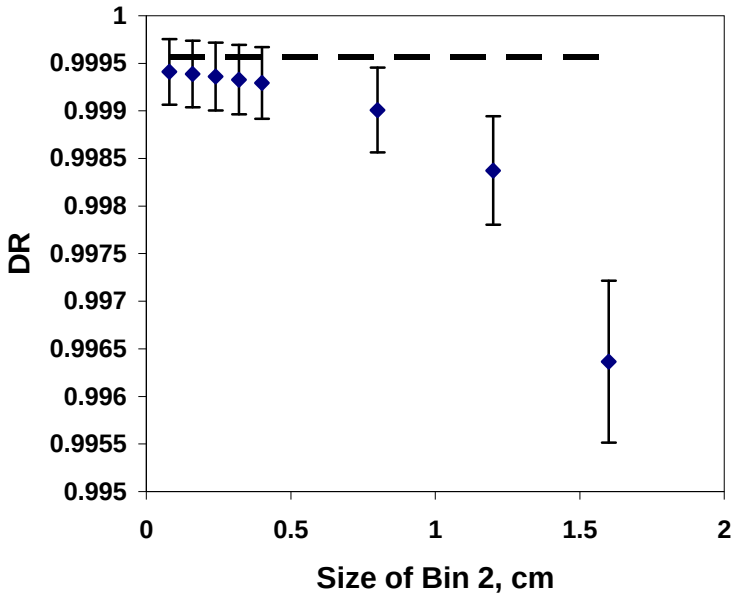

Figure 20: DR with 2σ std. dev. vs Increasing Eigenmode Cancellation Problem 2 Using 40,000 AC, 80,000 PC

From this result it appears that when more than 20% of the eigenvector canceled out over Bin 2 (corresponding to >0.4 cm for the size of Bin 2), the results became erroneous. At that point, the estimates were outside of a 2σ confidence interval. Especially with higher eigenmodes that have many fluctuations, a fine mesh scheme could be applied to prevent such a large cancellation of the mode. A stronger fitting order (such as ARMA(2,1)) could also be used to improve the estimate (Ueki, 2004), but the goal of CMPM is to keep the fitting method as simple as possible. CMPM relies on the availability of the full eigenmode for the simple AR(1) fitting order. As long as there is minimal cancellation of the mode, the method will produce accurate results, no matter what mesh scheme is applied. Formulating a broad mesh scheme criterion for higher eigenvalue calculation could be a topic for future research.

Section 4.4: Production Code Implementation

In this section, the practical implementation of CMPM into production codes is considered. A CMPM routine was added to the Monte Carlo code MCNP (X-5, 2003) and tested against the Fission Matrix Method. Specific concerns such as "on-the-fly" calculations are considered, as well as problems that have continuous-energy cross-sections.

Coding Considerations

The CMPM projection process has three main steps: 1) determination of an appropriate projection vector, 2) application of the projection vector to the source fluctuation, 3) time series analysis of the new projected series. The fourth step (solving the resulting polynomial/characteristic) is unnecessary when using CMPM since the desired eigenvalue ratio is simply the autocorrelation coefficient. Though it is a straightforward process, specific considerations when implementing this method into production codes such as MCNP have not yet been discussed. In particular, there is a strong desire to reduce memory usage, improve algorithm efficiency, and remove any reliance on commercial code packages to perform any parts of the calculation (such as matrix inversion, eigenvector determination, etc.).

Memory storage requirements are the most significant obstacle when implementing this method. Applied in a rudimentary way, the source fluctuation from every bin and every cycle must be stored during the run. After the run is complete, the eigenvectors of the noise propagation matrix can be computed and applied to the stored source fluctuations. Saving all of this data throughout the run is an enormous task; the number

of storage elements required for this implementation is $(p \text{ source bins}) \times (n \text{ active cycles})$. It is very common for there to be thousands of active cycles per run, so it is easy to see how this number can quickly become unmanageable. One of the main goals of the CMPM is to be less memory intensive than methods such as the FMM, so we derive an alternate expression of the eigenvalue ratio so that only the necessary terms are stored each cycle.

The terms in Eq. (3.1.44) can be written out fully as

$$\lambda_i = \frac{E\left[y^{(m+1)}y^{(m)}\right]}{E\left[y^{(m)}y^{(m)}\right]} = \frac{E\left[\left\langle \vec{d}^{(i)}, \vec{e}^{(m+1)} \right\rangle \left\langle \vec{d}^{(i)}, \vec{e}^{(m)} \right\rangle\right]}{E\left[\left\langle \vec{d}^{(i)}, \vec{e}^{(m)} \right\rangle \left\langle \vec{d}^{(i)}, \vec{e}^{(m)} \right\rangle\right]}, \tag{4.1.23}$$

where the projection vector $\vec{d}_i$ (which is the i^{th} eigenvector of $\mathbf{A}_0^*$) is written as $\vec{d}^{(i)}$ instead and its j$^{\text{th}}$ location is $d_j^{(i)}$. As proven in Appendix A, this can be written alternatively as the ratio of two Frobenius inner products as

$$\lambda_i = \frac{\left\langle \vec{d}^{(i)} \otimes \vec{d}^{(i)}, E\left[\vec{e}^{(m+1)} \otimes \vec{e}^{(m)}\right] \right\rangle}{\left\langle \vec{d}^{(i)} \otimes \vec{d}^{(i)}, E\left[\vec{e}^{(m)} \otimes \vec{e}^{(m)}\right] \right\rangle}. \tag{4.1.24}$$

This is a very important result. The only terms that must be stored each cycle are the cross and lag covariance matrices $\vec{e}^{(m+1)} \otimes \vec{e}^{(m)}$ and $\vec{e}^{(m)} \otimes \vec{e}^{(m)}$. This means that the number of storage elements is $2p^2$ since both matrices are size $p \times p$. As was explained in Section 3.2, smaller mesh sizes are preferred for the larger eigenvalue ratios (to reduce computer memory requirements), so the number of storage elements might typically range from eight (for the coarsest 2^1-bin mesh in one dimension) to two thousand (for a 10^3-bin mesh in three dimensions). This is a significant improvement to the original

arrangement in Eq. (4.1.23) or to the fission matrix method, both of which might require the square of thousands of storage elements.

This result is also important for the evaluation of the noise propagation matrix $\mathbf{A}_0$. Recalling Eqs. (3.1.9) – (3.1.11), $\mathbf{A}_0$ is evaluated as

$$\mathbf{A}_0 = \mathbf{L}_1 \mathbf{L}_0^{-1}$$

where

$$\mathbf{L}_0 = E\left[\vec{e}^{(m)} \otimes \vec{e}^{(m)}\right]$$

$$\mathbf{L}_1 = E\left[\vec{e}^{(m+1)} \otimes \vec{e}^{(m)}\right].$$

These are exactly the quantities that are stored for the final eigenvalue ratio calculation. Thus, no extra terms must be stored throughout the run to compute $\mathbf{A}_0$.

Another consideration when implementing this method into production codes is the evaluation of the source fluctuation. If the source is not stored for every bin and every cycle, there is no way to properly evaluate the source fluctuation since it is estimated by subtracting the ensemble average over all active cycles from the source. However, as stated before, production code developers wish to avoid storing all of this data, so we will also derive an alternate approach to use actual source values (instead of the fluctuations). First, the NP matrix calculation using the actual source will be derived. From this the equivalent projection vectors are calculated. Next, the eigenvalue calculation using the actual source will be derived, taking into account the result of Eq. (4.1.24).

We begin by rewriting Eq. (3.1.1)

$$\vec{e}^{(m+1)} = \mathbf{A}_0 \vec{e}^{(m)} + \vec{\varepsilon}^{(m+1)}. \tag{4.1.25}$$

If $\vec{S}_0$ is added to $\vec{e}^{(m)}$ in the RHS in the equation above, we obtain

$$\vec{e}^{(m+1)} = \mathbf{A}_0\left(\vec{S}_0 + \vec{e}^{(m)}\right) + \vec{\varepsilon}^{(m+1)} = \mathbf{A}_0\vec{S}^{(m)} + \vec{\varepsilon}^{(m+1)}, \tag{4.1.26}$$

since $\mathbf{A}_0\vec{S}_0 = 0$, according to Eq. (2.2.58). Now $\vec{S}_0$ is added to both sides of Eq. (4.1.26), yielding

$$\vec{S}^{(m+1)} = \mathbf{A}_0\vec{S}^{(m)} + \vec{\eta}^{(m+1)}, \tag{4.1.27}$$

where $\vec{\eta}^{(m+1)} = \vec{S}_0 + \vec{\varepsilon}^{(m+1)}$. Applying $\vec{S}^{(m)}$ to both sides as an outer product and taking the expectation results in

$$E\left[\vec{S}^{(m+1)} \otimes \vec{S}^{(m)}\right] = \mathbf{A}_0 E\left[\vec{S}^{(m)} \otimes \vec{S}^{(m)}\right] + E\left[\vec{\eta}^{(m+1)} \otimes \vec{S}^{(m)}\right] \tag{4.1.28}$$

$$E\left[\vec{S}^{(m+1)} \otimes \vec{S}^{(m)}\right] = \mathbf{A}_0 E\left[\vec{S}^{(m)} \otimes \vec{S}^{(m)}\right] + E\left[\left(\vec{\varepsilon}^{(m+1)} + \vec{S}_0\right) \otimes \left(\vec{e}^{(m)} + \vec{S}_0\right)\right] \tag{4.1.29}$$

$$E\left[\vec{S}^{(m+1)} \otimes \vec{S}^{(m)}\right] = \mathbf{A}_0 E\left[\vec{S}^{(m)} \otimes \vec{S}^{(m)}\right] + \vec{S}_0 \otimes \vec{S}_0. \tag{4.1.30}$$

Eqs. (3.1.2) – (3.1.4) are used to arrive at Eq. (4.1.30), since

$$E\left[\vec{e}^{(m)} \otimes \vec{S}_0\right] = E\left[\vec{e}^{(m)}\right] \otimes \vec{S}_0 = 0. \tag{4.1.31}$$

$$E\left[\vec{\varepsilon}^{(m+1)} \otimes \vec{S}_0\right] = E\left[\vec{\varepsilon}^{(m+1)}\right] \otimes \vec{S}_0 = 0. \tag{4.1.32}$$

Solving for $\mathbf{A}_0$ yields

$$\mathbf{A}_0 = \left\{E\left[\vec{S}^{(m+1)} \otimes \vec{S}^{(m)}\right] - \vec{S}_0 \otimes \vec{S}_0\right\}\left\{E\left[\vec{S}^{(m)} \otimes \vec{S}^{(m)}\right]\right\}^{-1}. \tag{4.1.33}$$

Since $\vec{S}_0 \otimes \vec{S}_0$ is estimated as $E\left[\vec{S}^{(m)} \otimes \vec{S}^{(m)}\right]$, this becomes

$$\mathbf{A}_0 = E\left[\vec{S}^{(m+1)} \otimes \vec{S}^{(m)}\right]\left\{E\left[\vec{S}^{(m)} \otimes \vec{S}^{(m)}\right]\right\}^{-1} - \mathbf{I}. \tag{4.1.34}$$

where $\mathbf{I}$ is the identity matrix. If the NP matrix is calculated using the actual source values instead of the fluctuation, the only difference is the subtraction of the identity

matrix. With this subtracted, the NP matrix is equivalent to the matrix defined previously that uses the source fluctuation.

Next, the eigenvalue calculation will be derived using only the source values. Starting with Eq. (4.1.27) and following a derivation similar to the projection process described in Section 3.1, a new times series can be written as

$$y^{(m+1)} = \lambda_i y^{(m)} + z^{(m+1)} \tag{4.1.35}$$

after applying an eigenvector $\vec{d}_i$ of $\mathbf{A}_0^*$ to the expansions of $\vec{S}^{(m)}$ and $\vec{\eta}^{(m)}$ by the eigenvector $\vec{b}_j$ of $\mathbf{A}_0$. Note that Eq. (4.1.27) and Eq. (3.1.1) are of the same form since only Eqs. (3.1.13) – (3.1.16) were used to derive (3.1.37). In this case, however, the projected series and noise are defined as

$$y^{(m)} = \left\langle \vec{d}_i, \vec{S}^{(m)} \right\rangle \tag{4.1.36}$$

$$z^{(m)} = \left\langle \vec{d}_i, \vec{\eta}^{(m)} \right\rangle. \tag{4.1.37}$$

To solve for the autocorrelation coefficient, a similar process is followed. $y^{(m)}$ is multiplied throughout and the expectation of the quantities is taken:

$$E\left[y^{(m+1)} y^{(m)} \right] = \lambda_i E\left[y^{(m)} y^{(m)} \right] + E\left[z^{(m+1)} y^{(m)} \right]. \tag{4.1.38}$$

In this case, the last term in Eq. (4.1.38) is

$$\begin{aligned} E\left[z^{(m+1)} y^{(m)} \right] &= E\left[\left\langle \vec{d}_i, \vec{\eta}^{(m+1)} \right\rangle \left\langle \vec{d}_i, \vec{S}^{(m)} \right\rangle \right] \\ &= \left\langle \vec{d}_i \otimes \vec{d}_i, E\left[\vec{\eta}^{(m+1)} \otimes \vec{S}^{(m)} \right] \right\rangle \end{aligned}, \tag{4.1.39}$$

again, proven in Appendix A. The expectation term inside the inner product is simply

$$\begin{aligned} E\left[\vec{\eta}^{(m+1)} \otimes \vec{S}^{(m)} \right] &= E\left[\left(\vec{S}_0 + \vec{\varepsilon}^{(m+1)} \right) \otimes \left(\vec{S}_0 + \vec{e}^{(m)} \right) \right] \\ &= \vec{S}_0 \otimes \vec{S}_0 \end{aligned} \tag{4.1.40}$$

reducing Eq. (4.1.39) to

$$E\left[z^{(m+1)}y^{(m)}\right]=\left\langle \vec{d}_i\otimes\vec{d}_i,\vec{S}_0\otimes\vec{S}_0\right\rangle=0. \tag{4.1.41}$$

To prove Eq. (4.1.41) is zero, we consider that for $\lambda_i\neq 0$

$$\begin{aligned}\lambda_i\left\langle \vec{d}_i,\vec{S}_0\right\rangle&=\left\langle \lambda_i\vec{d}_i,\vec{S}_0\right\rangle\\&=\left\langle \mathbf{A}_0^{\mathbf{T}}\vec{d}_i,\vec{S}_0\right\rangle\\&=\left\langle \vec{d}_i,\mathbf{A}_0\vec{S}_0\right\rangle\\&=0\end{aligned} \tag{4.1.42}$$

where Eq. (3.1.14) was used at the second step and Eq. (2.2.58) was used at the last step. Since $\left\langle \vec{d}_i\otimes\vec{d}_i,\vec{S}_0\otimes\vec{S}_0\right\rangle=\left\langle \vec{d}_i,\vec{S}_0\right\rangle\left\langle \vec{d}_i,\vec{S}_0\right\rangle$, Eq. (4.1.41) is zero. Thus, Eq. (4.1.38) can be written

$$\left\langle \vec{d}_i\otimes\vec{d}_i,E\left[\vec{S}^{(m+1)}\otimes\vec{S}^{(m)}\right]\right\rangle=\lambda_i\left\langle \vec{d}_i\otimes\vec{d}_i,E\left[\vec{S}^{(m)}\otimes\vec{S}^{(m)}\right]\right\rangle \tag{4.1.43}$$

and the eigenvalue λ_i is solved for as

$$\lambda_i=\frac{\left\langle \vec{d}_i\otimes\vec{d}_i,E\left[\vec{S}^{(m+1)}\otimes\vec{S}^{(m)}\right]\right\rangle}{\left\langle \vec{d}_i\otimes\vec{d}_i,E\left[\vec{S}^{(m)}\otimes\vec{S}^{(m)}\right]\right\rangle}. \tag{4.1.44}$$

In this way any eigenvalue ratio can be determined in the same way using the actual source rather than the fluctuation (except for the subtraction of the identity matrix **I** in Eq. (4.1.34)). These two results, whereby the NP matrix and eigenvalue ratios are computed on-the-fly using the actual source and storing only two covariance matrices, will greatly help to reduce the computer storage memory required for implementing this method into production codes.

MCNP Calculation Results

The above implementation was coded into MCNP5 and tested on several problems. To check that the method was properly coded and that the theory was accurate, the Problem 3 checkerboard was tested first. The problem parameters remained exactly the same. The DR result is shown in Table 17 using 1,000 particles per cycle, 200 inactive cycles and 500 active cycles and a 4-bin mesh, compared against the benchmark discrete ordinates method. Table 18 shows the first four eigenvalues using 5,000 particles per cycle, 200 inactive cycles and 1000 active cycles and a 36-bin mesh, compared against the previous benchmark FMM results using a 2,304-bin mesh.

	Benchmark by Discrete Ordinates	CMPM 2σ Interval Using 4-bin Mesh	Benchmark Contained in 2σ?
k_1/k_0	0.9581	(0.92426, 0.97918)	Yes

Table 17: DR of Problem 3 Using MCNP5
Benchmark vs CMPM with Minimum 4-bin Mesh and 2σ std. dev.

	FMM Using 2304-bin Mesh	CMPM 2σ Interval Using 36-bin Mesh	FMM Result Contained in 2σ?
k_1/k_0	0.95740	(0.92797, 0.96821)	Yes
k_2/k_0	0.95710	(0.91445, 0.95877)	Yes
k_3/k_0	0.92031	(0.87892, 0.93404)	Yes
k_4/k_0	0.89708	(0.87892, 0.93404)	Yes

Table 18: First Four Eigenvalue Ratios of Problem 3 Using MCNP5
Benchmark vs CMPM with 36-bin Mesh and 2σ std. dev.

In all cases were the benchmark results contained within the 2σ interval. The interval ranges were typically large because only 1,000 active cycles were used. However, these results give proof of principle.

The Fission Matrix Method was also implemented into MCNP5 recently, though not by the author. CMPM was tested against FMM using coarse meshes to emphasize the difference in accuracy between methods. The Problem 3 checkerboard was tested again using 5,000 particles per cycle, 200 inactive cycles and 1,000 active cycles. Table 19 compares DR using a 4-bin mesh. Table 20 compares DR using a 36-bin mesh.

	Benchmark by Discrete Ordinates	CMPM ± 1σ Using 4-bin Mesh	FMM Using 4-bin Mesh
k_1/k_0	0.9581	0.95449 ± 0.00943	0.88913

Table 19: DR of Problem 3 Using MCNP5
Benchmark vs CMPM vs FMM with Minimum 4-bin Mesh and 1σ std. dev.

	Benchmark by Discrete Ordinates	CMPM ± 1σ Using 36-bin Mesh	FMM Using 36-bin Mesh
k_1/k_0	0.9581	0.94809 ± 0.01006	0.93513

Table 20: DR of Problem 3 Using MCNP5
Benchmark vs CMPM vs FMM with 36-bin Mesh and 1σ std. dev.

As predicted by the theory, CMPM consistently estimates DR accurately using the minimum mesh size. FMM performs poorly in both cases, though it improves when the mesh becomes finer due to the decrease in discretization error. It is worth noting that the on-the-fly CMPM DR calculations in MCNP5 do not add significantly to run time since the major calculations involved are to inverse and solve a very small matrix.

The next problem analyzed (Problem 6) is a two dimensional version of an initial core pressurized water reactor (PWR) problem with continuous-energy cross-sections (Nakagawa, 1993). The problem is illustrated in Figure 21; the computation was run using reflecting top and bottom boundaries. k_{eff} for this problem is 1.0187 ± 0.0004 (1σ) using the continuous-energy model.

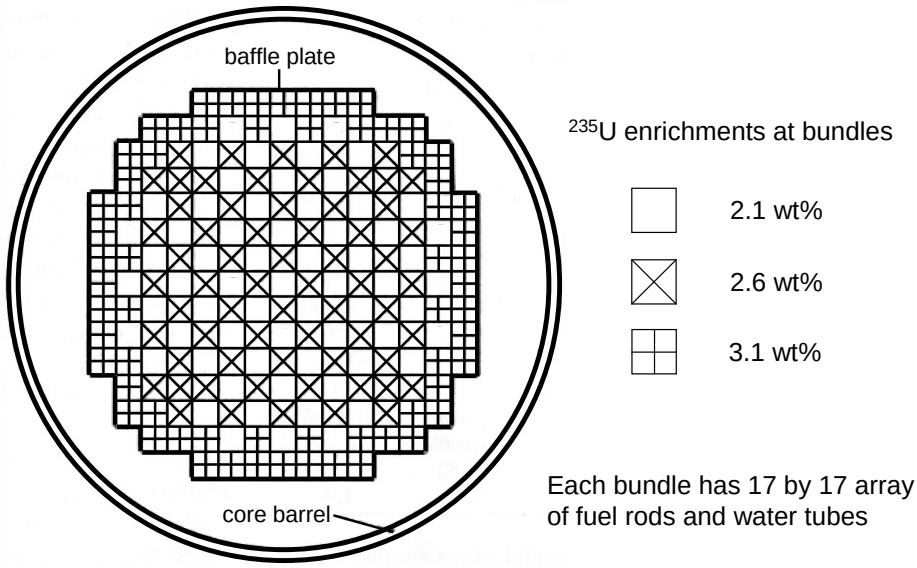

Figure 21: Problem 6 – 2D PWR Initial Core

Table 21 compares the benchmark DR computed by the ARMA(2,1) half-domain fitting method against CMPM using 200,000 particles per cycle, 1,000 inactive cycles, 9,000 active cycles and a 4-bin mesh. As can be seen, CMPM performs well even for realistic problems with complicated geometry and material placement.

	Benchmark by ARMA(2,1) HDFM	CMPM 2σ Interval Using 4-bin Mesh	Benchmark Contained in 2σ?
k_1/k_0	0.992651 ± 0.001731	(0.98782, 0.99356)	Yes

Table 21: DR of Problem 6 Using MCNP5
Benchmark vs CMPM with Minimum 4-bin Mesh and 2σ std. dev.

One final analysis was made using Problem 6 and Problem 7. Problem 7 is a three-dimensional version of Problem 6. It is nearly the same as Problem 6 except that it includes the plenum, top and bottom end plugs inside Zirconium cladding, and top and

bottom supports. The detailed specifications are found in (Nakagawa, 1993). k_{eff} for this problem is 1.01249 ± 0.00055 (1σ) using the continuous-energy model. DR was calculated using basic CMPM mesh (four bins for Problem 6 and eight bins for Problem 7) and contrasted against FMM using a varying number of bins. This was done to illustrate the advantage of CMPM over FMM, especially in three-dimensional analysis where thousands of bins may be required for FMM to calculate the eigenvalues accurately. Problem 6 was run using 5,000 particles per cycle, 200 inactive cycles and 1,000 active cycles and is shown in Figure 22. Problem 7 was run using 20,000 particles per cycle, 200 inactive cycles and 2,000 active cycles and is shown in Figure 23. Trend lines were added to estimate the number of FMM bins necessary to reach the 1σ CI of the CMPM estimate using only 8-bins.

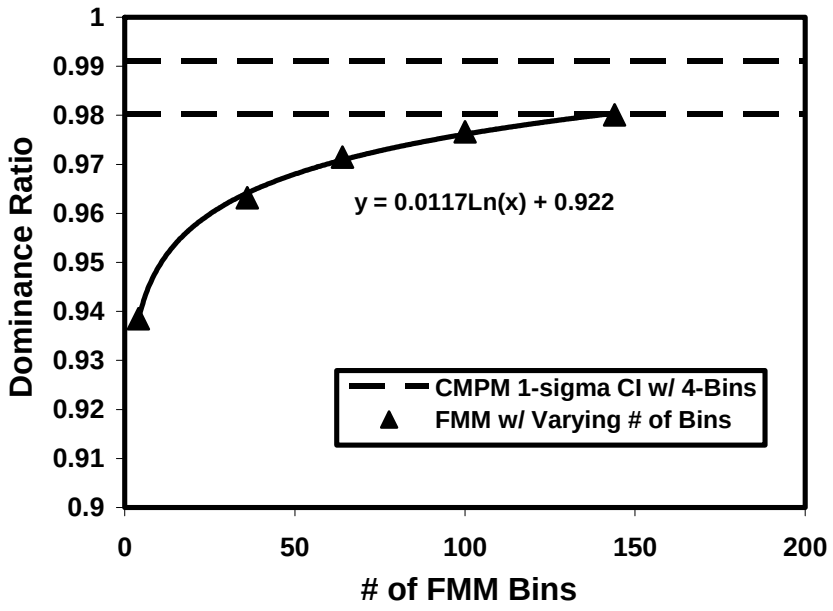

Figure 22: 2D PWR Comparison FMM vs CMPM

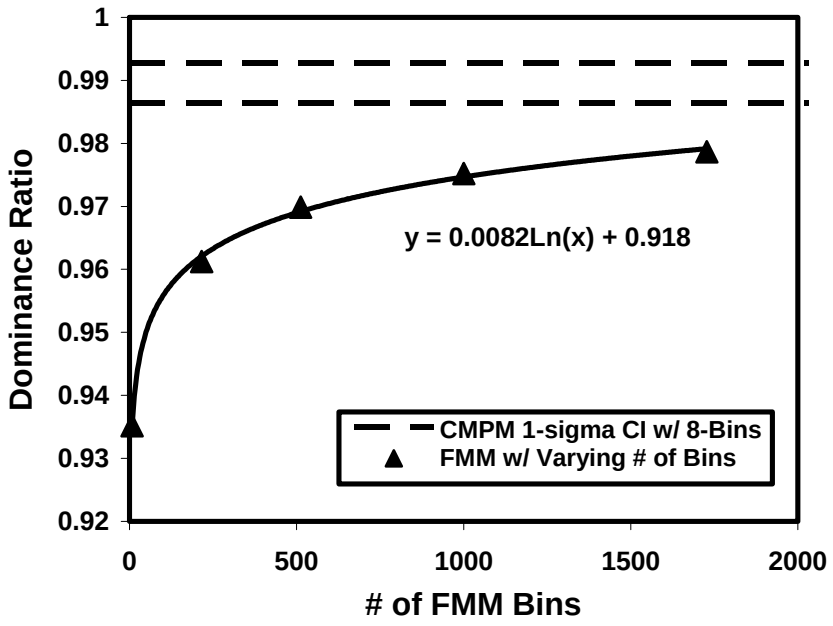

Figure 23: 3D PWR Comparison FMM vs CMPM

As can be seen, FMM needs significantly more bins to accurately estimate DR, especially in Problem 7. The number of bins necessary for FMM to compute DR within the CMPM 1σ CI is estimated to be 146 for Problem 6 and 4,169 for Problem 7 using the trend lines. CMPM requires only four bins for Problem 6 and eight bins for Problem 7. This is a significant difference that highlights the benefit of CMPM for large three-dimensional analysis.

Chapter 5: Summary, Conclusions and Future Work

A novel method of computing the k-eigenvalues of the neutron transport equation in Monte Carlo calculations was presented. This Coarse Mesh Projection Method applies time series techniques to the MC fission source, eliminating the effects of discretization error that arise in other methodologies such as deterministic methods or the Fission Matrix Method. The application of time series techniques allows for the largest non-fundamental eigenvalues to be calculated using very coarse mesh schemes (as few as two bins per coordinate direction) making the calculations extremely fast and efficient. To accurately calculate the eigenvalues, however, certain conditions must be met. First, there must be minimal-to-no cancellation of the eigenmode over the source tally bins. The effect of other eigenmodes must also be removed, but this occurs automatically in CMPM by using the transpose of the NP matrix. Second, we impose that a number of active cycles equal to roughly

$$\eta_{AC} = \max\left[500, \frac{\ln\left(10^{-3}\right)}{\ln\left(\lambda_1\right)}\right]$$

must be used to ensure unbiased results. In cases where the eigenvalues are very close in magnitude $\left(k_{i+1}/k_i > 0.99\right)$ more cycles are necessary to calculate the degenerate eigenvalue k_{i+1} accurately. Also, when $k_{i+1}/k_i > 0.99$ complex conjugate eigenvalues of the NP matrix frequently arise. We have shown that if the imaginary part of the complex eigenvalue is small, the real part of the eigenvector can safely be used. For cases when the imaginary part is not negligible, the method of autoregressive fitting for a complex

valued time series was presented. The magnitude of the imaginary part of the complex eigenvalues was numerically shown to decrease roughly as N^{-1} or $N^{-1/2}$, where N is the number of active cycles. Finally, a robust implementation method was presented where alternate representations were derived for calculating the noise propagation matrix and eigenvalue ratio. These derivations were significant since they allowed for on-the-fly application of the CMPM method and a minimization of necessary computer memory.

There are many further areas of study that could be explored with regard to this method. Application of the method to other geometries, such as spherical problems or problems with rotational symmetry, would be worthwhile. A stronger requirement for the necessary number of active cycles should also be investigated. A specific correlation distance between cycles does not always provide an accurate gauge, especially when there is multiplicity or degenerate eigenvalues. Perhaps the application of informatics-based diagnostics could prove beneficial for problems with highly correlated cycles. Another area of study should be the source tally mesh schemes, since they must be placed so as to prevent cancellation of the desired eigenmode to keep the fitting order as simple as possible (i.e. AR(1)). The ultimate goal would be to find the zeroes of the desired eigenmode and place the bin boundaries at those points. This does not appear to be computationally feasible at first glance, so other ideas have been considered. For instance, it is theorized that for DR calculations of a 1-D problem the zero of the eigenmode will roughly correspond to the point H when

$$\int_0^H S(\vec{r})d\vec{r} = \int_H^L S(\vec{r})d\vec{r} = \frac{1}{2}\int_0^L S(\vec{r})d\vec{r}$$

where 0 and L are the slab boundaries and H is some point in between. An investigation into the properties of the zeroes of eigenmodes would be worthwhile to determine when this is true and if it could extend to other higher order eigenmodes.

Appendix A

The equalities below are proven in this appendix:

$$\left\langle \vec{a}, \vec{R}^{(m+l)} \right\rangle \left\langle \vec{b}, \vec{S}^{(m)} \right\rangle = \left\langle \vec{a} \otimes \vec{b}, \vec{R}^{(m+l)} \otimes \vec{S}^{(m)} \right\rangle, \tag{5.1.1}$$

$$E\left[\left\langle \vec{a}, \vec{R}^{(m+l)} \right\rangle \left\langle \vec{b}, \vec{S}^{(m)} \right\rangle \right] = \left\langle \vec{a} \otimes \vec{b}, E\left[\vec{R}^{(m+l)} \otimes \vec{S}^{(m)} \right] \right\rangle, \tag{5.1.2}$$

where $\vec{a}, \vec{b}, \vec{R}^{(m+l)}, \vec{S}^{(m)}$ are all column vectors quantities, i.e. $\vec{S}^{(m)} = \left(S_1^{(m)}, S_2^{(m)}, \cdots, S_p^{(m)} \right)^{\mathbf{T}}$, and $\vec{R}^{(m+l)}, \vec{S}^{(m)}$ are stochastic quantities while $\vec{a}, \vec{b}$ are deterministic. These equalities are used multiple times throughout the work and are important to understanding many of the derivations. Note that $\left\langle \vec{a}, \vec{R}^{(m+l)} \right\rangle$ signifies a dot product (equivalent to $\vec{a}^{\mathbf{T}} \vec{R}^{(m+l)}$) and $\vec{a} \otimes \vec{R}^{(m+l)}$ signifies an outer product (equivalent to $\vec{a}\left(\vec{R}^{(m+l)} \right)^{\mathbf{T}}$). All vector quantities have the same number of elements, *p*.

Expanding the inner products on the LHS of Eq. (5.1.1) yields

$$LHS = \sum_{j=1}^{p} \left[a_j R_j^{(m+l)} \right] \cdot \sum_{j=1}^{p} \left[b_j S_j^{(m)} \right]. \tag{5.1.3}$$

Expanding each summation term results in

$$= \left(a_1 R_1^{(m+l)} + \cdots + a_p R_p^{(m+l)} \right) \left(b_1 S_1^{(m)} + \cdots + b_p S_p^{(m)} \right). \tag{5.1.4}$$

Next, each of the terms is multiplied out and rearranged yielding

$$= a_1 b_1 R_1^{(m+l)} S_1^{(m)} + \cdots + a_1 b_p R_1^{(m+l)} S_p^{(m)} + \cdots + a_p b_p R_p^{(m+l)} S_p^{(m)}. \tag{5.1.5}$$

Now, the vector terms $a_j b_k$ are written under two summation terms as

$$= \sum_{k=1}^{p} \left[\sum_{j=1}^{p} \left[a_j b_k R_j^{(m+l)} S_k^{(m)} \right] \right]. \tag{5.1.6}$$

This final arrangement is quite interesting and is strikingly similar to a Frobenius inner product of two matrices. If we define matrices such that

$$\mathbf{A} = \vec{a} \otimes \vec{b} \tag{5.1.7}$$

$$\mathrm{B}^{(l)} = \vec{R}^{(m+l)} \otimes \vec{S}^{(m)} \tag{5.1.8}$$

we can see that it is indeed a Frobenius inner product

$$= \sum_{k=1}^{p} \left[\sum_{j=1}^{p} \left[\mathrm{A}_{jk} \mathrm{B}_{jk}^{(l)} \right] \right]. \tag{5.1.9}$$

and can write the final rearrangement succinctly as

$$= \left\langle \vec{a} \otimes \vec{b}, \vec{R}^{(m+l)} \otimes \vec{S}^{(m)} \right\rangle. \tag{5.1.10}$$

Eq. (5.1.2) follows immediately from this result. Taking the expectation of both sides of Eq. (5.1.1) yields

$$E\left[\left\langle \vec{a}, \vec{R}^{(m+l)} \right\rangle \left\langle \vec{b}, \vec{S}^{(m)} \right\rangle \right] = E\left[\left\langle \vec{a} \otimes \vec{b}, \vec{R}^{(m+l)} \otimes \vec{S}^{(m)} \right\rangle \right]. \tag{5.1.11}$$

Since $\vec{a}, \vec{b}$ are deterministic quantities this simply becomes

$$E\left[\left\langle \vec{a}, \vec{R}^{(m+l)} \right\rangle \left\langle \vec{b}, \vec{S}^{(m)} \right\rangle \right] = \left\langle \vec{a} \otimes \vec{b}, E\left[\vec{R}^{(m+l)} \otimes \vec{S}^{(m)} \right] \right\rangle. \tag{5.1.12}$$

Appendix B

The process of bin placement and bin merging for CMPM is covered in this appendix. To quickly remind the reader, bins are only placed over regions where the fission source is tallied. If a bin is placed over a region that does not have fissile material, the associated matrix location is removed before the CMPM calculation. For the results in this work, the problems were usually run only once using a finer bin scheme and collapsed down to a coarse mesh for the CMPM calculations. For example, for the one-dimensional Problem 2, the typical procedure was as follows: apply 101 source bins over the entire domain as shown in Figure 24. Before the CMPM calculation, all of the 101 bins are checked to ensure they are non-zero. If any of the bins is zero (as is the case for the center bin for this arrangement according to Figure 24), those bins are removed.

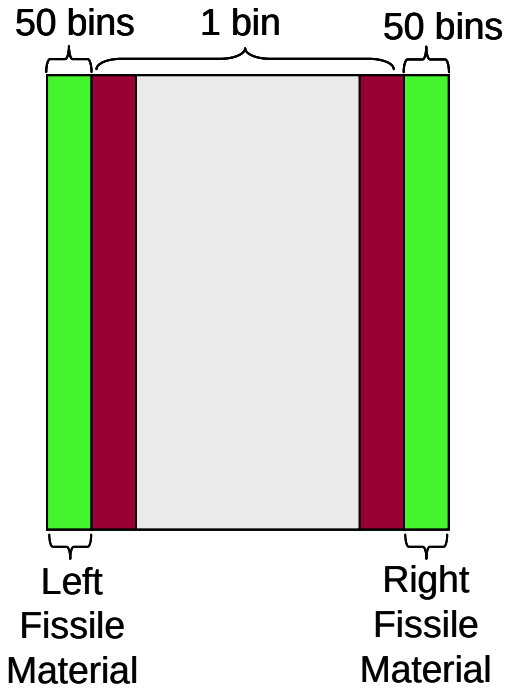

Figure 24: Bin Placement for Problem 2

Next, the remaining bins are collapsed down to the desired number of bins for the CMPM calculation. For example, the remaining fissile material in Figure 24 is combined down to four bins in Figure 25.

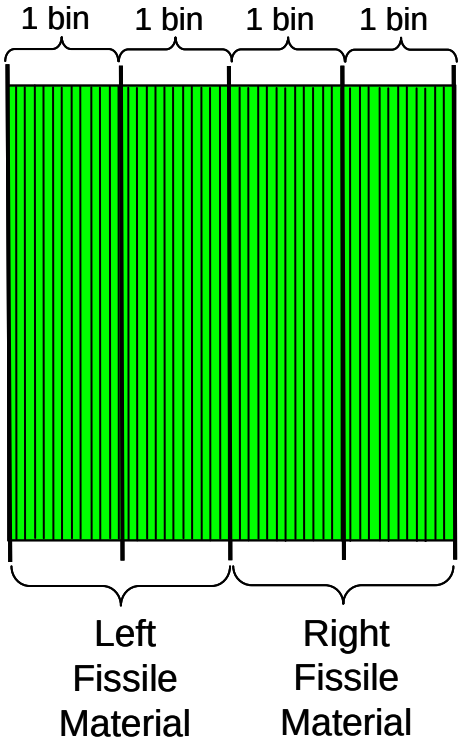

Figure 25: Bin Merging for Problem 2

For the two-dimensional problems, the bins are combined over each coordinate axis. Consider Problem 3, which is illustrated in Figure 26. Originally, source bins were placed such that each square of material in the checkerboard had one source tally bin assigned to it (36 bins in total, 6 per coordinate direction). These bins were combined down to four bins total (2 per coordinate direction) as shown in Figure 26.

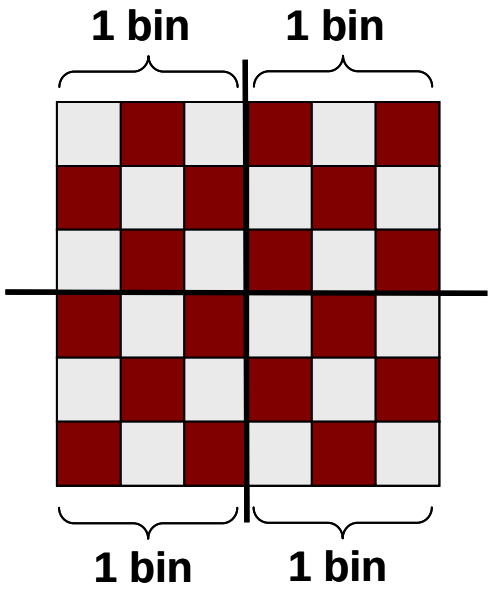

Figure 26: Bin Placement and Merging for Problem 3

References

Akaike H. (1974). Markovian representation of stochastic processes and its application to the analysis of autoregressive moving average processes, Ann. of the Inst. of Stat. Math., 26, pp 363-387.

Box G.E., Jenkins G.M., Reinsel G.C. (1997). *Time series analysis: forecasting and control*, Prentice-Hall, Inc., Upper Saddle River, NJ.

Brissenden R.J., Garlick A.R. (1986). Biases in the estimation of keff and its error by monte carlo methods, Annals of Nuclear Energy, 13, pp 63-83.

Brown F.B., Nease B.R., Ueki T. (2008). Dominance ratio calculations with MCNP, submitted to International Conference on Reactor Physics.

Cover T.M., Thomas J.A. (1991). *Information theory*, John Wiley & Sons, NY.

Demaret L., *et. al.* (1999). Accurate determination of confidence intervals in monte carlo eigenvalue calculations, Proc. 6th Int. Conf. Nuclear Criticality Safety, Versailles, France.

Duderstadt J., Hamilton L. (1976). *Nuclear reactor analysis*, John Wiley & Sons, NY.

Gelbard E.M., Prael R.E. (1974). Monte carlo work at Argonne National Laboratory, ANL-75-2, Argonne National Laboratory.

Hashimoto K. (1993). Linear modal analysis of out-of-phase instability in boiling water reactor cores, Annals of Nuclear Energy, 20, 12, pp 789-797.

Jacquet O., *et. al.* (2001). Eigenvalue uncertainty evaluation in mc calculations using time series methodologies, Advanced Monte Carlo for Radiation Physics, Particle Transport Simulation and Applications, Proc. Monte Carlo 2000 Conf., Libson, Portugal.

Kornreich D.E., Ganapol B.D. (2003). The green's function method for nuclear engineering applications, Nuc. Sci. and Eng., 31, p. 293.

MacMillan D. (1973). Monte carlo confidence limits for iterated-source calculations, Nuc. Sci. and Eng., 50, pp 73-87.

Miro R., *et al.* (2002). A nodal modal method for the neutron diffusion equation. Application to BWR instabilities analysis, Annals of Nuc. Energy, 29, pp 1171-1194.

Morrisson G.W., Mihalczo J.T., Irving D.C. (1966). REACT and CONVERG fortran subroutines for determining source convergence for the O5R monte carlo neutron transport code, ORNL-TM-1325, Oak Ridge National Laboratory.

Morton K.W. (1956). Criticality calculations by monte carlo methods, AERE-TR-1903, Harwell.

Nakagawa M., Mori T. (1993). Whole core calculations of power reactors by use of monte carlo method, Journal of Nuc. Sci. and Tech., 30 [7], pp 692-701.

Nease B.R., Ueki T. (2007). Time series analysis of monte carlo fission sources: III. coarse mesh projection, Nuc. Sci. and Eng., 157, pp. 51-64.

Nease B.R. (2005). Autocorrelation analysis of fission source distributions in monte carlo simulations, Master Thesis, The University of New Mexico.

Parsons D.K., Kornreich, D.E. (2003). Approximations to the dominance ratio using effective and infinite multiplication results, American Nuclear Society, Inc., Proceedings of M&C 2003: A Century in Review – A Century Anew, Gatlinburg, Tennessee, La Grange Park, Illinois.

Priestly M.B. (1981). *Spectral analysis and time series*, Academic Press.

Sahni D.C. (1996). Some new results pertaining to criticality and time eigenvalues of one-speed neutron transport equation, Progress in Nuclear Energy, 30, 3, pp. 305-320.

Storch H., Zwiers F. (1999) *Statistical analysis in climate research*, Cambridge University Press, Cambridge, UK.

Sutton T.M., Brown F.B. (1991). Analysis of the monte carlo eigenvalue bias, (unpublished).

Ueki T., Mori T., Nakagawa M. (1997). Error estimations and their biases in monte carlo eigenvalue calculations, Nuc. Sci. and Eng, 125, pp 1-11.

Ueki T. (2002). Intergenerational correlation in monte carlo k-eigenvalue calculation, Nuc. Sci. and Eng, 141, pp 101-110.

Ueki T., Brown F.B., Parsons D.K., Kornreich D.E. (2003). Autocorrelation and dominance ratio in monte carlo criticality calculations, Nuc. Sci. and Eng., 145, pp 279-290.

Ueki T., Brown F.B., Parsons D.K., Warsa J.S. (2004). Time series analysis of monte carlo fission sources I: dominance ratio computation, Nuc. Sci. and Eng., 148, pp 374-390.

Ueki T., Nease B.R. (2006). Time series analysis of monte carlo fission sources II: confidence interval estimation, Nuc. Sci. and Eng., 153, pp 184-191.

Urbatsch T. (1995). Iterative acceleration methods for monte carlo and deterministic criticality calculations, LA-13052-T, Los Alamos National Laboratory.

Visual Numerics Inc., (1997). *IMSL stat/library Volume 2*, Houston, TX.

Wareing T.A., McGhee J.M., Morel J.E., Pautz S.D. (2001). Discontinuous finite element Sn methods on three-dimensional unstructured grids, Nuc. Sci. and Eng., 138, p 256.

Warsa J.S., et. al. (2000). Krylov subspace iterations for the calculation of k-eigenvalues with Sn transport codes, American Nuclear Society, Inc., Proceedings of M&C 2003: A Century in Review – A Century Anew, Gatlinburg, Tennessee, La Grange Park, Illinois.

X-5 Monte Carlo Team (2003). MCNP – A general purpose monte carlo n-particle transport code: version 5, LA-UR-03-1987, Los Alamos National Laboratory.

Zolotukhin V.G., Mairorov L.V. (1983). An estimate of the systematic errors in the calculation of criticality by the monte carlo method, Atomnaya Energiya, 55, p 173.

Attachment 2

NUCLEAR SCIENCE AND ENGINEERING: **157**, 51–64 (2007)

Time Series Analysis of Monte Carlo Fission Sources—III: Coarse-Mesh Projection

Brian R. Nease and Taro Ueki*

The University of New Mexico, Department of Chemical and Nuclear Engineering
209 Farris Engineering Center
Albuquerque, New Mexico 87131

Received June 5, 2006
Accepted October 20, 2006

Abstract—*A coarse-mesh projection method has been developed for the Monte Carlo calculation of dominant eigenvalue ratio [dominance ratio (DR)]. The first step of the method consists of the regression analysis of the multivariate time series from the coarse-mesh binning of the Monte Carlo fission source distribution. The second step is computation of the eigenvectors of the adjoint matrix of noise propagation. In general, projections on these eigenvectors can be utilized to compute important characteristics of the eigenmodes of fission source distribution. In this work, it has been proven that if the eigenvector corresponding to the largest eigenvalue of the aforementioned adjoint matrix is taken to be the vector for projection, the projected scalar time series follows the autoregressive process of order one with the root of characteristic polynomial, i.e., the autocorrelation coefficient, being the DR of fission source distribution. Numerical results are presented for four problems including one-energy-group checkerboard-type problems, a one-energy-group cube problem and a continuous-energy pressurized water reactor core problem. The strength of the method is twofold; (a) the elimination of the use of autoregressive moving average fitting, and (b) no need to optimize the order of fitting.*

I. INTRODUCTION

The knowledge and availability of nonfundamental-mode eigenvalues of the fission source distribution are valuable for some types of nuclear reactor analysis. One example is a nodal modal method where eigenvalues including but not limited to the fundamental-mode eigenvalue (k_{eff}) are used to analyze the stability of boiling water reactors.[1,2] Another example is the use of eigenvalue ratios in the confidence interval estimation of the fission source distribution in iterated source Monte Carlo (MC) methods.[3,4] In these examples, a robust method of evaluating dominant eigenvalue ratio [dominance ratio (DR)], i.e., the eigenvalue ratio of first to fundamental modes using continuous-energy nuclear cross-section data, will be desired.

Recent work[5] has shown that the time series analysis of the fission source distribution correctly computes DR. These methodologies utilize the autoregressive moving average (ARMA) model of order 2 and 1 [ARMA(2,1)] with half-domain fitting within the general framework of the ARMA(p, $p-1$) representation of linear noise propagation, and are not constrained by whether the nuclear cross-section data of analyzed problems are energy independent, multigroup energy, or continuous energy. This is a good point. However, ARMA fitting generally utilizes nonlinear least-square iterations after the preliminary parameter guesses.[6,7] The nonlinear least-square iterations involve the backward estimation at the initial values of time series data and the tolerance parameter specifications for convergence control. They are tricky processes and occasionally need fine-tuning. In practice, it is very difficult to have some algorithms automatically cope with such an occasional need of fine-tuning. This aspect of the nonlinear least-square iterations is currently preventing the ARMA(2,1)-based time series methodologies from becoming part of production MC radiation transport codes with reactor/criticality analysis capabilities such as MCNP (Ref. 8).

*E-mail: tueki@unm.edu

In the present work, we have successfully developed a novel time series method of computing DR, which can be made blackbox and thus become part of the production MC radiation transport codes. The method consists of multivariate regression analysis, the computation of the noise propagation matrix, and coarse-mesh projection for generating a new scalar time series. It has been proven that the autocorrelation coefficient of the projection time series is DR if the vector of projection is chosen to be the eigenvector corresponding to the largest eigenvalue of the adjoint matrix of noise propagation. Its theoretical derivation is confirmed by the numerical computation of DR for various problems as well as the examination of Akaike's information criterion[6] (AIC) for selected problems.

II. THEORY

II.A. Preliminaries

In static analysis of nuclear reactors, MC iterated source methods are used to solve an integral equation of the following form:

$$S(\vec{r}) = \frac{1}{k} \int F(\vec{r}' \rightarrow \vec{r}) S(\vec{r}')\, dV' \quad , \tag{1}$$

where

$\vec{r}$ = space coordinate vector

dV = volume element

$S(\vec{r})$ = source distribution

k = eigenvalue

$F(\vec{r}' \rightarrow \vec{r})$ = an integral kernel that can be interpreted as the expected number of direct descendent source particles per unit volume at $\vec{r}$ resulting from a source particle at $\vec{r}'$.

Under the standard notations of neutron transport theory,[9] Eq. (1) may be explicitly written as

$$S(\vec{r}) = \frac{1}{k} \mathbf{F}\mathbf{R}^{-1} \left(\frac{\chi(E)}{4\pi} S(\vec{r}) \right) \quad , \tag{2}$$

where $\chi(E)$ is fission energy spectrum normalized to unity, and $\mathbf{F}$ and $\mathbf{R}$ are the fission and removal operators defined as follows via the operation on the function ϕ of position $\vec{r}$, energy E, and unit vector of direction of movement $\vec{\Omega}$, with the mean number of neutrons per fission ν, the macroscopic fission cross section Σ_f, the macroscopic total cross section Σ_t, and the differential scattering cross section Σ_s:

$$\mathbf{F}\phi = \int_0^{E_{\max}} \int_{4\pi} \nu \Sigma_f(\vec{r}, E') \phi(\vec{r}, E', \vec{\Omega}')\, d\Omega'\, dE' \tag{3}$$

and

$$\begin{aligned} \mathbf{R}\phi = {} & \vec{\Omega} \cdot \nabla \phi(\vec{r}, E, \vec{\Omega}) + \Sigma_t(\vec{r}, E) \phi(\vec{r}, E, \vec{\Omega}) \\ & - \int_0^{E_{\max}} \int_{4\pi} \Sigma_s(\vec{r}, E', \vec{\Omega}' \rightarrow E, \vec{\Omega}) \\ & \times \phi(\vec{r}, E', \vec{\Omega}')\, d\Omega'\, dE' \quad . \end{aligned} \tag{4}$$

The eigenvalue k is ordered $|k_0| > |k_1| > |k_2| > \ldots$, and the corresponding eigenfunctions are denoted $S_i(\vec{r})$, $i = 0, 1, \ldots$, where the subscript 0 implies the fundamental mode and the subscript i is referred to as the i'th mode.

Let the source distribution after simulating the m'th stationary cycle in an MC iterated source computation be $\hat{S}^{(m)}(\vec{r})$. Since $\hat{S}^{(m)}(\vec{r})$ is a stochastic realization, it can be written as

$$\hat{S}^{(m)}(\vec{r}) \equiv NS(\vec{r}) + \sqrt{N}\, \hat{e}^{(m)}(\vec{r}) \quad , \quad m \geq 0 \quad , \tag{5}$$

where

N = number of particles (neutrons) per cycle

$S(\vec{r}) = E[\hat{S}^{(m)}(\vec{r})]/N$, with $E[\cdot]$ denoting expectation

$\hat{e}^{(m)}(\vec{r})$ = fluctuating part of the source distribution $(E[\hat{e}^{(m)}(\vec{r})] = 0)$.

The scaling by N and $\sqrt{N}$ is introduced to clarify the asymptotic behavior of the integrals of individual terms over the domain as $N \rightarrow \infty$. The hat above symbols is used to imply a stochastic realization. The noise component $\hat{\varepsilon}^{(m)}(\vec{r})$ resulting from the source particle selection and the subsequent tracking is introduced as

$$\begin{aligned} & \sqrt{N}\, \hat{\varepsilon}^{(m)}(\vec{r}) \\ & \equiv \hat{S}^{(m)}(\vec{r}) - \frac{N \int F(\vec{r}' \rightarrow \vec{r}) \hat{S}^{(m-1)}(\vec{r}')\, dV'}{\int \hat{S}^{(m-1)}(\vec{r}'')\, dV''} \quad . \end{aligned} \tag{6}$$

Here, with the standard notation for conditional expectation, the following relations hold:

$$\begin{aligned} & E[\hat{S}^{(m)}(\vec{r}) | \hat{S}^{(m-1)}(\vec{r}')] \\ & = \frac{N \int F(\vec{r}' \rightarrow \vec{r}) \hat{S}^{(m-1)}(\vec{r}')\, dV'}{\int \hat{S}^{(m-1)}(\vec{r}'')\, dV''} \end{aligned} \tag{7}$$

and

$$E[\hat{\varepsilon}^{(m)}(\vec{r})|\hat{S}^{(m-1)}(\vec{r}')] = 0 \ . \quad (8)$$

Note that throughout this work the uppercase E is used to denote expectation, except for the energy variables in Eqs. (2) through (4) and the explanation associated with them. The lower case e is used for the fluctuating part of the source distribution. This fluctuating part is governed by an asymptotically linear Markov process[5] as follows:

$$\hat{e}^{(m)}(\vec{r}) = \mathbf{A}_0\hat{e}^{(m-1)}(\vec{r}) + \hat{\varepsilon}^{(m)}(\vec{r}) + O(N^{-1/2}) \ , \quad (9)$$

$$E[\hat{\varepsilon}^{(m1)}\hat{e}^{(m2)}] = 0 \ , \quad m1 > m2 \ , \quad (10)$$

$$E[\hat{\varepsilon}^{(m)}] = 0 \ , \quad (11)$$

and

$$E[\hat{\varepsilon}^{(m1)}\hat{\varepsilon}^{(m2)}] = 0 \ , \quad m1 > m2 \ , \quad (12)$$

where the operator $\mathbf{A}_0$ is defined via the operation on function $f(\vec{r})$ as

$$\mathbf{A}_0(f) \equiv \frac{1}{k_0}\int [F(\vec{r}' \rightarrow \vec{r}) - S_0(\vec{r})](f(\vec{r}'))\, dV' \ , \quad (13)$$

with the following additional requirement:

$$\int S_0(\vec{r})\, dV = k_0 \ . \quad (14)$$

The operator $\mathbf{A}_0$ has the following features:

$$\mathbf{A}_0^i S_0(\vec{r}) = 0 \quad \text{for } i \geq 1 \ , \quad (15)$$

$$\mathbf{A}_0^i[S_j(\vec{r}) - S_0(\vec{r})] = \left(\frac{k_j}{k_0}\right)^i [S_j(\vec{r}) - S_0(\vec{r})]$$

$$\text{for } j \geq 1 \text{ if } \int S_j(\vec{r})\, dV \neq 0 \ \ j \geq 1 \ , \quad (16)$$

and

$$\mathbf{A}_0^i S_j(\vec{r}) = \left(\frac{k_j}{k_0}\right)^i S_j(\vec{r})$$

$$\text{for } j \geq 1 \text{ if } \int S_j(\vec{r})\, dV = 0 \ \ j \geq 1 \ , \quad (17)$$

where in Eq. (16) $S_j(\vec{r})$ is normalized to be k_j, i.e., $\int S_j(\vec{r})\, dV = k_j$.

II.B. Computation of Noise Propagation Matrix

Let us consider the discrete form of Eqs. (9) through (12):

$$\vec{e}^{(m)} = \mathbf{A}_0\vec{e}^{(m-1)} + \vec{\varepsilon}^{(m)} \ , \quad (18)$$

$$E[\vec{\varepsilon}^{(m1)}(\vec{e}^{(m2)})^T] = 0 \ , \quad m1 > m2 \ , \quad (19)$$

$$E[\vec{\varepsilon}^{(m)}] = 0 \ , \quad (20)$$

and

$$E[\vec{\varepsilon}^{(m1)}(\vec{\varepsilon}^{(m2)})^T] = 0 \ , \quad m1 > m2 \ , \quad (21)$$

where $\vec{e}^{(m)}$ and $\vec{\varepsilon}^{(m)}$ are $p \times 1$ matrices (column vectors with p entries), $\mathbf{A}_0$ is assumed to be the operator in Eq. (13) for function cases and the corresponding $p \times p$ matrix for discrete cases, and T implies transpose. Note that p stands for the number of bins.

The standard technique in multivariate regression analysis allows one to compute the explicit expression of $\mathbf{A}_0$. First, the multiplication of Eq. (18) by $\vec{e}^{(m-1)T}$ from the right yields

$$\vec{e}^{(m+1)}(\vec{e}^{(m)})^T = \mathbf{A}_0\vec{e}^{(m)}(\vec{e}^{(m)})^T + \vec{\varepsilon}^{(m+1)}(\vec{e}^{(m)})^T \ . \quad (22)$$

Taking the expectation of Eq. (22) and applying Eq. (19), one obtains

$$E[\vec{e}^{(m+1)}(\vec{e}^{(m)})^T] = \mathbf{A}_0 E[\vec{e}^{(m)}(\vec{e}^{(m)})^T] \ . \quad (23)$$

Defining

$$\mathbf{L}_0 = E[\vec{e}^{(m)}(\vec{e}^{(m)})^T] \quad (24)$$

and

$$\mathbf{L}_1 = E[\vec{e}^{(m+1)}(\vec{e}^{(m)})^T] \ , \quad (25)$$

the matrix $\mathbf{A}_0$ is expressed as

$$\mathbf{A}_0 = \mathbf{L}_1\mathbf{L}_0^{-1} \ . \quad (26)$$

If $(\vec{e}^{(m)})^T = (e_1^{(m)}, \ldots, e_p^{(m)})$, the explicit form of $\mathbf{A}_0$ is

$$\mathbf{A}_0 = \begin{bmatrix} E[e_1^{(m+1)}e_1^{(m)}], E[e_1^{(m+1)}e_2^{(m)}], \ldots, E[e_1^{(m+1)}e_p^{(m)}] \\ E[e_2^{(m+1)}e_1^{(m)}], E[e_2^{(m+1)}e_2^{(m)}], \ldots, E[e_2^{(m+1)}e_p^{(m)}] \\ \vdots \quad\quad\quad \vdots \quad\quad\quad \vdots \\ E[e_p^{(m+1)}e_1^{(m)}], E[e_p^{(m+1)}e_2^{(m)}], \ldots, E[e_p^{(m+1)}e_p^{(m)}] \end{bmatrix} \begin{bmatrix} E[e_1^{(m)}e_1^{(m)}], E[e_1^{(m)}e_2^{(m)}], \ldots, E[e_1^{(m)}e_p^{(m)}] \\ E[e_2^{(m)}e_1^{(m)}], E[e_2^{(m)}e_2^{(m)}], \ldots, E[e_2^{(m)}e_p^{(m)}] \\ \vdots \quad\quad\quad \vdots \quad\quad\quad \vdots \\ E[e_p^{(m)}e_1^{(m)}], E[e_p^{(m)}e_2^{(m)}], \ldots, E[e_p^{(m)}e_p^{(m)}] \end{bmatrix}^{-1} \ . \quad (27)$$

Therefore, the computation of $\mathbf{L}_0$ and $\mathbf{L}_1$ using sample cross and lag covariances allows one to evaluate $\mathbf{A}_0$.

Equations (16) and (17) allow one to assume that the eigenvalues of the discrete version of $\mathbf{A}_0$ approach $k_i/k_0, i = 1, 2, \ldots,$ if $p \gg 1$ and all bins are sufficiently fine. Such an assumption is also valid for the deterministic computation of k_i/k_0 via solving the statistically computed $\mathbf{A}_0$ in Eq. (27) with some matrix solvers in mathematics libraries if one spends sufficiently large numbers of stationary cycles and particles per cycle. The determination of k_i/k_0 in these ways can be computationally prohibitive, however, because of the large number of bins needed to sufficiently reduce the discretization error. Therefore, it is preferable to use a computational approach that is free of the effect of discretization error. To this end, time series analysis guided by the eigenvectors of $\mathbf{A}_0$ is pursued next.

II.C. Projection Process

The eigenvalue problem of $\mathbf{A}_0$ is

$$\mathbf{A}_0 \vec{b}_i = \lambda_i \vec{b}_i \ , \quad i = 1, \ldots, p \tag{28}$$

and

$$\mathbf{A}_0^* \vec{d}_i = \lambda_i \vec{d}_i \ , \quad i = 1, \ldots, p \ , \tag{29}$$

where $\mathbf{A}_0^*$ is the adjoint matrix of $\mathbf{A}_0$, $\mathbf{A}_0^* = \mathbf{A}_0^T$ because $\mathbf{A}_0$ is real, and by the standard results of linear algebra, $\mathbf{A}_0^*$ and $\mathbf{A}_0$ have the same set of eigenvalues with their eigenvectors satisfying

$$\vec{d}_j^T \vec{b}_i = 0 \quad \text{if } \lambda_j \neq \lambda_i \ . \tag{30}$$

Analysis via the eigensystem of Eqs. (28), (29), and (30) is standard. For example, Brissenden and Garlick[10] utilized the adjoint eigenvector $\vec{d}_j$ to derive the formula of the MC estimation bias of k_0. In this work, $\vec{d}_j$ is utilized to define a projected process from which the eigenvalue ratio k_j/k_0 can be computed in a simple manner.

In order to utilize Eqs. (28) and (29), first repeatedly apply Eq. (18) as follows:

$$\vec{e}^{(m)} = \mathbf{A}_0^m \vec{e}^{(0)} + \mathbf{A}_0^{m-1} \vec{\varepsilon}^{(1)} + \mathbf{A}_0^{m-2} \vec{\varepsilon}^{(2)} + \cdots + \vec{\varepsilon}^{(m)} \ . \tag{31}$$

Second, expand $\vec{\varepsilon}^{(i)}$ as follows:

$$\vec{\varepsilon}^{(i)} = \eta_1^{(i)} \vec{b}_1 + \eta_2^{(i)} \vec{b}_2 + \cdots + \eta_p^{(i)} \vec{b}_p \ , \tag{32}$$

and expand $\vec{e}^{(0)}$ as follows:

$$\vec{e}^{(0)} = b_1^{(0)} \vec{b}_1 + b_2^{(0)} \vec{b}_2 + \cdots + b_p^{(0)} \vec{b}_p \ . \tag{33}$$

Third, rewrite $\vec{e}^{(m)}$ in Eq. (31) using Eqs. (32) and (33) with the aid of Eq. (28) to obtain the following:

$$\begin{aligned} \vec{e}^{(m)} = {} & (b_1^{(0)} \lambda_1^m + \eta_1^{(1)} \lambda_1^{m-1} + \eta_1^{(2)} \lambda_1^{m-2} \\ & + \cdots + \eta_1^{(m-1)} \lambda_1 + \eta_1^{(m)}) \vec{b}_1 \\ & + \cdots \\ & + (b_p^{(0)} \lambda_p^m + \eta_p^{(1)} \lambda_p^{m-1} + \eta_p^{(2)} \lambda_p^{m-2} \\ & + \cdots + \eta_p^{(m-1)} \lambda_p + \eta_p^{(m)}) \vec{b}_p \ . \end{aligned} \tag{34}$$

Fourth, take the projection on $\vec{d}_1$ to yield the following:

$$\begin{aligned} \vec{d}_1^T \vec{e}^{(m)} = {} & (b_1^{(0)} \lambda_1^m + \eta_1^{(1)} \lambda_1^{m-1} + \eta_1^{(2)} \lambda_1^{m-2} \\ & + \cdots + \eta_1^{(m-1)} \lambda_1 + \eta_1^{(m)}) \vec{d}_1^T \vec{b}_1 \\ & + \cdots \\ & + (b_p^{(0)} \lambda_p^m + \eta_p^{(1)} \lambda_p^{m-1} + \eta_p^{(2)} \lambda_p^{m-2} \\ & + \cdots + \eta_p^{(m-1)} \lambda_p + \eta_p^{(m)}) \vec{d}_1^T \vec{b}_p \ . \end{aligned} \tag{35}$$

Suppose that λ_1 has the largest magnitude among λ_i, $i = 1, \ldots, p$ and its multiplicity is q, i.e.,

$$\lambda_1 = \lambda_2 = \cdots = \lambda_q$$

and

$$|\lambda_1| > |\lambda_{q+1}| \geq \cdots \geq |\lambda_p| \ , \tag{36}$$

and

$$\vec{d}_1^T \vec{b}_j = 0 \ , \quad q < j \leq p \ , \tag{37}$$

where Eq. (37) results from Eq. (30). Then Eq. (35) becomes the following:

$$\begin{aligned} \vec{d}_1^T \vec{e}^{(m)} = {} & (b_1^{(0)} \lambda_1^m + \eta_1^{(1)} \lambda_1^{m-1} + \eta_1^{(2)} \lambda_1^{m-2} \\ & + \cdots + \eta_1^{(m-1)} \lambda_1 + \eta_1^{(m)}) \vec{d}_1^T \vec{b}_1 \\ & + \cdots \\ & + (b_q^{(0)} \lambda_1^m + \eta_q^{(1)} \lambda_1^{m-1} + \eta_q^{(2)} \lambda_1^{m-2} \\ & + \cdots + \eta_q^{(m-1)} \lambda_1 + \eta_q^{(m)}) \vec{d}_1^T \vec{b}_q \ . \end{aligned} \tag{38}$$

If m is replaced by $m - 1$ in Eq. (38), one obtains the following:

$$\begin{aligned} \vec{d}_1^T \vec{e}^{(m-1)} = {} & (b_1^{(0)} \lambda_1^{m-1} + \eta_1^{(1)} \lambda_1^{m-2} + \eta_1^{(2)} \lambda_1^{m-3} \\ & + \cdots + \eta_1^{(m-2)} \lambda_1 + \eta_1^{(m-1)}) \vec{d}_1^T \vec{b}_1 \\ & + \cdots \\ & + (b_q^{(0)} \lambda_1^{m-1} + \eta_q^{(1)} \lambda_1^{m-2} + \eta_q^{(2)} \lambda_1^{m-3} \\ & + \cdots + \eta_q^{(m-2)} \lambda_1 + \eta_q^{(m-1)}) \vec{d}_1^T \vec{b}_q \ . \end{aligned} \tag{39}$$

Equations (38) and (39) yield the following:

$$\vec{d}_1^T \vec{e}^{(m)} = \lambda_1 \vec{d}_1^T \vec{e}^{(m-1)} + \vec{d}_1^T (\eta_1^{(m)} \vec{b}_1 + \cdots + \eta_q^{(m)} \vec{b}_q) \ . \tag{40}$$

Equations (32) and (31) yield the following:

$$\vec{d}_1^T \vec{\varepsilon}^{(m)} = \vec{d}_1^T (\eta_1^{(m)} \vec{b}_1 + \cdots + \eta_q^{(m)} \vec{b}_q) \equiv z^{(m)} \ . \tag{41}$$

Now, define a scalar time series as follows:

$$y^{(m)} \equiv \vec{d}_1^T \vec{e}^{(m)} \quad . \tag{42}$$

Eqs. (40) and (41) imply that $y^{(m)}$ satisfies the following:

$$y^{(m)} = \lambda_1 y^{(m-1)} + z^{(m)} \quad . \tag{43}$$

In addition, Eqs. (20) and (21) with Eq. (41) yield the following:

$$E[z^{(m)}] = 0 \ , \tag{44}$$

and

$$E[z^{(m1)} z^{(m2)}] = \vec{d}_1^T E[\vec{\varepsilon}^{(m1)} (\vec{\varepsilon}^{(m2)})^T] \vec{d}_1 = 0 \ , \quad m1 > m2 \ , \tag{45}$$

where, in Eq. (45), $\vec{d}_1^T \vec{\varepsilon}^{(m)} = z^{(m)} = (z^{(m)})^T = (\vec{\varepsilon}^{(m)})^T \vec{d}_1$ is used because $z^{(m)}$ is a scalar. Therefore, $y^{(m)}$ follows the autoregressive (AR) process of order one [AR(1)] with λ_1 as the autocorrelation coefficient.

As stated at the end of Sec. II.B, computing $\mathbf{A}_0$ by matrix solvers would yield $\lambda_1 \approx k_1/k_0$ with discretization error due to the geometric sizes of bins. However, previous work[5] showed that such discretization error does not exist if the fluctuation of binned source is analyzed by time series methods. The numerical results therein convincingly showed that half-domain fitting is enough to get an unbiased estimate of k_1/k_0. However, this half-domain fitting approach is based on the ARMA model of orders p and $p-1$ [ARMA$(p, p-1)$], which was derived via Akaike's theory of Markovian representation.[11] Normally, the least-square implementation of ARMA fitting with the preliminary estimation by the method of moments for AR parts and some iterative computation for moving average parts uses backward estimation[6,7] at the initial value of time series, $\vec{e}^{(0)}$ in this work. However, its automation is difficult, and in some cases the departure of the fluctuation from its typical behavior forces the user of ARMA fitting software to fine-tune the number of time steps for the backward estimation even when time series data are collected from the iteration cycles confirmed by stationary diagnostics. The AR(1) model in Eqs. (43) through (45) is free of such problems. This is a preferred feature for MC code developers who attempt to make DR computation part of production codes like MCNP.

II.D. Coarse-Mesh Projection

In this section, the idea of coarse-mesh projection is developed based on the relation between source binning and the first-mode eigenfunction $[S_1(\vec{r})]$. First, previous work[12] has shown that if the complete cancellation of $S_1(\vec{r})$ occurs at a bin, the fluctuation mode associated with k_1/k_0 disappears for the source at the bin. Second, other previous work[5] has shown that the source binning with the complete cancellation of $S_1(\vec{r})$ can be utilized to compute the next eigenvalue ratio k_2/k_0 via time series analysis. Therefore, the primary question to be asked is the following: Is there any source binning scheme of general nature that always prevents the complete cancellation of $S_1(\vec{r})$ from occurring? The fundamental-mode eigenfunction $[S_0(\vec{r})]$ is everywhere nonnegative, i.e., does not change sign. The first-mode eigenfunction $[S_1(\vec{r})]$ is of antisymmetric nature, i.e., changes sign once if simply put. For example, following the diffusion theory methods,[13] one can find the first- and second-mode eigenfunctions next to the fundamental-mode eigenfunction for a rectangular reactor $-a/2 \le x \le a/2$ and $-b/2 \le y \le b/2$ to be

$$\cos\left(\frac{\pi}{a} x\right) \sin\left(\frac{2\pi}{b} y\right) \tag{46}$$

and

$$\sin\left(\frac{2\pi}{a} x\right) \cos\left(\frac{\pi}{b} y\right) \quad . \tag{47}$$

Therefore, if the half-domain fitting is applied to $0 \le x \le a/2$ and $-b/2 \le y \le b/2$, the complete cancellation of the eigenmode in Eq. (46) occurs. Similarly, if the half-domain fitting is applied to $-a/2 \le x \le a/2$ and $0 \le y \le b/2$, the complete cancellation of the eigenmode in Eq. (47) occurs. On the other hand, if the domain of fitting is $0 \le x \le a/2$ and $0 \le y \le b/2$, no cancellation occurs for both these eigenmodes. Since the first-mode eigenfunction is of antisymmetric nature with respect to x-y Cartesian coordinate axes or diagonal lines, one can consider the scenario in Fig. 1: If the geometry and material distribution are symmetric with respect to x and y Cartesian coordinate axes, the first-mode eigenfunction changes the sign with respect to these axes. If the geometry and material distribution are only diagonally symmetric, the first-mode eigenfunction changes the sign across the diagonal lines. For the binning to pick up the fluctuation associated with the first mode, the integral of source distribution should not cancel out over at least one of the bins. This noncancellation condition is satisfied by the meshes with the four bins in Fig. 1. In general, nearly complete cancellation of very high eigenmodes is likely to occur at all four bins in Fig. 1 because of the frequent sign changes. However, even for problems without any symmetric material placement, the complete cancellation of the first eigenfunction at all four bins in Fig. 1 would not occur, since the first eigenmode is the eigenmode next to the "everywhere nonnegative" fundamental eigenmode. Previous work[5] proposed half-domain ARMA(2,1) fitting and thus demanded the knowledge of first-mode eigenfunction cancellation on the user side of the methodologies. The source binning by four bins for two-dimensional problems does not require such knowledge on the user side of the methodologies. Similarly, the number of bins is two for one-dimensional

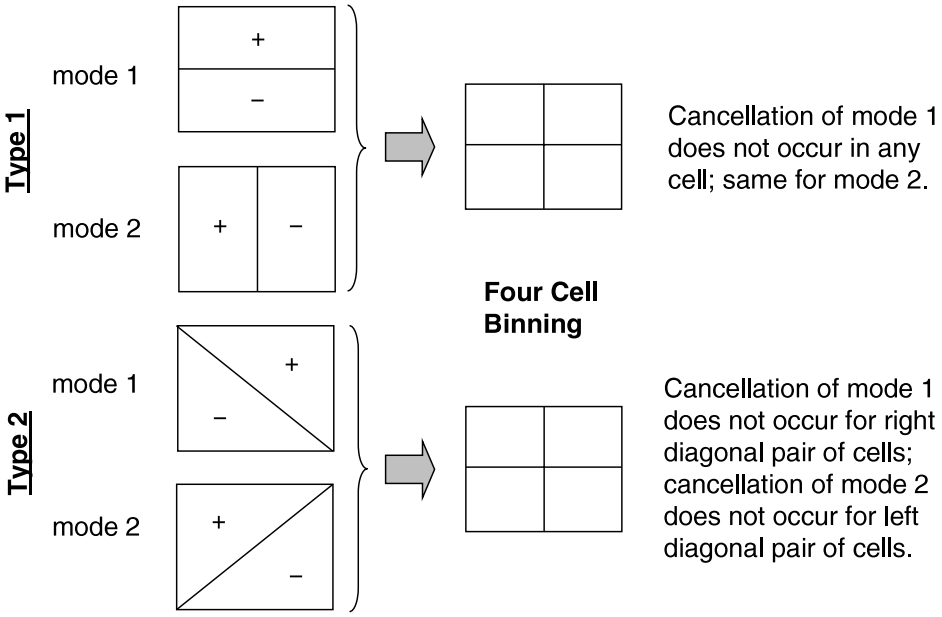

Fig. 1. Four-cell binning and the dominant eigenmodes ($S_1(\vec{r})$ & $S_2(\vec{r})$) next to fundamental eigenmode ($S_0(\vec{r})$) in two-dimensional problems.

geometry and eight for three-dimensional right-parallelepiped geometry. With these coarse binning meshes, the projection series on the eigenvector corresponding to the largest eigenvalue of the adjoint of noise propagation matrix ($\mathbf{A}_0^*$) is computed. The theory of Sec. II.C implies that the autocorrelation of the projection series, which is the coefficient of its AR(1) fitting, is k_1/k_0. This is the coarse-mesh projection method for DR computation.

III. NUMERICAL RESULTS

In this section, the coarse-mesh projection method is applied to four problems to check that AR(1) reliably computes DR as implied in Eqs. (43), (44), and (45). However, for comparison purposes, DRs computed by AR(n), $n \geq 2$, and AR(1) and ARMA(2,1) with half-domain fitting are also displayed. The explicit expression of these DRs is

$$\mathrm{DR} = \frac{k_1}{k_0} = \begin{cases} \text{autocorrelation coefficient } [\lambda_1 \text{ in Eq. (43)}] \ , \\ \quad \text{for AR(1)}, \\ \text{largest zero of characteristic polynomial,} \\ \quad \text{for AR}(n), n \geq 2, \text{ and ARMA(2,1)}. \end{cases} \tag{48}$$

The second relation in Eq. (48) is based on the following general results, first derived in the statistics community[11] and recently rediscovered in the nuclear engineering community,[5] for the projection processes from the linear noise propagation in Eq. (18):

Let $\vec{e}^{(m)}$ be a column vector with p entries

(equivalent to assuming p bins).

Define $\vec{y}^{(m)} = C\vec{e}^{(m)}$; C is a matrix with p columns.

$$|\lambda \mathbf{I} - \mathbf{A}_0| \equiv \lambda^p + \sum_{n=1}^{p} a_n \lambda^{p-n}$$

(characteristic polynomial of $\mathbf{A}_0$);

I is the identity matrix . (49)

$$E_i \equiv C(A_0^i + a_1 A_0^{i-1} + \cdots + a_i I) \ , \quad E_0 = C \ . \tag{50}$$

$$\vec{y}^{(n+p)} + a_1 \vec{y}^{(n+p-1)} + \cdots + a_p \vec{y}^{(n)} = E_0 \vec{\varepsilon}^{(n+p)} + E_1 \vec{\varepsilon}^{(n+p-1)} + \cdots + E_{p-1} \vec{\varepsilon}^{(n+1)} \ . \tag{51}$$

The characteristics polynomial of the process in Eq. (51):

$$x^p + a_1 x^{p-1} + \cdots + a_{p-1} x + a_p \ . \tag{52}$$

Note that the largest zero of characteristic polynomial of AR(1) is $-a_1$, which corresponds to λ_1 in Eq. (43) and thus is autocorrelation coefficient; Eq. (48) is consistent.

The first problem (problem 1) is the one-energy-group checkerboard problem shown in Fig. 2. This problem appeared in previous work.[5] Figure 3 shows the DRs

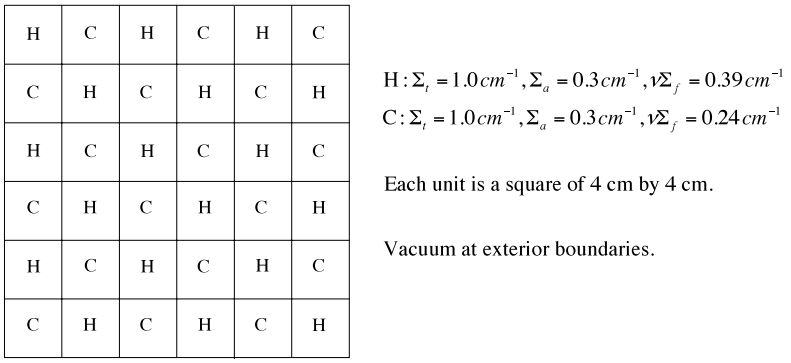

Fig. 2. Description of problem 1.

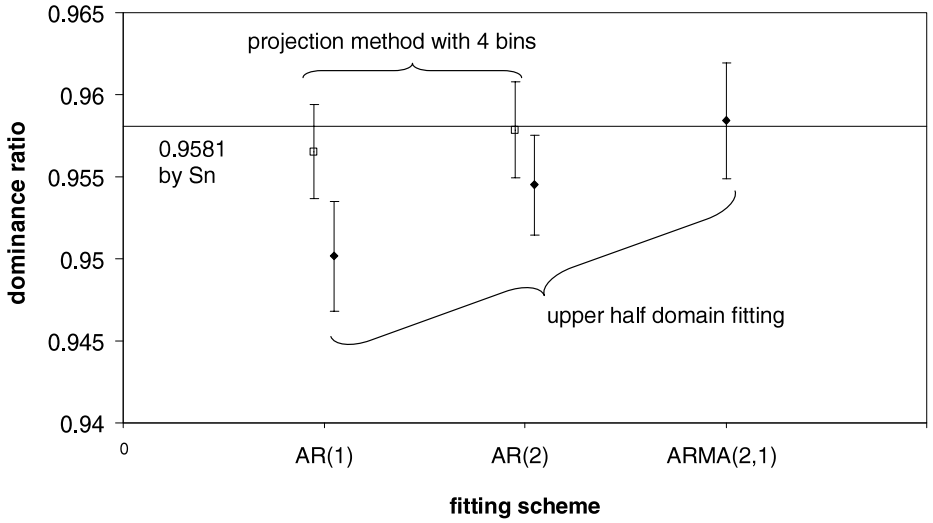

Fig. 3. Dominance ratio of problem 1 computed by coarse-mesh projection with four bins (confidence interval of 2σ).

computed by the coarse-mesh projection with four bins, along with the DRs that appeared in the same previous work. It is observed that the estimate by the AR(1) fitting with the coarse-mesh projection agrees with the estimate by the discrete ordinates method, while the estimates by the half-domain AR(1) fitting is poor. Figure 4 shows the AIC value[6] for determining the order of AR fitting, the definition of which is as follows:

$$\text{AIC} = M \ln(\sigma^2) + 2(q+1) \ , \tag{53}$$

where

M = number of active cycles

σ^2 = residual variance

q = order of fitting.

It is observed that the AIC value starts fluctuating at order two. From these two figures, one can conclude that the theory developed in Sec. II.C has been numerically confirmed.

It is very important to study what happens if one does not follow the coarse-mesh projection. Figure 5 shows the DRs computed by the 36-bin projection (one bin assigned to each unit) as opposed to the coarse-mesh projection with four bins. Poor performance is observed for AR(1) fitting, but the performance of AR(3), AR(4), and AR(5) is acceptable. This is an observed general trend, which is caused by the large statistical error of the projection vector due to fine binning. Note that when the statistical error of the projection vector is large, Eq. (43) is not an accurate representation. However, the good performance of AR(3), AR(4), and AR(5) in Fig. 5 implies that an accurate estimate of DR is still possible by raising the order of AR fitting just three or so more than the theory dictates [AR(1)]. Moreover, this could be guided by AIC as shown in Fig. 6, where the decreasing trend of AIC ends at order three. In conclusion, when

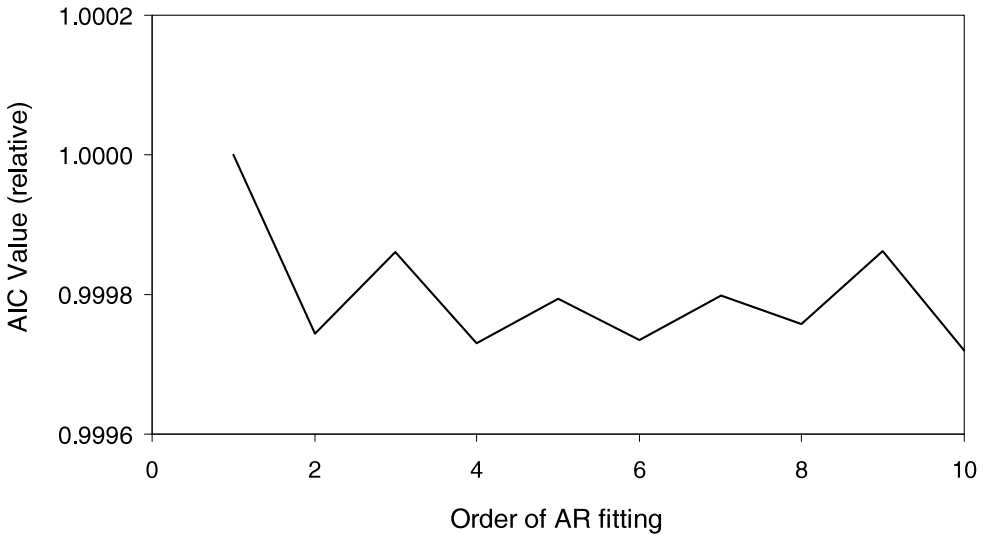

Fig. 4. AIC values of AR fitting with coarse-mesh projection (Fig. 3) for problem 1.

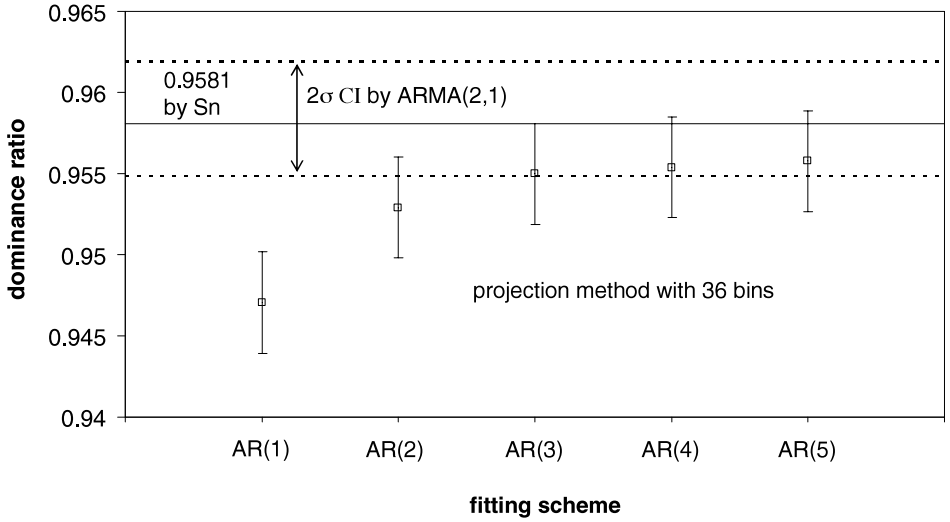

Fig. 5. Dominance ratio of problem 1 computed by projection method with 36 bins (confidence interval of 2σ).

coarse-mesh binning is used, AR(1) fitting performs very reliably and when fine-mesh binning is applied, such as one bin to each fuel bundle unit, one could still use AR fitting with the aid of AIC. However, the coarse-mesh projection approach is definitely preferable because of the unambiguous processes through computing; choose just AR(1), i.e., autocorrelation for DR.

Figure 7 shows a two-dimensional inhomogeneous problem (problem 2) with a DR of 0.9993 ± 0.0004 (2σ) taken from a previous work.[4] Figure 8 shows the DRs computed by the projection method with four bins along with the DRs computed by half-domain fitting. It is observed that the former has slightly smaller error. Also, if the confidence intervals are halved, the one σ confidence interval of AR(1) with the half-domain fitting does not share common values with the one σ confidence interval of ARMA(2,1).

Again, it is important to study what happens if one breaks the rule, i.e., the coarse-mesh projection. Figure 9 shows the DRs computed by the projection method with 324 bins (one bin assigned to each unit) as opposed to the coarse-mesh projection with four bins. Poor performance is observed for AR(1) and AR(2) fitting, but the performance of AR(5) through AR(10) is good. Figure 10 shows AIC values of the AR fitting in Fig. 9. It is observed that the decreasing trend of AIC ends at order six. Thus, as for problem 1, one could claim that AIC guided the DR computation with fine-mesh binning.

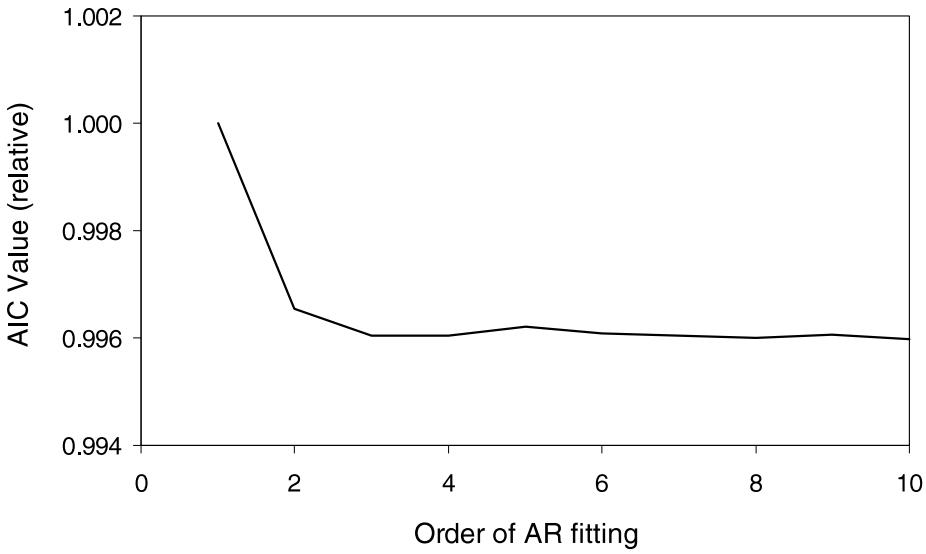

Fig. 6. AIC values of AR fitting via projection method with 36 bins (Fig. 5) for problem 1.

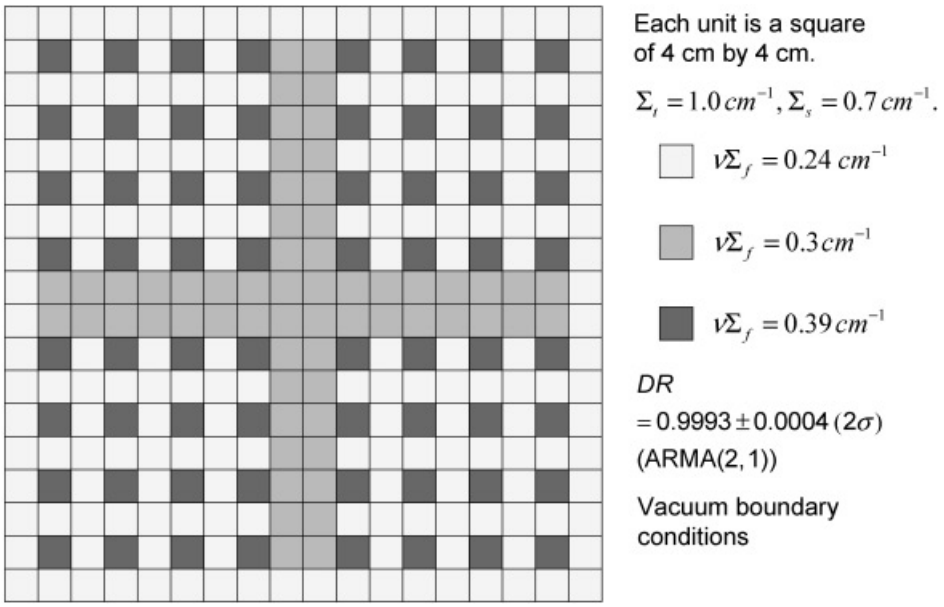

Fig. 7. Description of problem 2.

Figure 11 shows an example of the DRs computed by completely ignoring the projection method in Sec. II.C; DRs were determined by AR fitting of source at cell (8,8) in Fig. 7. Formally, this corresponds to choosing the following projection vector:

$$(0,\ldots,0,\underbrace{1}_{\substack{\text{component}\\ \text{corresponding}\\ \text{to cell } (8,8)}},0,\ldots,0)\ , \tag{54}$$

which has no relation with the eigenvectors of the adjoint of noise propagation. However, the complete cancellation of the first-mode eigenfunction $[S_1(\vec{r})]$ does not occur at cell (8,8); cell (8,8) is neither on the x nor the y Cartesian coordinate axis and is not on the upper-left to lower-right diagonal. Thus, one might hope that AR fitting yielded acceptable values of DR. However, as shown in Fig. 11, the DR computation by AR fitting is hopelessly off the reference value. Figure 12 shows the corresponding AIC values. One would observe that it was

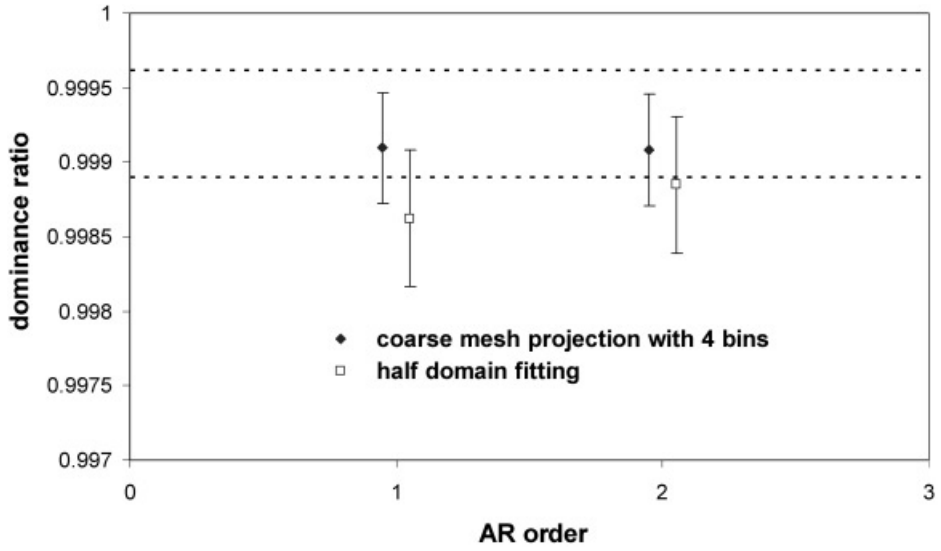

Fig. 8. Dominance ratio of problem 2 computed by coarse-mesh projection with four bins (confidence interval of 2σ).

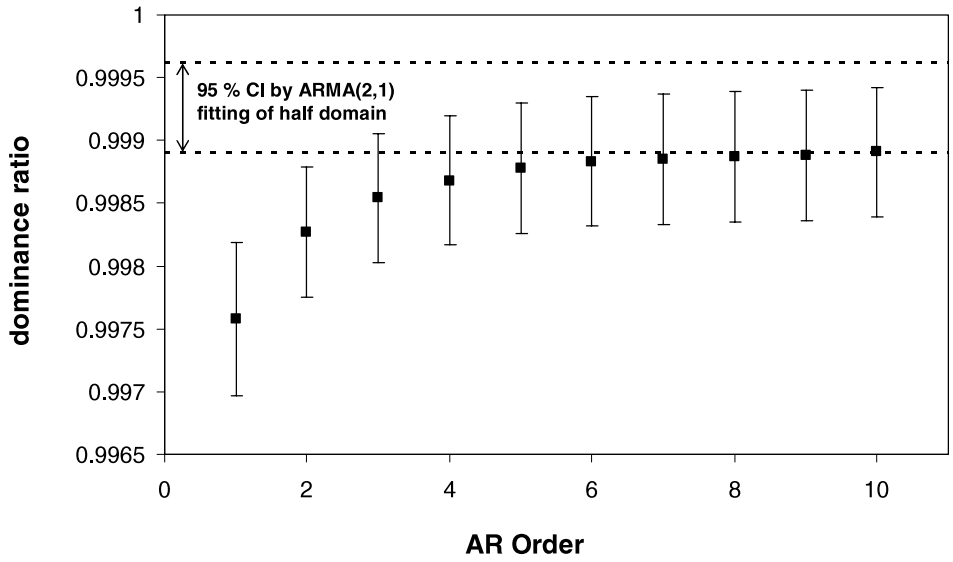

Fig. 9. Dominance ratio of problem 2 computed by projection method with 324 bins (confidence interval of 2σ).

impossible to make a judgment agreeable by all; is the decreasing trend toward order eighty or so real or spurious? Since the projection vector in Eq. (54) is not any of the eigenvectors of the adjoint of noise propagation, the fluctuation of the source at cell (8, 8) contains all eigenmodes with no preference to a particular mode. Therefore, AR(1) lumps them into one mode, AR(2) into two modes, AR(3) into three modes, etc., which means that the higher the order, the better the computed DR. This could provide plausible explanations for Figs. 11 and 12.

One can summarize the results for Problems 1 and 2 as follows:

1. If the projection vector is not of the eigenvectors of the adjoint matrix of noise propagation, the computation of DR by AR fitting is unreliable and can be grossly erroneous.

2. There are two possibilities when one chooses the projection vector to be the eigenvector corresponding to the largest eigenvalue of the adjoint matrix of noise propagation:

   a. If the binning is fine, one could rely on AIC.

   b. If one follows the coarse-mesh projection in Sec. II.D, just choose autocorrelation, the first-order parameter in AR(1); no ambiguity exists.

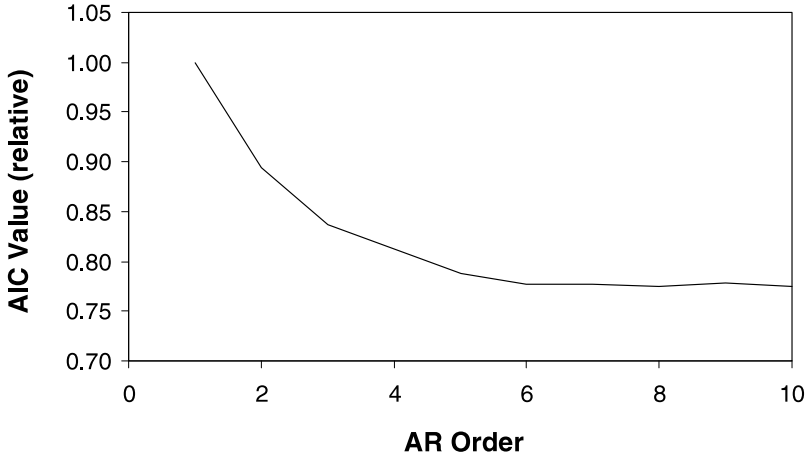

Fig. 10. AIC values of AR fitting via projection method with 324 bins (Fig. 9) for problem 2.

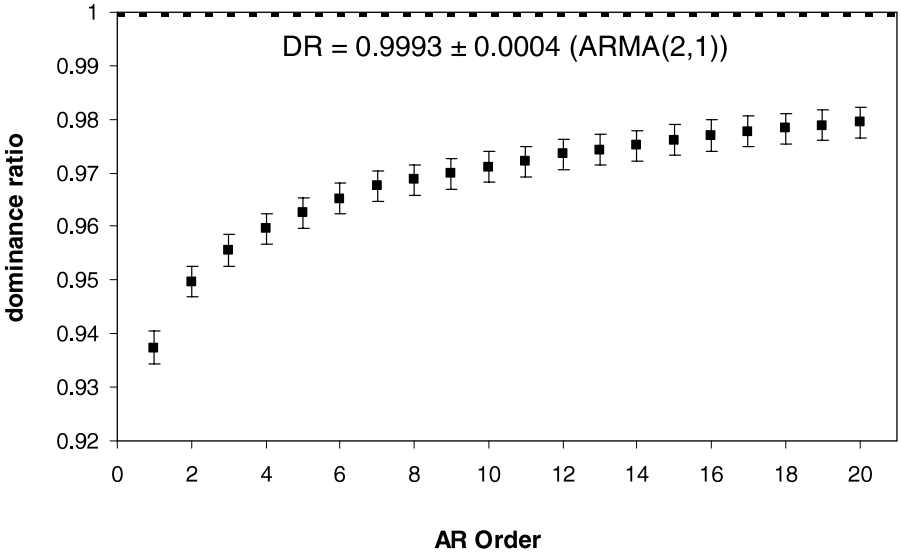

Fig. 11. Dominance ratio of problem 2 computed by AR fitting of source at cell (8,8) (confidence interval of 2σ).

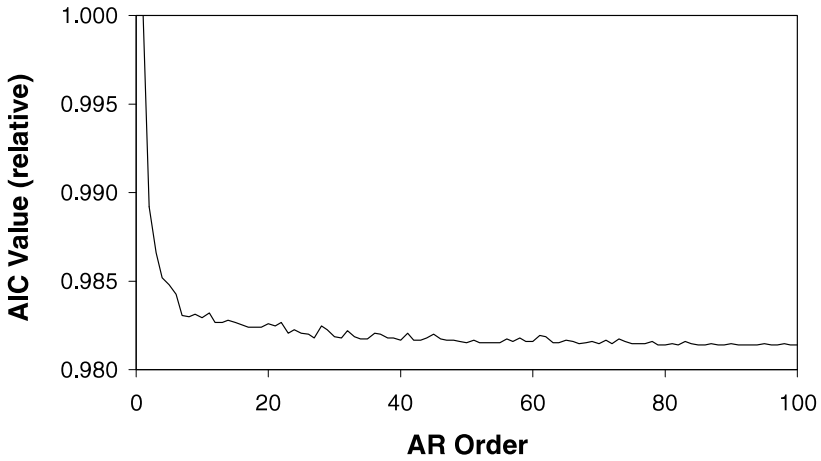

Fig. 12. AIC values of AR fitting of source at cell (8,8) (Fig. 11) for problem 2.

Homogeneous cube of size 200 cm by 200 cm by 200 cm

Vacuum boundary conditions

$$\Sigma_t = 1.0\ cm^{-1}$$
$$\Sigma_s = 0.75\ cm^{-1}$$
$$\Sigma_a = 0.25\ cm^{-1}$$
$$\nu\Sigma_f = 0.275\ cm^{-1}$$

Fig. 13. Description of problem 3.

Since it is very difficult to automate the judgment of whether the continuation of the decreasing trend of AIC is real or spurious, we consider the coarse-mesh projection superior to the projection method with fine-mesh binning.

Figure 13 shows a three-dimensional homogeneous cube problem (problem 3) from the same previous work[5] from which problem 1 was taken. Figure 14 shows 20 independent replicas of the DR values computed by the coarse-mesh projection with eight bins and the half-domain fitting. It is observed that the coarse-mesh projection with eight bins performs well with smaller errors,

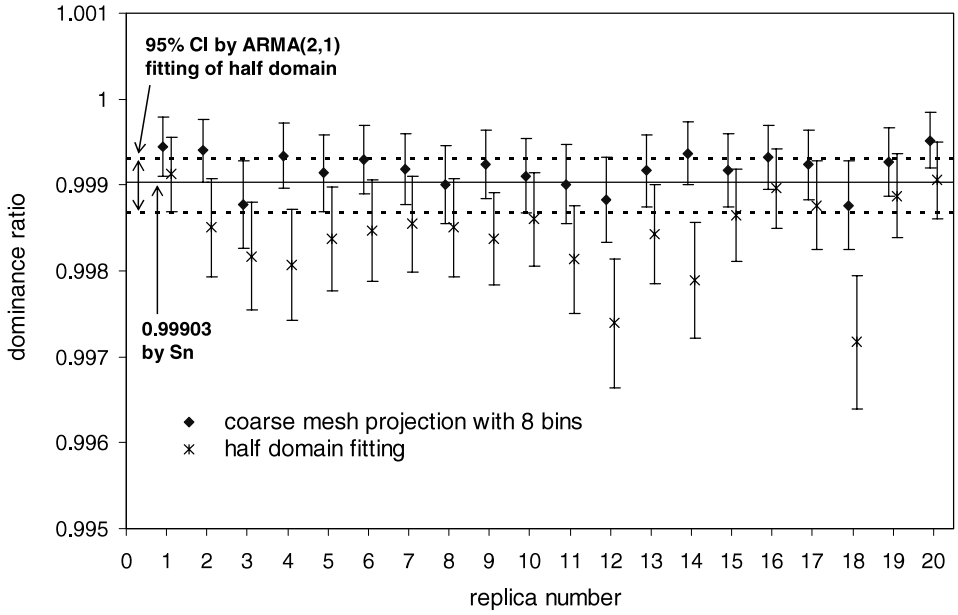

Fig. 14. Dominance ratio of problem 3 (three-dimensional cube) computed by AR(1) fitting (confidence interval of 2σ).

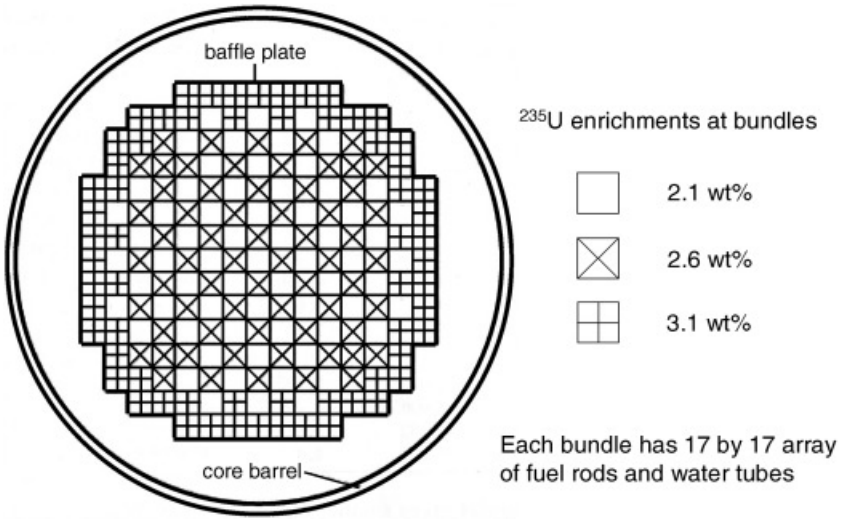

Fig. 15. Description of problem 4 (PWR initial core).

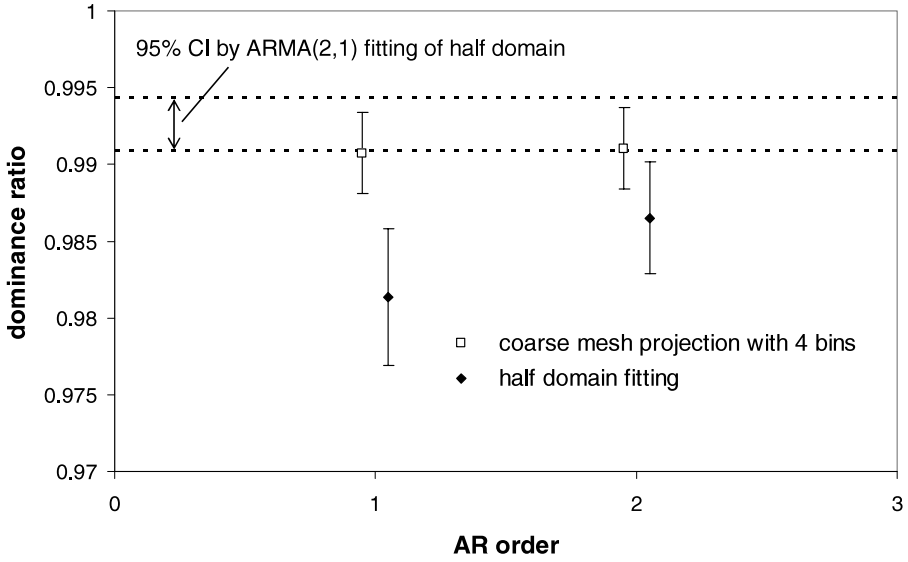

Fig. 16. Dominance ratio of problem 4 computed by coarse-mesh projection with four bins (confidence interval of 2σ).

while the half-domain fitting appears to be biased. Figure 15 shows an initial core problem (problem 4) of a pressurized water reactor[14] (PWR). The DR values of its two-dimensional version with the reflecting top and bottom boundaries are shown in Fig. 16, where the MC computation was performed in the continuous-energy mode. One can see greatly superior performance of the coarse-mesh projection with four bins.

IV. CONCLUSION

This work has derived that the scalar time series obtained via the projection on the eigenvectors of the adjoint matrix of noise propagation is an AR(1) process with the autocorrelation coefficient equal to the eigenvalue ratio of fission source distribution with respect to the fundamental mode eigenvalue. This theoretically derived result has been successfully implemented to numerically compute the DR of fission source distribution.

ACKNOWLEDGMENTS

Part of this work was supported by the Nuclear Engineering Educational Research Program of the U.S. Department of Energy under contract DE-FG07-05ID14705. The second author also expresses his sincere thanks to Group X-3 at Los Alamos National Laboratory for financial and technical support. In addition, both authors greatly appreciate constructive comments on the original manuscript by O. Jacquet and Y. Richet at Institut de Radioprotection et de Sûreté Nucléaire in France.

REFERENCES

1. R. MIRO et al., "A Nodal Modal Method for the Neutron Diffusion Equation. Application to BWR Instabilities Analysis," *Ann. Nucl. Energy*, **29**, 1171 (2002).

2. K. HASHIMOTO, "Linear Modal Analysis of Out-of-Phase Instability in Boiling Water Reactor Cores," *Ann. Nucl. Energy*, **20**, *12*, 789 (1993).

3. B. R. NEASE and T. UEKI, "Extension of MacMillan's Approach to Autocorrelation Estimation of Monte Carlo Fission Sources," *Trans. Am. Nucl. Soc.*, **93**, 563 (2005).

4. T. UEKI and B. R. NEASE, "Time Series Analysis of Monte Carlo Fission Sources—II: Confidence Interval Estimation," *Nucl. Sci. Eng.*, **153**, 184 (2006).

5. T. UEKI, F. B. BROWN, D. K. PARSONS, and J. S. WARSA, "Time Series Analysis of Monte Carlo Fission Sources—I: Dominance Ratio Computation," *Nucl. Sci. Eng.*, **148**, 374 (2004).

6. G. E. P. BOX, G. M. JENKINS, and G. C. REINSEL, *Time Series Analysis: Forecasting and Control*, Prentice-Hall, Inc., Upper Saddle River, New Jersey (1994).

7. IMSL Stat/Library Vol. 2, Visual Numerics, Inc., Houston Texas (1997).

8. X-5 MONTE CARLO TEAM, "MCNP—A General Purpose Monte Carlo N-Particle Transport Code, Version 5," LA-UR-03-1987, Los Alamos National Laboratory (Apr. 2003).

9. E. E. LEWIS and W. F. MILLER, Jr., *Computational Methods of Neutron Transport*, American Nuclear Society, La Grange Park, Illinois (1993).

10. R. J. BRISSENDEN and A. R. GARLICK, "Biases in the Estimation of Keff and Its Error by Monte Carlo Methods," *Ann. Nucl. Energy*, **13**, 63 (1986).

11. H. AKAIKE, "Markovian Representation of Stochastic Processes and Its Application to the Analysis of Autoregressive Moving Average Processes," *Ann. Inst. Stat. Math.*, **26**, 363 (1974).

12. T. UEKI, F. B. BROWN, D. K. PARSONS, and D. E. KORNREICH, "Autocorrelation and Dominance Ratio in Monte Carlo Criticality Calculations," *Nucl. Sci. Eng.*, **145**, 279 (2003).

13. D. K. PARSONS and D. E. KORNREICH, "Approximations to the Dominance Ratio Using Effective and Infinite Multiplication Results," *Proc. Topl. Mtg. Nuclear Mathematical and Computational Sciences (M&C 2003): A Century in Review—A Century Anew*, Gatlinburg, Tennessee, April 6–10, 2003, American Nuclear Society (2003) (CD-ROM).

14. M. NAKAGAWA and T. MORI, "Whole Core Calculations of Power Reactors by Use of Monte Carlo Method," *J. Nucl. Sci. Technol.*, **30**, *7*, 692 (1993).

Attachment 3

HIGHER EIGENMODE ANALYSIS WITH COARSE MESH PROJECTION IN MONTE CARLO FISSION SOURCE ITERATIONS

Brian R. Nease and Taro Ueki

University of New Mexico, Department of Chemical and Nuclear Engineering
nease81@unm.edu; tueki@unm.edu

INTRODUCTION

The eigenvalues k_i of the fission source distribution, which are ordered $|k_0| > |k_1| > |k_2| > \cdots$, have several applications in reactor analysis including stability analysis in boiling water reactors [1] and confidence interval estimation of the fission source distribution in iterated source Monte Carlo (MC) calculations [2]. Recent work has shown that the largest non-fundamental eigenvalue ratio k_1/k_0 known as the dominance ratio (DR) can be accurately computed by applying time series methods to the MC fission source distribution [3]. The methodology therein, called Coarse Mesh Projection Method (CMPM), involves estimating the eigenvector of a noise propagation matrix corresponding to the ratio k_1/k_0, applying it to the fission source distribution to create a new time series, and performing an autoregressive fitting of order 1 [AR(1)]. This is a robust technique: it requires only a very simple fission source binning scheme and the AR(1) fitting is guaranteed convergent [4]. In the present work, we investigate the application of CMPM to the calculation of higher-order eigenvalue ratios k_j/k_0, $j \geq 2$.

The present work is not fully consistent with some of the numerical results in previous work [3]. We found an inappropriate programming which affected the computation of k_1/k_0 with the non-standard binning scheme therein. Correction was made on the program and it has turned out that CMPM equally works well to compute k_j/k_0, $j \geq 2$ as the theory predicts. We will separately communicate the corrigendum to *Nuclear Science and Engineering*. Herewith, we specifically report that the usefulness of CMPM is not limited to the computation of k_1/k_0.

COARSE MESH PROJECTION METHOD

CMPM for computing k_i/k_0 consists of two main parts. The first consists of a multivariate regression analysis used to compute the noise propagation matrix. The second consists of coarse mesh projection for generating a new scalar time series.

It has been shown [5] that the fluctuating part of the fission source distribution after the *m*-th stationary cycle in an MC iterated source calculation, denoted $\vec{e}^{(m)}$, can be represented as

$$\vec{e}^{(m)} = \mathbf{A}_0 \vec{e}^{(m-1)} + \vec{\varepsilon}^{(m)}, \tag{1}$$

where $\mathbf{A}_0$ is the $p \times p$ noise propagation matrix and $\vec{\varepsilon}^{(m)}$ is a $p \times 1$ noise component matrix, both corresponding to a mesh with p bins. Important properties of them are

$$E[\vec{\varepsilon}^{(m1)}(\vec{e}^{(m2)})^T] = 0, m1 > m2 \tag{2}$$

$$E\left[\vec{\varepsilon}^{(m)}\right] = 0 \tag{3}$$

$$E\left[\vec{\varepsilon}^{(m1)}(\vec{\varepsilon}^{(m2)})^T\right] = 0, m1 > m2 \tag{4}$$

where *T* stands for transpose. By multiplying (1) on the right by $\{\vec{e}^{(m-1)}\}^T$, taking the expectation, using Eq. (2) and replacing *m* by *m*+1, one can obtain the expression for the noise propagation matrix as

$$\mathbf{A}_0 = L_1 L_0^{-1} \tag{5}$$

where

$$L_0 = E\left[\vec{e}^{(m)}(\vec{e}^{(m)})^T\right] \tag{6}$$

$$L_1 = E\left[\vec{e}^{(m+1)}(\vec{e}^{(m)})^T\right] \tag{7}$$

With the matrix $\mathbf{A}_0$ determined, a projection vector can be applied to the fluctuating part of the source distribution to create a new scalar time series. This projection vector is chosen to be the eigenvector of $\mathbf{A}_0$ corresponding to the desired eigenvalue ratio. The details are as follows. The eigenvalue problem of $\mathbf{A}_0$ is [3]

$$\mathbf{A}_0 \vec{b}_i = \lambda_i \vec{b}_i, i = 1, \ldots, p, \tag{8}$$

$$\mathbf{A}_0^* \vec{d}_i = \lambda_i \vec{d}_i, i = 1, \ldots, p, \tag{9}$$

where $\lambda_i \approx k_i / k_0$, $\mathbf{A}_0^*$ is the adjoint matrix of $\mathbf{A}_0$, $\mathbf{A}_0^* = \mathbf{A}_0^T$ because $\mathbf{A}_0$ is real. By the standard results of linear algebra, $\mathbf{A}_0^*$ and $\mathbf{A}_0$ have the same set of eigenvalues with their eigenvectors satisfying

$$\vec{d}_j^T \vec{b}_i = 0 \quad \text{if} \quad \lambda_j \neq \lambda_i . \tag{10}$$

Defining a scalar time series as

$$y^{(m)} \equiv \vec{d}_j^T \vec{e}^{(m)}, \tag{11}$$

the application of the eigenvector $\vec{d}_j$ to (1) leads to [3]

$$y^{(m)} = \lambda_j y^{(m-1)} + z^{(m)}, \tag{12}$$

implying that $y^{(m)}$ follows the autoregressive process of order 1 [AR(1)] with the autocorrelation coefficient λ_j. Since the *j*-th eigenvalue of the continuous counterpart of $\mathbf{A}_0$ is exactly k_j / k_0 [5]., the accurate estimation of k_j / k_0 is possible via the analysis of fluctuation instead of directly solving $\mathbf{A}_0$ with a matrix solver. Thus λ_j estimated as the autocorrelation coefficient of the AR(1) process (12) yields an estimate of k_j / k_0.

NUMERICAL RESULTS

Results are presented for two problems. Problem 1 is a one-group isotropically-scattering inhomogeneous and diagonally symmetric reactor system shown in Figure 1. The macroscopic cross sections for the two hot and cold fuel types are $\Sigma_t = 1.0$, $\Sigma_s = 0.7$, $\nu\Sigma_f = 0.39\,(\mathrm{H})$, $0.24\,(\mathrm{C})$, all in units cm^{-1}. Each bin is a square with units 4 cm by 4 cm, with vacuum boundaries at the exterior. Table 1 compares the first four eigenvalue ratios computed by CMPM and by the fission matrix method (FMM) [6] with the discontinuous finite element discrete ordinates methods [7]. The FMM reference values were computed using a 2,304 (48×48) bin mesh. The 95% confidence interval CMPM results were computed using one source tally bin per fuel region, 36 bins in total. This prevents the complete cancellation of the desired mode eigenfunctions from occurring. In every case, the reference FMM value is contained within the CMPM 95% confidence interval. It should also be noted that the confidence interval of the CMPM values are quite small. Also, k_1 / k_0 is computed to be 0.9581 by the spectral radius analysis of outer iterations in the same discontinuous finite element discrete ordinates methods [7]. This value is contained in the confidence interval of k_1 / k_0

H	C	H	C	H	C
C	H	C	H	C	H
H	C	H	C	H	C
C	H	C	H	C	H
H	C	H	C	H	C
C	H	C	H	C	H

Figure 1: Checkerboard reactor system

Table 1: First four eigenvalue ratios of checkerboard reactor system

	CMPM *	FMM
# of bins	36	2,304
k1/k0	(0.95409, 0.95989)	0.95740
k2/k0	(0.95324, 0.95910)	0.95710
k3/k0	(0.91660, 0.92426)	0.92031
k4/k0	(0.89253, 0.90121)	0.89708

*** 95% Confidence Interval**

Problem 2 is a one-group multi-region 1-D slab system with vacuum boundaries and three materials. The macroscopic cross sections (units in cm^{-1}) are

Material 1 (width 1cm):
$\Sigma_t = 1.0$, $\Sigma_s = 0.8$, $\nu\Sigma_f = 0.30$, $\nu = 3.0$
Material 2 (width 1cm):
$\Sigma_t = 1.0$, $\Sigma_s = 0.8$
Material 3 (width 5cm):
$\Sigma_t = 1.0$, $\Sigma_s = 0.1$

These materials are placed from left to right as 1, 2, 3, 2 and 1. This is a very difficult problem to analyze because k_1 / k_0 is computed to be 0.99957 by the Greens Function Methods (GFM) [8]. Such a large DR indicates that the MC

cycles are still correlated with each other, even when separated by a distance of 5,000 active cycles. Note $0.99957^{5000} = 0.11643$. Table 2 compares the first four eigenvalue ratios computed by GFM and CMPM. The GFM reference values were computed using a 1,800 bin mesh. The 95% confidence interval CMPM results were computed using 24 source bins (12 bins over each material Region 1). In three of four cases the reference GFM values were contained in the CMPM 95% confidence interval. Even in the case of k_3/k_0, the reference value is contained in a 3-σ confidence interval.

Table 2: First four eigenvalue ratios of 1-D slab system

	CMPM *	GFM
# of bins	24	1,800
k1/k0	(0.99906, 0.99974)	0.99957
k2/k0	(0.29234, 0.31192)	0.30465
k3/k0	(0.28518, 0.30392)	0.30464
k4/k0	(0.16045, 0.17977)	0.16774

*** 95% Confidence Interval**

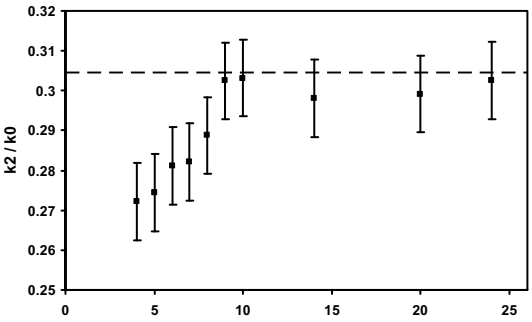

Figure 3: Second eigenvalue ratios of 1-D slab reactor system

The last result is shown in Figure 3 where effect of the number of bins is examined when calculating k_2/k_0 for Problem 2. Due to the rapidly changing shape of the second eigenmode after the fundamental mode, Figure 3 suggests that a minimum of a 10-bin mesh (five bins per fuel region) is necessary to capture the mode and accurately compute k_2/k_0. At this moment, no clear method has yet been developed to determine the minimum number of bins in an on-the-fly manner. However, we also analyzed loosely coupled systems with three fissile components and the k_1/k_0 and k_2/k_0 values both larger than 0.99, and obtained agreements with GFM estimates, using fewer than 30 bins.

CONCLUSION AND FUTURE WORK

We have shown that the Coarse Mesh Projection Method is able to accurately compute higher-order eigenvalue ratios using only an autoregressive fitting of order 1. It should be investigated whether raising the AR fitting order will improve CMPM cases with too few bins. Another interesting option would be to apply information criteria to determine if the bin count is sufficient.

REFERENCES

1. R. Miro et al., "A Nodal Modal Method for the Neutron Diffusion Equation. Application to BWR Instabilities Analysis," *Annals of Nuclear Energy*, **29**, 1171, 2002.
2. T. Ueki and B.R. Nease, "Time Series Analysis of Monte Carlo Fission Sources – II: Confidence Interval Estimation," *Nuclear Science and Engineering*, **153**, 184 (2006).
3. B.R. Nease, T. Ueki, "Time Series Analysis of Monte Carlo Fission Sources: III. Coarse Mesh Projection," *Nuclear Science and Engineering*, **157**, 51 (2007).
4. G.E.P. Box, G.M. Jenkins and G.C. Reinsel, Time series analysis: forecasting and control, Prentice-Hall, Inc., Upper Saddle River, New Jersey (1994).
5. T. Ueki, F.B. Brown, D.K. Parsons, and J.S. Warsa, "Time Series Analysis of Monte Carlo Fission Sources: I. Dominance Ratio Computation," *Nuclear Science and Engineering*, **148**, 374(2004).
6. K.W. Morton, "Criticality Calculations by Monte Carlo Methods," AERE-TR-1903, Harwell (1956).
7. T.A. Wareing, J.M. McGhee, J.E. Morel, and S.D. Pautz, "Discontinuous Finite Element S_N Methods on Three-Dimensional Unstructured Grids," *Nuclear Science and Engineering*, **138**, 256 (2001).
8. D.E. Kornreich, B.D. Ganapol, "The Green's Function Method for Nuclear Engineering Applications," *Nuclear Science and Engineering*, **31**, 293 (2003).